

**Nanofracture mechanics:
Scanning Force Microscopy for the
investigation of adhesion and corrosion at
solid-solid interfaces**

INAUGURALDISSERTATION

zur

Erlangung der Würde eines Doktors der Philosophie

vorgelegt der

Philosophisch-Naturwissenschaftlichen Fakultät

der Universität Basel

von

André Nicolas Kaufmann

aus Escholzmatt (LU)

Villigen, 2013

Originaldokument gespeichert auf dem Dokumentenserver der Universität Basel

edoc.unibas.ch



Dieses Werk ist unter dem Vertrag „Creative Commons Namensnennung-Keine kommerzielle Nutzung-Keine Bearbeitung 2.5 Schweiz“ lizenziert. Die vollständige Lizenz kann unter creativecommons.org/licences/by-nc-nd/2.5/ch eingesehen werden.



Namensnennung-Keine kommerzielle Nutzung-Keine Bearbeitung 2.5 Schweiz

Sie dürfen:



das Werk vervielfältigen, verbreiten und öffentlich zugänglich machen

Zu den folgenden Bedingungen:



Namensnennung. Sie müssen den Namen des Autors/Rechteinhabers in der von ihm festgelegten Weise nennen (wodurch aber nicht der Eindruck entstehen darf, Sie oder die Nutzung des Werkes durch Sie würden entlohnt).



Keine kommerzielle Nutzung. Dieses Werk darf nicht für kommerzielle Zwecke verwendet werden.



Keine Bearbeitung. Dieses Werk darf nicht bearbeitet oder in anderer Weise verändert werden.

- Im Falle einer Verbreitung müssen Sie anderen die Lizenzbedingungen, unter welche dieses Werk fällt, mitteilen. Am Einfachsten ist es, einen Link auf diese Seite einzubinden.
- Jede der vorgenannten Bedingungen kann aufgehoben werden, sofern Sie die Einwilligung des Rechteinhabers dazu erhalten.
- Diese Lizenz lässt die Urheberpersönlichkeitsrechte unberührt.

Die gesetzlichen Schranken des Urheberrechts bleiben hiervon unberührt.

Die Commons Deed ist eine Zusammenfassung des Lizenzvertrags in allgemeinverständlicher Sprache: <http://creativecommons.org/licenses/by-nc-nd/2.5/ch/legalcode.de>

Haftungsausschluss:

Die Commons Deed ist kein Lizenzvertrag. Sie ist lediglich ein Referenztext, der den zugrundeliegenden Lizenzvertrag übersichtlich und in allgemeinverständlicher Sprache wiedergibt. Die Deed selbst entfaltet keine juristische Wirkung und erscheint im eigentlichen Lizenzvertrag nicht. Creative Commons ist keine Rechtsanwalts-gesellschaft und leistet keine Rechtsberatung. Die Weitergabe und Verlinkung des Commons Deeds führt zu keinem Mandatsverhältnis.

Genehmigt von der Philosophisch-Naturwissenschaftlichen Fakultät auf Antrag von:

Prof. Dr. T.A. Jung

Prof. Dr. E. Meyer

Basel, den 26. April 2011

Prof. Dr. M. Spiess, Dekan

CONTENTS

Abstract	IV
Abbreviations	VI
1. Introduction	1
1.1. Material testing.....	1
1.2. Scientific interest.....	2
1.3. Technological interest	3
1.4. References	5
2. Fracture mechanics – an overview	6
2.1. Synopsis	6
2.2. Brittle and ductile fracture	6
2.2.1. Brittle fracture	6
2.2.2. Ductile fracture.....	8
2.3. Theoretical mechanical strength of solid bodies.....	9
2.4. Fracture mechanics of the ideal brittle body (Griffith theory).....	11
2.5. The three fundamental crack opening modes.....	13
2.6. Fracture mechanics on the nanoscale and other size effects	14
2.7. References	17
3. Introduction to Scanning Force Microscopy	18
3.1. Synopsis	18
3.2. Common SFM concepts.....	18
3.3. The scanning probe	20
3.4. Piezoceramic actuators.....	21
3.5. Relevant forces.....	22
3.5.1. Van der Waals forces	22

3.5.2. Electrostatic forces	23
3.5.3. Capillary forces	23
3.5.4. Forces in liquids	24
3.6. Force sensing.....	25
3.7. Force calibration.....	25
3.7.1. Normal force calibration	26
3.7.2. Lateral force calibration	28
3.8. References	30
4. Fracture experiments in air	31
4.1. Introduction	31
4.2. Nanopillar production	31
4.3. Fracture mechanics using SFM.....	34
4.3.1. Conditions	34
4.3.2. Interactions between tip and pillar	36
4.4. Statistical fracture experiments	38
4.5. Nanopillar - Lithography.....	41
4.6. Summary/Discussion	44
4.7. References	45
5. Fracture mechanics in a corrosive environment.....	47
5.1. Introduction	47
5.2. Theory	47
5.2.1. Influence of water.....	47
5.2.2. Interactions between electrolytes in general and in particular of sodium ions with charged surfaces	49
5.3. Nanopillar experiments in liquids	50
5.4. Interpretation of the measured data.....	57

5.5. References	60
6. The titanium polyimide interface	61
6.1. Introduction	61
6.2. TEM, FIB and XPS	62
6.2.1. Transmission electron microscopy	62
6.2.2. Focused Ion Beam (FIB)	62
6.2.3. X-ray induced photoelectron spectroscopy (XPS)	63
6.3. Material and methods	63
6.3.1. Overview	63
6.3.2. Used materials	64
6.3.3. Preparation of the samples	65
6.3.4. Nanopillar production using FIB.....	67
6.4. Results	68
6.4.1. XPS.....	68
6.4.2. Fracture experiments with the SFM.....	70
6.4.3. Determination of the friction and the lateral force	72
6.4.4. TEM	75
6.5. Summary and discussion.....	76
6.6. References	78
7. Summary and conclusions	79
Acknowledgement	83
List of publications	85
Curriculum Vitae	88

ABSTRACT

Fracture processes are crucially determined by structural features on the molecular/nanometer scale (cavities, occlusions, cracks, etc.) as well as on the atomic scale (e.g. interstitial, substitutional and vacancy defects). In this work, fracture mechanics experiments were performed with fabricated nanostructures, so-called nanopillars. Furthermore, material interfaces had been introduced into these nanopillars as weak links in order to act as well-defined breaking points. By exerting calibrated forces onto these nanostructures, the threshold force for fracture incidents can be determined and hence the adhesion strengths of the interfaces involved can be studied.

All such experiments were performed using a Scanning Force Microscope (SFM). Here, force and topography investigations, using a cantilever tip as a tool, reveal information about the fracture behavior of a particular interface as well as information regarding the mechanical strength. The SFM was used in the tapping (intermitted) or in the contact mode to fracture single nanopillars or an ensemble of them. For statistical examinations, an area of nanopillars was scanned with increased normal forces. Therefore, interfaces manufactured for microelectronic applications or micro-electro-mechanical systems (MEMS) can be studied by low forces applied to nanopillars exhibiting realistic interface dimensions.

Due to the small dimensions of the manufactured nanopillars, slow processes, such as the weakening of the interface by fatigue (also including heat cycling in devices) or by physico-chemical processes (e.g. by tribochemical processes or corrosion which may occur in a liquid environment) can be monitored on considerably shorter time scales and under easier to control conditions than with macroscopic specimens. Additionally, such fracture experiments performed with nanopillars designed to mimic macroscopic fracture experiments, in medium (characteristic cross section $\sim\text{cm}^2$) to large scale ($> \sim\text{m}^2$) engineering, are often less cost intensive compared to large, real-world samples in time consuming (\sim many load/unload heat/cool cycles, extended exposure to ambient or corrosive fluids etc.) conventional fracture experiments.

Another important application comprises the study of a soft metal/polyimide interface, which is important for flexible microelectronic devices and flexible interconnect circuitry. Here, interface problems, specifically failure incidents after exposure to temperature cycling and/or mechanical load/unload cycles, have been associated with the occurrence of interfacial

contamination, e.g. with residual water originating from the polyimide curing process. Hence, in a well-chosen model experiment under ultra-high vacuum (UHV) conditions, a precise amount of water was deposited on an in-situ produced polyimide sample which then was coated by a metal. Afterwards, the nanopillar structures were generated by Focused Ion Beam (FIB) milling.

This work established a radically new approach to perform fracture mechanics experiments down to the few nanometers, which provides a route towards a better understanding of fracture processes down to an atomic/molecular scale.

ABBREVIATIONS

AFM	Atomic force microscope
BPDA	Biphenyl dianhydride
CCD	Charge-coupled device
DLC	Diamond like carbon
DVD	Digital versatile disc
EBL	Electron beam lithography
EDL	Electrical double layer
FIB	Focused ion beam
HV	High vacuum
IHL	Inner Helmholtz layer
IPA	Isopropyl alcohol
LJ	Lennard-Jones
LMN	Laboratory for micro- and nanotechnology
LPCVD	Low pressure chemical vapor deposition
MEMS	Microelectro-mechanical systems
MIBK	Methyl isobutyl ketone
ML	Monolayer
NEMS	Nanoelectro-mechanical systems
NMP	N-Methyl-2-pyrrolidone
OHL	Outer Helmholtz layer
PCB	Printed circuit board
PES	Photoelectron spectroscopy
PI	Polyimide

PMMA	Polymethyl methacrylat
PPD	para-Phenylene diamine
PSD	Photo-sensitive detector
PSI	Paul Scherrer institute
PZT	Lead zirconate titanate
RIE	Reactive ion etching
RMS	Root mean square
SEM	Scanning electron microscope
SFM	Scanning force microscope
SMD	Surface mounted device
SOI	Silicon on insulator
SPM	Scanning probe microscopy
STM	Scanning tunneling microscope
TEM	Transmission electron microscopy
TMR	Trace minus retrace
UHV	Ultrahigh vacuum
WORM	Write once read many [times]
XPS	X-ray photoelectron spectroscopy

1. INTRODUCTION

In manufacturing in general, the use of tools/equipment depends on the properties of the material used in the construction of a particular work piece. On the other hand, it is the chemical composition and the physical structure, more general the physico-chemical properties of the material of concern, which must be chosen towards the intended application or product. Altogether, the tools, the processing and the material for the specific applications have to be optimized in advance, to obtain strength and lifetime optimized products. Insufficient material strength e.g. due to low adhesion between grain boundaries but also due to alterations of a structures integrity or shape caused by fatigue, bending, wear and/or corrosion, are usually the reason for premature failure. For an analytical understanding of materials and their failure, it is important to link manufacturing and material parameters to test results which provide the particular challenge in that the tests should be performed fast, while some of the detrimental properties depend on processes which are inherently slow. This has been the specific goal of this thesis: On the basis of a ‘proof of principle’, established in earlier scientific publications [1.1, 1.2], an experimental technique and routine procedure has been developed for the fast and local determination of interface strengths in technologically relevant setups. This technique now reaches a state far beyond the well-established material test procedures for macroscopic specimens and opens the way towards a reference process, in some analogy to the methods named after Brinell or Vickers for surface hardness determinations.

1.1. *Material testing*

In contrast to bulk materials, surfaces and interfaces have properties which need specifically adapted methods for their examination. To obtain new or modified surface and interface properties for testing, methods such as surface coating by deposition or immersion are used. Furthermore, surfaces and interfaces provide a template for an enhanced interaction with external media by offering a pathway for diffusion which may facilitate aging processes, just to provide an example. This behavior at surfaces and interfaces underlines the importance of methods and tools for their in-depth characterization.

It is important to note that the adhesion at solid-solid interfaces crucially depends on local properties e.g. on whether the interface has been grown uniformly, with specific

physical or chemical interactions and/or with or without epitaxial conformity. All such issues have in common, that the microscopic adhesion properties must be quantified as a function of the manufacturing parameters in order to be able to improve the mechanical properties of systems and devices as a whole.

1.2. *Scientific interest*

Interfaces play an important role in chemistry, physics and biology. Many processes (e.g. heterogeneous catalysis) take place at interfaces or influence the material behavior in some way. Grain boundaries for example can affect the mechanical behavior stronger than the chemical nature of the material itself. In mechanics, defects at interfaces can decrease adhesion and strength and cause the failure of entire systems. Methods for measuring the mechanical properties are numerous, since the importance of mechanical quantities was recognized very early during the time of industrialization. Such a test procedure is the Charpy impact test [1.3] which determines the fracture strength (toughness) in case of an exposure to an abrupt force (Fig.1.1).

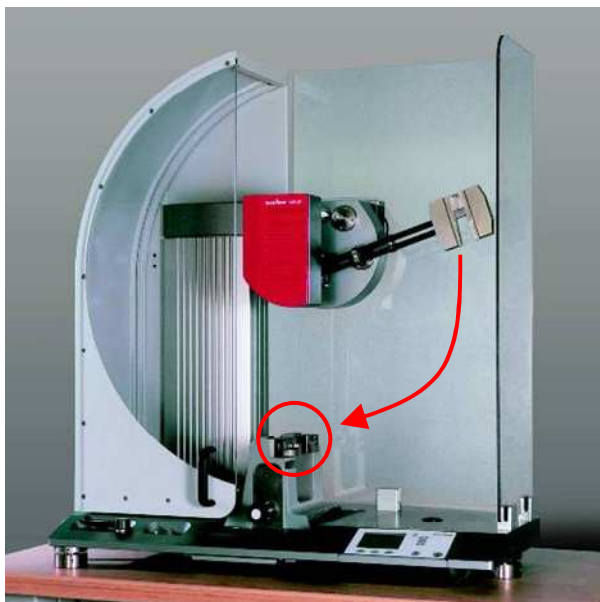


Fig.1.1: A Charpy test machine for measuring the material toughness upon a sudden mechanical impact. The red arrow indicates the fall hammer direction while the red circle shows the location of the specimen. Fall height and weight of the fall hammer defines the applied force (Image taken from a Zwick GmbH advertising brochure).

Macroscopic tests typically reflect the integral influence of a very large number of defects. A technique, which is able to determine single defects therefore, must be carried out on the same length scale of defects which is very small i.e. some micrometers at most (in the case of grain boundary defects). This provides the motivation to use a Scanning Force Microscopy (SFM) based [1.4] probing method for this project. SFM gives access to the sample topography and can be used to exert defined forces to manipulate objects like atoms or

molecules [1.5-1.7] in a controlled manner. Here, defined nanostructures were used to investigate the fracture behavior of SiO₂/Si [1.2]. The examined structures feature a cylindrical shape and consist of a material interface at a certain height above the base level which is why they are referred to as nanopillars or nanotowers. The exact positioning of the interface within the nanopillar is a prerequisite to recognize if fracturing happened at the interface or in either one of the materials involved.

1.3. Technological interest

Furthermore, the polyimide-on-metal material system, a typical interface used in flexible electronics, was characterized in collaboration with an industry partner, Hightec MC Ltd. in Lenzburg, Switzerland. In their business, polyimides are used for flexible 'printed circuit boards' to support wirings and small micro-electronic device packages, most often in surface mounted device (SMD) technology. Interface adhesion here determines the range of heating/cooling or bending cycles the final assembly can take before delamination occurs. Thereby, the strength of this particular interface is of key importance for a large group of products like medical invasive surgery and diagnostics where cameras and other sensors have to be operated through long flexible tubes and in aerospace where the use of the solvent free polyimide material instead of more conventional materials warrants that there is minimal outgassing of solubilizing/softening agents which protects the optical mirrors from condensation. In SiO₂ on Si interfaces, which are important for the 'SOI'- Silicon-on-Insulator technology used in the fabrication of high performance logic processors (since year 2000 by IBM and others) for example, delamination results in the failure of the whole device. It is worth to note, that the systematic investigation of interface strength and interface fracture by SFM in industry is new and uniquely allows investigating interfaces of only some hundred nm².

These examples demonstrate that beyond fundamental investigations with model systems, also material systems used for specific applications can be characterized. Therefore, this project paved the way towards routine methods investigating fracture mechanisms in general, both in academic and in an industrial context. On these grounds, the following topics have systematically been examined by our newly developed Scanning Force Microscopy (SFM) based fracture investigation technique:

- Adhesion of a SiO₂ thin film on top of a Si(100) substrate
- Directed fracture experiments on single nanopillars (arbitrary pattern generation)
- Corrosion experiments at SiO₂/Si nanopillars in brine solutions
- Adhesion between a titanium metallization layer and a polyimide substrate

The content of this work is structured as follows: After the introduction, the second chapter discusses theoretical aspects of fracture mechanics. In Chapter 3, SFM techniques and their potential to probe and manipulate surfaces are discussed. Chapter 4 presents material interface tests which are used to characterize SiO₂/Si interfaces but also introduces concepts for the application of nanopillars for data storage purposes. Chapter 5 shows experiments with the same pillars as in the foregoing chapter but in a liquid media: Thereby, corrosion phenomena can be studied much faster than with larger, real-world structures. In chapter 6, the influence of water, affecting interface strength in a technological application, is examined. In this industrial problem, the adhesion between a polymer and a metallization layer is studied. Finally, chapter 7 provides a summary and draws conclusions.

1.4. References

- [1.1] Baumeister, B., T.A. Jung, and E. Meyer, *Nanoscale fracture studies using the scanning force microscope*. Applied Physics Letters, 2001. **78**(17): p. 2485-2487.
- [1.2] Baumeister, B., T.A. Jung, and E. Meyer, *Tribological studies on fracture and erosion of nanostructures*. Tribology Letters, 2001. **11**(2): p. 107-110.
- [1.3] Kobayashi, T., I. Yamamoto, and M. Niinomi, *Evaluation of dynamic fracture toughness parameters by instrumented Charpy impact test*. Engineering Fracture Mechanics, 1986. **24**(5): p. 773-782.
- [1.4] Binnig, G., C.F. Quate, and C. Gerber, *Atomic Force Microscope*. Physical Review Letters, 1986. **56**(9): p. 930-933.
- [1.5] Eigler, D.M. and E.K. Schweizer, *Positioning single atoms with a scanning tunneling microscope*. Nature, 1990. **344**(6266): p. 524-526.
- [1.6] Falvo, M.R., et al., *Nanometre-scale rolling and sliding of carbon nanotubes*. Nature, 1999. **397**(6716): p. 236-238.
- [1.7] Hansen, L.T., et al., *A technique for positioning nanoparticles using an atomic force microscope*. Nanotechnology, 1998. **9**(4): p. 337-342.

2. FRACTURE MECHANICS – AN OVERVIEW

2.1. *Synopsis*

In fracture mechanics, the failure of components under the presence of static and/or dynamic forces is studied. In general, a fracture process can be divided into three stages: Initiation of fracture, movement of the crack front through a material (crack propagation), and the end of the fracture process either caused by complete destruction of the affected object or by stopping the crack propagation with a barrier such as a grain boundary. Mechanical load and the existence of one or more defects, where crack propagation is facilitated, are prerequisites for an evolving fracture incident. Defects can be introduced during manufacturing or during use, e.g. by cyclic exposure. Different types of defects are known such as inclusions, grain boundaries, dislocations, cracks or cavities. A fracture incident is determined by the geometrical and the mechanical conditions of the crack tip and further by the characteristic properties of the involved material. The individual types of fracture can roughly be divided into brittle fracture, fatigue fracture and ductile fracture. Numerous subdivisions and combinations of different types of fracture among each other are possible. A brief review of the history of fracture mechanics is found in [2.1].

2.2. *Brittle and ductile fracture*

The differentiation between brittle and ductile fracture is carried out by analyzing the deformation patterns on the newly created crack surfaces. During brittle fracture almost no surface deformation is observed. This type of fracture is common for glass, ceramics, stones, concrete, ice etc. but occasionally also found in alloys and metals (especially at low temperatures). The ductile fracture is characteristic for most metals and involves a strong plastic deformation of the newly created surfaces.

2.2.1. Brittle fracture

Brittle fracture describes the sudden appearance of a complete material failure (the crack propagation speed has sound velocity or even higher). Brittle materials are characterized in the stress-strain diagram by a steep linear line where no plastic deformation at the end of the fracture incident can be seen (Fig.2.1).

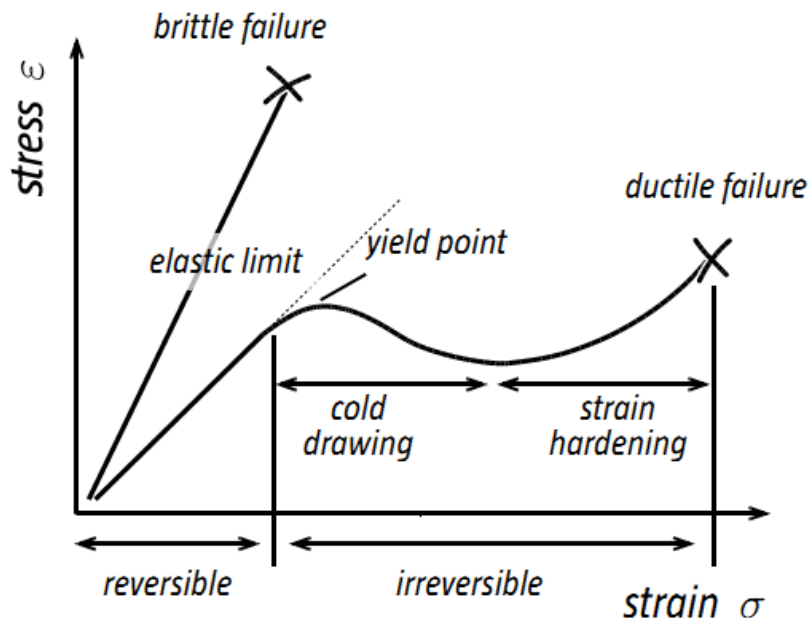


Fig.2.1: Stress-strain curves of a brittle (e.g. a ceramic) and a ductile material (e.g. a metal). The first curve (brittle) shows a steep and linear behavior which is similar to the one observed when a spring is compressed (Hooke's law). The second curve (ductile) shows a non-linear behavior after reaching a certain point (yield point). This behavior is caused by a ductile material transition to counteract the applied stress.

The beginning of the fracture process takes place on defect sites where tensions can accumulate. Brittle fracture can be detected based on the appearance of the fracture surface. In transcrystalline brittle fracture, the individual crystallites are split along related crystallographic planes (Fig.2.2a) but due to the different spatial orientation of the grains, the surface shows a furrow pattern.

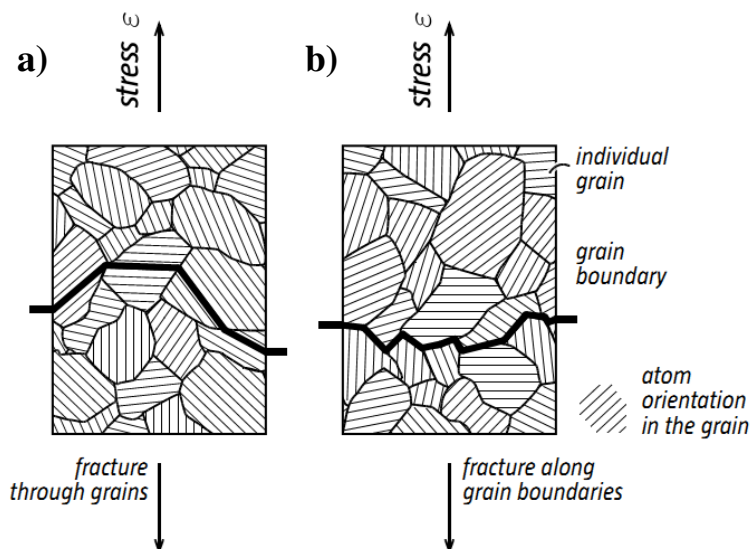


Fig.2.2: (a) Transcrystalline fracture course: The crack travels through the grains along certain crystallographic planes which show a weaker persistence against the moving crack front than other crystallographic planes. Due to the different spatial orientation of the individual grains, a furrow surface pattern will show up depending on the mean grain size. (b) Intercrystalline (transgranular) fracture course: The fracture front moves along the boundaries of the individual grains. The fracture surface of this type of brittle fracture normally shows a more flat crack pattern than in the transcrystalline case.

The intercrystalline (transgranular) brittle fracture runs alongside the grain boundaries and shows, depending on the grain size, a finer, less furrowed surface (Fig.2.2b). Another attribute for brittle fracture is the so-called Chevron pattern, which is frequently observed in brittle

breaking metals. It has different fracture layers which are located at different heights. The surfaces show a fan-like pattern starting from the crack origin expanding to the outside, with deep furrows and ridges. The Chevron pattern is an indicator for a brittle fracture induced by a sudden force impact (Fig.2.3).

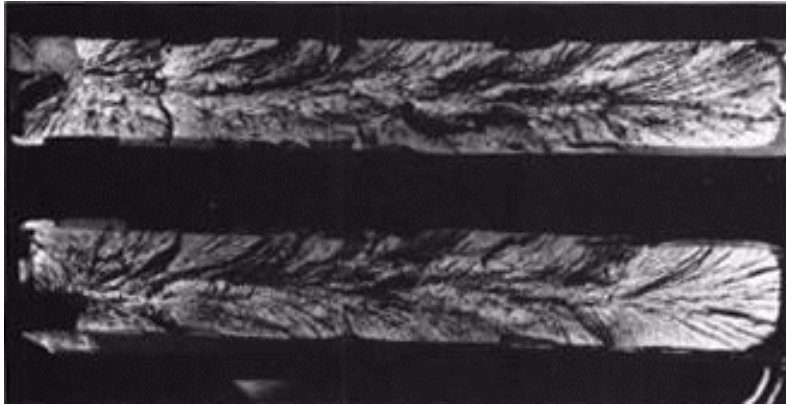


Fig.2.3: Chevron pattern on a steel rod: The Chevron pattern indicates an abrupt force load e.g. due to a hit. Chevron patterns only originate for brittle fracture processes and are more often observed in metals (Image taken from: [2.2]).

Brittle materials generally obey a much higher pressure resistance than tensile strength and are particularly sensitive to notches and cracks.

2.2.2. Ductile fracture

As already mentioned, a ductile behavior is mainly observed in metals. Ductile fracture occurs when a certain strain limit is reached. The ductile fracture is also known as honeycomb fracture according to its microscopic appearance (Fig.2.4). Ductile fracturing is favored by elevated temperatures, by uniaxial tension, and by soft materials as e.g. copper.

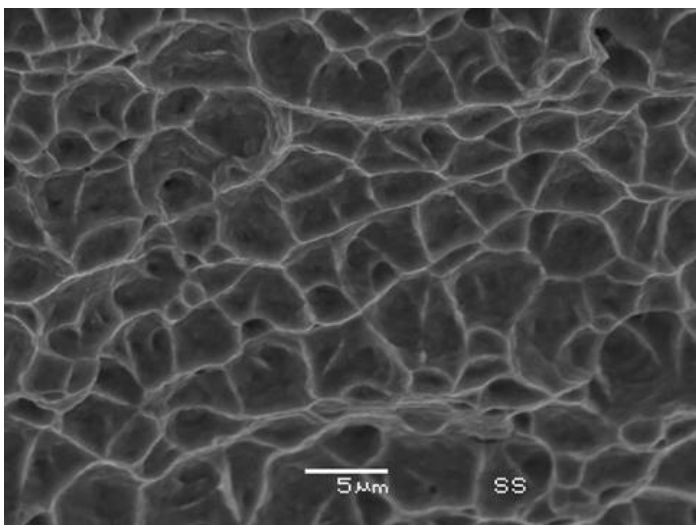


Fig.2.4: The displayed honeycomb-like pattern is formed due to the originating constrictions between inclusions/precipitates and the matrix material. The separation of particles from the matrix, by the applied strain forces, forms ellipsoidal cavities. If a critical number of voids is reached, the ribs between the cavities are broken off and the typical honeycomb-like structure appears (Image taken from: [2.3]).

2.3. Theoretical mechanical strength of solid bodies

Each solid body is held together by cohesive forces in-between the individual atoms. Therefore, the theoretical fracture strength of a body is the force needed to separate all atoms along an imaginary fracture plane. Fig.2.5 shows the interaction potential of two atoms in function of their distance. The distance d represents the equilibrium position and corresponds to the minima of the potential energy.

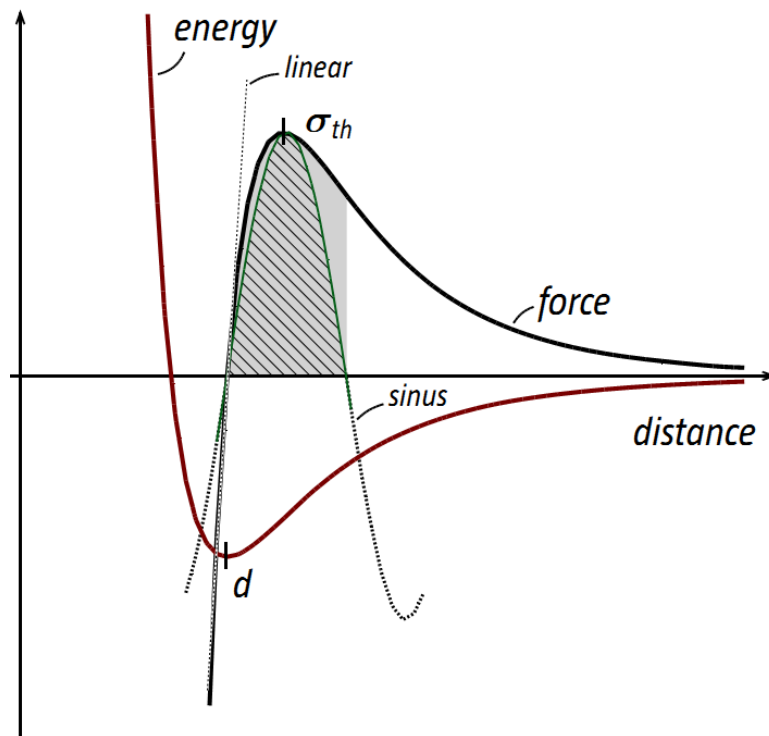


Fig.2.5: (energy) Potential curve between two atoms with the equilibrium distance d (minima). **(force)** First derivative of the potential curve which shows a maximum at the position of σ_{th} . **(sinus)** The force-distance-curve (per unit area) can be approximated by a sinusoidal curve fit. For very small deviations from the equilibrium position also a linear approximation is usable.

Any difference from the equilibrium distance d is denoted as x , σ_{th} is the theoretical force per unit area (stress) which is needed to separate the atoms from each other. As also illustrated in Fig.2.5, the force-distance curve can be approximated by a sinusoidal fit

$$\sigma = \sigma_{th} \cdot \sin \frac{2\pi x}{\lambda}, \quad (\text{Eq.2.1})$$

where λ means the period of the sinus function. For small values of x , a linear approximation can be used:

$$\lim_{x \rightarrow 0} \sigma = \frac{\sigma_{th} 2\pi x}{\lambda}. \quad (\text{Eq.2.2})$$

Comparably, Hooke's law can also be taken to express the uniaxial stress:

$$\sigma = E \frac{x}{d} \quad (\text{Eq.2.3})$$

where E corresponds to the modulus of elasticity (Young's modulus). It is notable that the E modulus is the only measurable quantity which directly represents cohesion forces. The combination of Eq.2.2 with Eq.2.3, rewritten for σ_{th} , results in the following equation:

$$\sigma_{th} = \frac{E\lambda}{2\pi d} \quad (\text{Eq.2.4})$$

With Eq.2.4, the calculation of σ_{th} is possible assuming that the entire work, used to separate the atoms, is converted into surface energy. Therefore, only elastic deformation, i.e. no plastic deformation, is taken into account. The work needed to separate the atoms (per unit area) is shown as shaded area in Fig.2.5 and will completely be converted (by definition) into surface energy (in this occasion two new surfaces were formed). Thus, integrating σ (Eq.2.1) from zero to $\lambda/2$, one obtains

$$\int_{x=0}^{\lambda/2} \sigma dx = \frac{\sigma_{th}\lambda}{\pi} := 2\gamma_0 \quad (\text{Eq.2.5})$$

where γ_0 expresses the surface energy of one of the two newly created surfaces. Rearranging Eq.2.5 to λ and inserting it into Eq.2.4 gives

$$\sigma_{th} = \sqrt{\frac{E\gamma_0}{d}} \quad (\text{Eq.2.6})$$

which allows the estimation of the theoretical tensile strength of brittle materials. The measured tensile strengths are generally lower than the calculated ones. Differences are caused by defects which weaken the material. Finally, values for the theoretical strength are not achievable because often other fracture mechanisms, e.g. plastic deformation of the crack tip, are involved during the fracture process.

2.4. *Fracture mechanics of the ideal brittle body (Griffith theory)*

The first analytical model for the mechanics of brittle fracture was developed in 1920 by Alan Arnold Griffith [2.4]. In this model, the internally stored potential (elastic) energy without a crack U_0 is associated to the potential energy of the system with a crack U , the external potential energy of the attached load W and the surface energy S of the crack which depends on its size. It follows that for a plate with a crack, a different amount of elastic energy is available, as there would be, without a crack:

$$U_0 = U + S + W . \quad (\text{Eq.2.7})$$

If the system is out of balance and the crack is allowed to expand, the instability criterion is fulfilled,

$$\frac{d}{da}(U + S + W) \leq 0 \quad (\text{Eq.2.8})$$

is given, with $2a$ the length of a crack. The formation of a crack leads to an energy release, i.e. the potential energy of a system is decreased. This energy is then available to enlarge the crack. The potential energy of a plate with infinite dimensions containing a crack is decreased by an amount of

$$\Delta U = \frac{\pi \sigma^2 a^2}{E} . \quad (\text{Eq.2.9})$$

Above expression is deduced from the elastic energy density formula and the expression by Kolosov (see [2.5] for more detailed information concerning this deduction). The work accomplished is equal to

$$W = \frac{\pi(1 + \kappa)}{8G} \sigma^2 a^2 \quad (\text{Eq.2.10})$$

and further also corresponds to the half quantity of U i.e. $U = -2W$. The Griffith fracture criterion, the critical stress that leads to fracture, can be calculated by the following relations

$$U + W = -\frac{\pi(1+\kappa)}{8G}\sigma^2 a^2 \text{ as well as} \quad (\text{Eq.2.11})$$

$$S = 4a\gamma_0 \quad (\text{Eq.2.12})$$

where G means the shear and κ the bulk modulus (bulk modulus in German means *Kompressionsmodul*) (Fig.2.6).

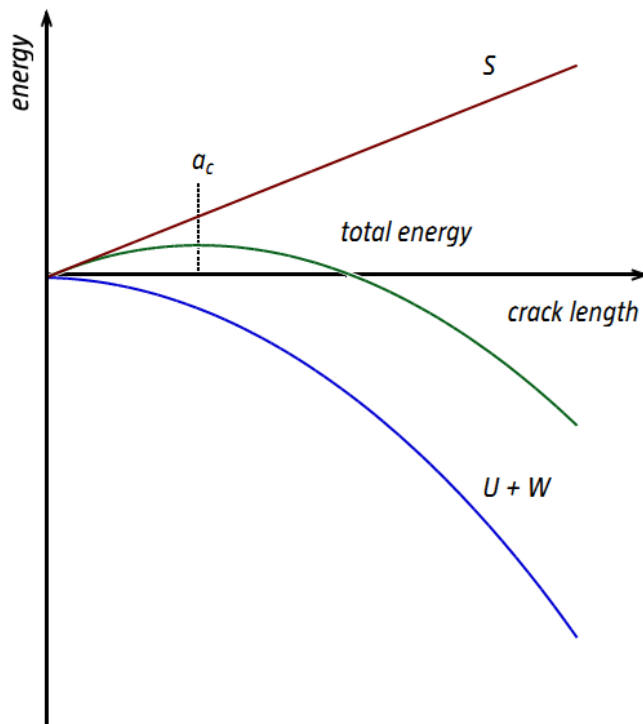


Fig.2.6: Potential energy diagram as a function of the crack length (the crack length is $2a$). The generation of new surfaces is energetically unfavorable because the production of surfaces consumes energy (linear dependency). However, if the crack length reaches a critical length a_c , the total energy gets reduced in such a way that any further crack growth decreases the potential energy which is favorable for the whole system (every system wants to reduce its stored potential energy (second law of thermodynamics)). This is caused by the $U+W$ term which represents the sum of the decreased potential energy (of a body with a crack) and the work done by the outside force.

If Eq.2.10 and Eq.2.11 are assembled into Eq.2.8 then the following equation can be obtained:

$$\frac{d}{da} \left(-\frac{\pi(1+\kappa)}{8G}\sigma^2 a^2 + 4a\gamma_0 \right) \leq 0 \text{ resp.} \quad (\text{Eq.2.13})$$

$$\frac{\pi(1+\kappa)}{4G}\sigma^2 a \geq 4\gamma_0 . \quad (\text{Eq.2.14})$$

Inserting the bulk modulus $\kappa=(3-\nu)/(1+\nu)$ and $E=2G(1+\nu)$ into Eq.2.13, one obtains the Griffith formula (for plane stress condition):

$$\sigma_c = \sqrt{\frac{2E\gamma_0}{\pi a}}, \quad (\text{Eq.2.15})$$

where ν is the Poisson's ratio which defines the ratio between the relative thickness change to the relative length change.

2.5. The three fundamental crack opening modes

In fracture mechanics, the stress conditions, directly at the crack tip, are of fundamental importance. According to George Rankine Irwin [2.6], the stress field can be described by one single factor, which only depends on the crack geometry and the externally applied load, called stress intensity factor K . There are three independent crack possibilities which are marked with I, II and III (Fig.2.7).

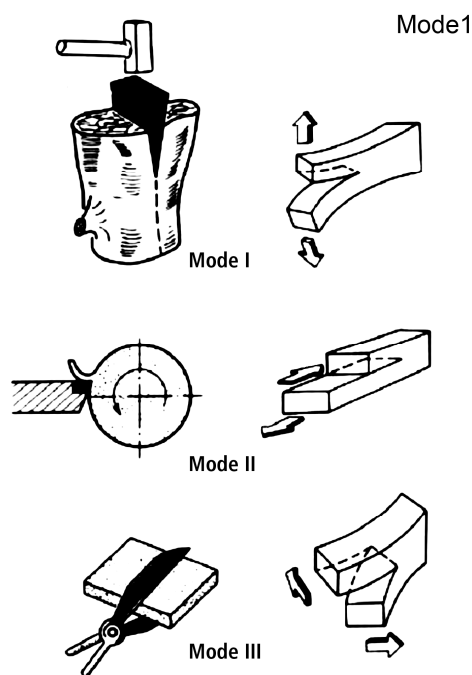


Fig.2.7: Here shown are the three different crack opening modes: Mode I is characteristic for tensile loads where the crack surfaces moves symmetrically in opposite directions relative to the crack level. Mode II corresponds to a plane shear stress state on the crack edges. The crack surfaces slide along the crack plane in opposite directions to each other. Mode III corresponds to the non-planar shear stress state. The crack surfaces are shifted antisymmetrically along the crack level to each other, but perpendicular to the crack direction. This case occurs for shear and torsional loads (Image taken from: [2.7]).

Case I is typical for tensile loads i.e. the crack surfaces are moving symmetrically relative to the crack level. This mode is true for Griffith-type cracks and further also for surface cracks which are exposed to uniaxial forces. Case II corresponds to a plane shear stress state on the edges of a crack. The crack surfaces slide alongside the crack level but in opposite directions to each other. Case III corresponds to the non-planar shear stress state: The crack surfaces are shifted antisymmetrically in the same level as the crack but perpendicular to the crack direction. This case especially occurs for shear and torsional loads.

The stress intensity factors are deducible from the complex stress functions of Kolosov and Muskhelishvili. For a load-free Griffith crack of length $2a$ on an infinitely large plate under uniaxial tension, the following relationship can be written:

$$K_I = \sigma\sqrt{\pi a} , K_{II} = K_{III} = 0 . \quad (\text{Eq.2.16})$$

For a Griffith crack in an infinite large plate on which a shear force is acting, an analogous relationship was found:

$$K_{II} = \tau\sqrt{\pi a} , K_I = K_{III} = 0 , \quad (\text{Eq.2.17})$$

whereas for an opening tunnel-shaped crack in an infinite prismatic body under longitudinal shear the relation

$$K_{III} = \tau\sqrt{\pi a} , K_I = K_{II} = 0 \quad (\text{Eq.2.18})$$

was found where τ denotes the shear stress.

2.6. Fracture mechanics on the nanoscale and other size effects

In the macroscopic world, many physical properties and characteristics appear to be of constant nature. If one reduces the size of a body, the properties believed to be constant begins to change, when reaching the nanometer scale. A well known example for this is the melting point variation of gold particles [2.8]. It was found that particles beyond 20 nm in diameter will drastically change their melting points as seen in Fig.2.8. This means that a gold particle of about 5 nm in diameter has a melting point which is about 200 K lower than the melting point for bulk gold (T_m for bulk gold is about 1337 K).

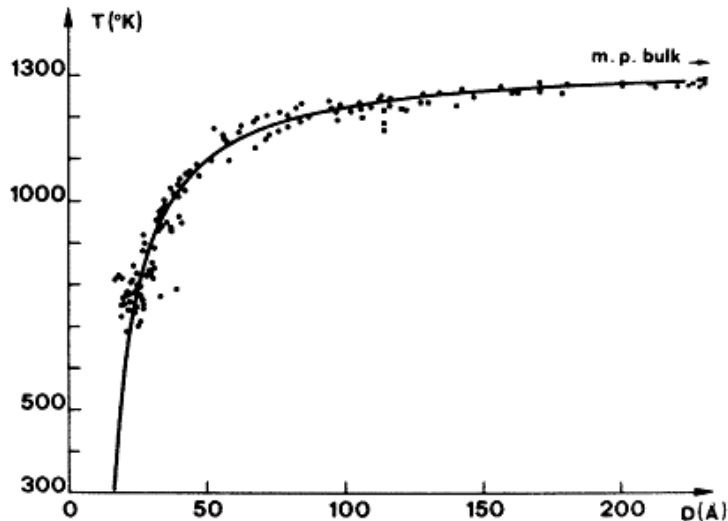


Fig.2.8: Experimental values of the melting-point temperatures of gold particles in function of their diameter. The melting point temperature decrease is caused by the changing surface-to-volume atom ratio: Surface and bulk atoms are different in terms of their stored potential energy. Surface atoms exhibit a lower symmetry than bulk atoms and hence a higher energy content (image taken from [2.8]).

This remarkable effect occurs because the particle energy is defined by the different energy states of the involved atoms i.e. surface and bulk atoms. The surface atoms increase the total energy of the system while the atoms in the volume lead to a reduction. As a result of the changing surface-to-volume ratio (the smaller the particles, the higher the surface-to-volume ratio), the total energy function contains a maxima quite similar to the one as shown in Fig.2.6. This will destabilize small particles and thus decrease their melting points.

Size effects also have an impact on the mechanical properties which are mainly determined by the presence of bulk defects such as e.g. dislocations. Therefore, the chance to find a defect-free object is increased, as when the object volume is smaller than the typical defect density of a chosen material. Existing dislocations make a material hard but also brittle because they inhibit intercrystalline slip processes needed for ductility and thus reduce the yield strength. The same principle is valid for crystallites respectively their grain boundaries: In a fracture process, the crack front moves along the force gradient until it meets a grain boundary or another obstacle. If this happens, the expanding crack has to choose if it moves through the crystallite or if it goes alongside the grain boundary. In any case, the crack is losing energy which is why defects, such as e.g. grain boundaries, enhance the mechanical strength. Strengthening of a polycrystalline material thus can be controlled by the mean size of the crystallites. This finding was proven valid for e.g. silver, copper, and palladium [2.9, 2.10]. This phenomenon is called Hall-Petch effect [2.11, 2.12] which can be mathematically written as follows:

$$\Delta\tau = \frac{k_{HP}}{\sqrt{D}} \quad (\text{Eq.2.19})$$

Here, the shear stress difference $\Delta\tau$ is associated with the average grain diameter D , k_{HP} is the Hall-Petch parameter i.e. a material constant. The above relationship suggests that the strength, expressed by the shear stress difference, increases continuously as long as the grain size decreases. However, this is not always the case: Below a certain grain size, the strength can decrease again. This phenomenon is called inverse Hall-Petch effect [2.13] and is not yet fully understood (Fig.2.9). The inverse Hall-Petch effect is observed for most polycrystalline materials.

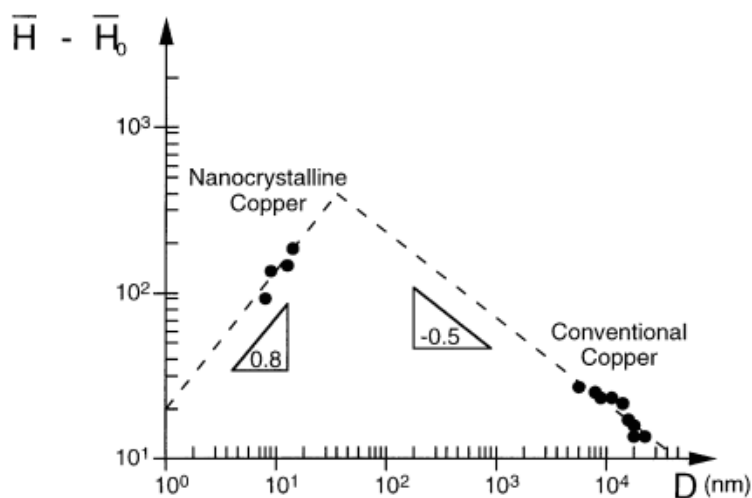


Fig.2.9: Inverse Hall-Petch behavior in nanocrystalline copper ($\bar{H}-\bar{H}_0$ denotes the hardness increment, D the grain size). The classical behavior breaks down at a grain size of about 50 nm (image taken from [2.14]).

It was observed that below a certain grain size, the brittle behavior disappears and plastic behavior are showing up [2.15]. This behavior, called inverse Hall-Petch phenomenon, may be explained by a diffusive flow of atoms along the grain boundaries. Since the grains are very small, the majority of atoms are placed at positions of the grain boundary. For further information, an informative review of size effects and their influence on the mechanical as well as the magnetic properties was written by Arzt [2.14].

2.7. References

- [2.1] Razvan, R., *Some remarks on the history of fracture mechanics*. Proceedings of the 3rd Int Conf on Applied Mathematics, Circuits, Systems, and Signals/Proceedings of the 3rd Int Conf on Circuits, Systems and Signals, ed. P. Pardalos, et al.2009, Athens: World Scientific and Engineering Acad and Soc. 122-131.
- [2.2] Callister, W.D., *Material Science and Engineering: An Introduction*, 1999, John Wiley & Sons Inc.: New York.
- [2.3] Sudhakar, K.V. and T. Majewski, *Undergraduate Teaching of Biomaterials*, International Journal of Modern Engineering, 2004. **4**(2).
- [2.4] Griffith, A.A., *The Phenomena of Rupture and Flow in Solids*. Philosophical Transactions of the Royal Society of London, 1920. **221**: p. 163-198.
- [2.5] Hahn, H.G., *Bruchmechanik: Einführung in die theoretischen Grundlagen*, 1976, B.G. Teubner: Stuttgart.
- [2.6] Irwin, G.R., *Analysis of stresses and strains near the end of a crack traversing a plate*. Journal of Applied Mechanics, 1957. **24**(31): p. 361–364.
- [2.7] Parton, V.Z., *Fracture mechanics: from theory to practice*, 1992: Gordon and Breach Science Publishers: New York.
- [2.8] Buffat, P. and J.P. Borel, *Size effect on the melting temperature of gold particles*. Physical Review A, 1976. **13**(6): p. 2287-2298.
- [2.9] Ma, Q. and D.R. Clarke, *Size dependent hardness of silver single crystals*. Journal of Materials Research, 1995. **10**(4): p. 853-863.
- [2.10] Nieman, G.W., J.R. Weertman, and R.W. Siegel, *Mechanical behavior of nanocrystalline Cu and Pd*. Journal of Materials Research, 1991. **6**(5): p. 1012-1027.
- [2.11] Hall, E.O., *The Deformation and Ageing of Mild Steel: III Discussion of Results*. Proceedings of the Physical Society of London Section B, 1951. **64**(381): p. 747-753.
- [2.12] Petch, N.J., *The cleavage strength of polycrystals*. Journal of the Iron and Steel Institute, 1953. **174**(1): p. 25-28.
- [2.13] Chokshi, A.H., et al., *On the validity of the Hall-Petch relationship in nanocrystalline materials*. Scripta Metallurgica, 1989. **23**(10): p. 1679-1683.
- [2.14] Arzt, E., *Size effects in materials due to microstructural and dimensional constraints: A comparative review*. Acta Materialia, 1998. **46**(16): p. 5611-5626.
- [2.15] Karch, J., R. Birringer, and H. Gleiter, *Ceramics ductile at low temperature*. Nature, 1987. **330**(6148): p. 556-558.

3. INTRODUCTION TO SCANNING FORCE MICROSCOPY

3.1. Synopsis

The SFM technique is strongly based on the inventions related to Scanning Tunneling Microscopy (STM). The development of the STM in 1981 [3.1, 3.2] earned its inventors, Gerd Binnig and Heinrich Rohrer, the Noble Prize in physics in 1986. In the same year, Gerd Binnig, Calvin Quate and Christoph Gerber presented their first paper on SFM [3.3]. In STM, the current, originating from the quantum tunneling effect, through a dielectric is measured while in SFM the forces acting between a cantilever tip and a probed sample surface are exploited. Both methods, as well as nearly all members of the Scanning Probe Microscopy (SPM) family, have in common, that the underlying interactions have near-field character. By this, the resolution limits of traditional far-field techniques as e.g. optical microscopy can be overcome.

3.2. Common SFM concepts

The main physical principle of SFM is the repulsive interaction force between the outermost atom of the preferably atomically sharp scanning tip and the directly underlying atom of the sample surface. This interaction is determined by the Coulomb repulsion of the negatively charged electron clouds of the involved atoms. An even stronger short-range interaction is caused if atomic orbitals, i.e. the corresponding electron wave functions, are overlapping each other while containing electrons with the same set of quantum states (known as strong or positive overlap). In this case a very strong repulsion is provoked which is known as Pauli repulsion. Thus, SFM is often referred to as Atomic Force Microscopy (AFM). In SFM, unfortunately, also long-range interactions are present, namely van der Waals, electrostatic and capillary forces between the mesoscopic tip and the sample surface. This discriminates SFM from STM where only the short-range interaction of the distance dependent exponential-tunneling-current-decrease is dominant. This explains the better resolution capabilities of STM compared to SFM. On the other hand, the SFM technique is not limited to conducting samples which in turn makes the SFM so popular and widely

applicable. The cantilever, which acts as the actual force sensor behaves analogous to a conventional spring and can therefore be described according to Hooke's law:

$$F_N = k_N \cdot \Delta z , \quad (\text{Eq.3.1})$$

where F_N (in N) denotes the force, k_N is the spring constant (in N/m) and Δz means the displacement (in m) of the free end of the cantilever from its equilibrium position. In the contact mode of the SFM, the tip is in close contact during scanning and the bending of the cantilever and therefore the force is kept constant by a feedback loop system. In the more commonly used dynamic modes, the oscillation frequency is often maintained constant. If an SFM tip is approached to a surface it will pass through a potential minimum. This potential (U_{LJ}) can be described by the Lennard-Jones (LJ) potential (Fig.3.1):

$$U_{LJ}(r) = U_0 \left[\left(\frac{r_0}{r} \right)^{12} - 2 \left(\frac{r_0}{r} \right)^6 \right] , \quad (\text{Eq.3.2})$$

where U_0 is the depth of the potential well, r is the actual atom distance and r_0 is the distance at which the potential reaches its minimum. In this potential the r^{-12} term describes the repulsive forces whereas the r^{-6} term represents the attractive forces. Because of these two terms, the LJ potential is also often referred to as the 6-12 potential. With this potential function, the overall interaction between two identical and chemically inert atoms (e.g. argon) is modeled.

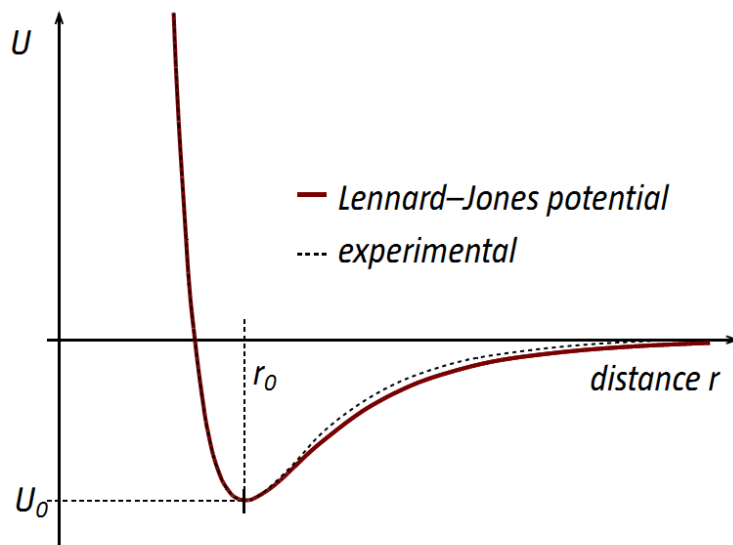


Fig.3.1: The Lennard-Jones (LJ) potential describes the potential when two chemically inert and uncharged atoms are approached to each other. This potential is also used to qualitatively describe the approach process between an SFM tip and a sample surface.

However, in SFM the situation is far more complex than the one depicted in figure 3.1. Due to the geometry of the cantilever tip (pyramidal cone which is defined by the Si(111) crystallographic planes) a multitude of atoms is interacting with the sample surface. Due to the longer distance of this assembly of atoms to the surface, only long range interactions are involved. By contrast, short range interactions dominate for the tip's outermost atom. This causes an inverted force vector in respect to the force vector of the outermost atom (Fig.3.2).

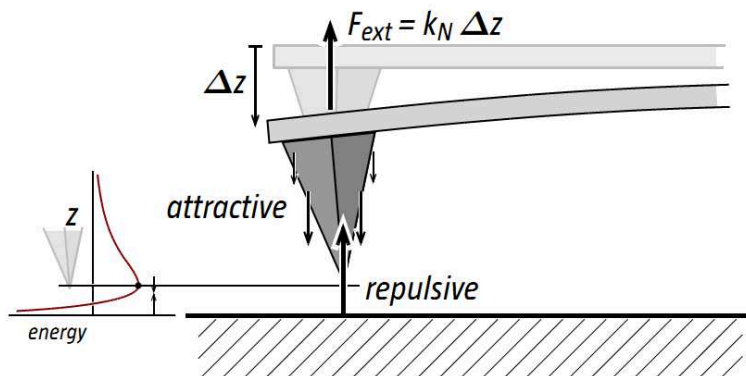


Fig.3.2: Cantilever tip after snap-in: The forces are balanced, i.e. the attractive long range forces are compensated by the occurring repulsive short range forces provoked by the decreasing tip-sample distance. Due to the attractive forces in the beginning of the approach process, the cantilever is bent towards the sample surface. An opposing force is caused by the stressed cantilever, i.e. according to Hooke's law.

3.3. The scanning probe

The scanning probe in SFM is mounted onto the free end of a silicon bar i.e. a so-called cantilever. As mentioned above, the cantilever is the actual force sensor which, in a

normal and/or in a torsional direction, will measure the load acting on the cantilever tip by the degree of bending. The whole cantilever is made out of highly doped (p⁺) single crystalline silicon. This doping is required to improve the capability to dissipate static charges because otherwise gradual charging i.e. tribocharging would induce a drift. While the cantilever is made of silicon, the tip, especially for contact mode cantilevers, is often coated with e.g. silicon dioxide (SiO₂), silicon nitride (Si₃N₄) or diamond like carbon (DLC) to prevent destructive abrasion due to the enhanced friction forces. Furthermore, the tip geometry i.e. the angle between the probed surface and the cantilever tip, the opening angle of the tip itself and the distortion of the tip apex are crucial for the topographic resolution. The resolution is reduced if topographical sample features (e.g. cavities or steep edges) have a size comparable to the size of the tip apex (tip broadening effect) [3.4].

3.4. Piezoceramic actuators

Because even the best stepper motors have a limited accuracy and sensitivity, piezoelectric actuators were used in SFM setups. Nowadays, piezoelectric tube scanners are mostly used while in the beginning of SPM tripods were popular. Here, the linear expansion (Δz) and the bending ($\Delta x, y$) of a segmented piezoelectric tube scanner as a function of the electric field applied across them is utilized (inverse or indirect piezoelectric effect). The applied electrical field (E) and the relative strain ($S = \Delta l/l$) are linked through a piezoelectric strain constant d (d_{33} for the longitudinal, d_{31} for the transverse and d_{15} for the shear piezoelectric effect):

$$S(E) = d \cdot E \quad . \quad (\text{Eq.3.3})$$

The used piezoceramic materials, e.g. lead zirconate titanate (PZT: $\text{Pb}[\text{Zr}_x\text{Ti}_{1-x}]\text{O}_3$, $0 < x < 1$) are operated in the transverse way, i.e. the relative strain perpendicular to the direction of its polarization (P) is related to an electrical field in the direction of the polarization. The voltage (U) dependent displacement ($\Delta x, \Delta y, \Delta z$) of a piezotube scanner can be described as follows:

$$\Delta z = \frac{d_{31} \cdot U_z \cdot l}{h}, \quad \Delta x, y = \frac{2\sqrt{2} \cdot d_{31} \cdot U_{x,y} \cdot l^2}{\pi \cdot D \cdot h}, \quad (\text{Eq.3.4, Eq.3.5})$$

where D is the average diameter, l is the length and h is the wall thickness of the piezotube scanner [3.5]. Since the piezoelectric effect is time dependent, creeping of the actuator is often observed, especially when a sudden change of the driving voltage is applied. This behavior hinders the accurate positioning of the scan tip under certain circumstances, because the actuator is elongated up to a certain level and then slowly creeps to the final expansion length. The time dependent deformation follows a logarithmic law:

$$\Delta l(t) = \Delta l_0 \cdot \left(1 + \gamma \cdot \log \left\{ \frac{t}{0.1s} \right\} \right). \quad (\text{Eq.3.6})$$

In the equation above, Δl_0 is the deformation after 100 ms and γ is a constant which typically will take a value between 0.01 and 0.02.

3.5. *Relevant forces*

As shown, the short range forces are composed of the repulsive Coulomb interaction of the negatively charged electron clouds and the Pauli repulsion. Nevertheless, under certain conditions, the overlap of the electron wave functions of the outer shell electrons of an atom or a molecule can also lead to a total energy decrease which in turn is equivalent to a covalent (chemical) bond [3.6]. Apart from these forces, the remaining forces are attractive and exhibit long-range character. The long-range forces are classified into van der Waals, electrostatic, and capillary forces. Furthermore, also magnetic forces and forces which only arise in liquids e.g. solvation forces are observable.

3.5.1. Van der Waals forces

The term “van der Waals” forces refers to relatively weak non-covalent interactions between atoms or molecules whose interaction energy decreases with approximately the sixth power of the distance. The van der Waals forces can be divided into three components: Interactions between permanent dipoles (Keesom forces), interactions between a permanent dipole and a polarizable molecule (Debye forces) and interactions between molecules which are polarizable and which, because of electron density fluctuations, will mutually induce short-life dipoles (London forces).

3.5.2. Electrostatic forces

Electrostatic forces appear when the tip and the sample, respectively isolated domains on the sample surface, are differently charged, i.e. on a different electrical potential. The strength of this force can be estimated by Coulomb's law:

$$F(r) = \frac{Q_1 \cdot Q_2}{4 \cdot \pi \cdot \epsilon \cdot r^2} , \quad (\text{Eq.3.7})$$

where Q denotes the individual point charges (in C), r is the separation distance (in m) and ϵ is the permittivity (in F/m). In contact mode SFM, the different potentials will equilibrate upon contact. This becomes noticeable by a drift phenomenon because the potential equilibration is time dependent i.e. the potential change follows a delay proportional to the resistivity of the sample [3.7].

3.5.3. Capillary forces

Capillary forces are present while measuring in air or generally in a humid atmosphere. When tip and sample are in contact, the water in the overlapping region is displaced and accumulates at the edge of the contact area forming a meniscus. Assuming that the water film thicknesses h are equal for both the tip and the surface, one can estimate the capillary force by

$$F(D) = \frac{4 \cdot \pi \cdot R \cdot \gamma_{H_2O} \cdot \cos \theta}{1 + \frac{D}{d}} , \quad (\text{Eq.3.8})$$

where γ_{H_2O} denotes the liquid-vapor interfacial energy of water, R corresponds to the radius of a sphere fitted into the tip apex and D stands for the tip-sample distance [3.8]. The lower case d can be expressed by $d = R(1 - \cos \phi)$ and stands for the meniscus height subtracted with D (Fig.3.3).

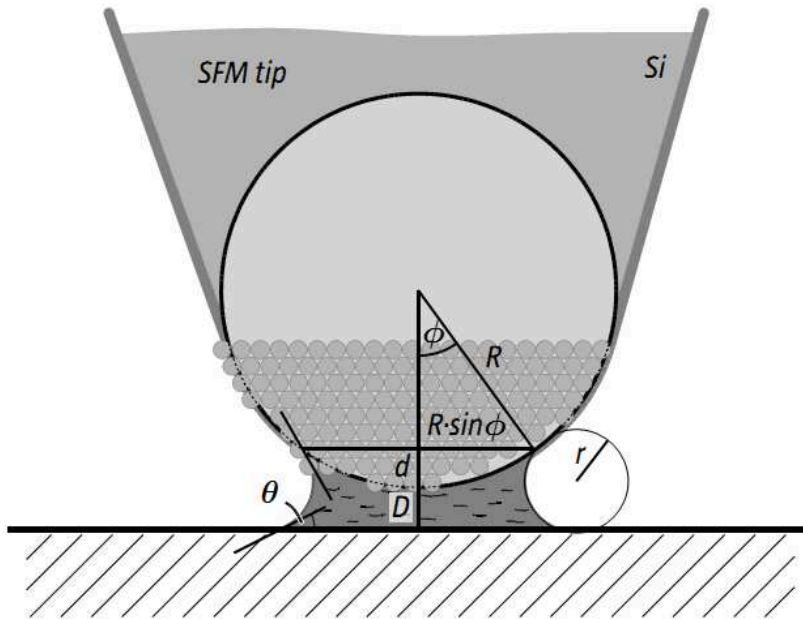


Fig.3.3: Schematic drawing representing the merged surface water films i.e. the formation of a meniscus. The tip apex is modeled by a fitted sphere defined by its radius R . The meniscus arises from the displaced water which then gets accumulated at the edge zone of the sphere. D stands for the tip-sample distance while the lower-case d denotes the height of the meniscus relative to the sphere radius R . The sum of D and d connotes the total meniscus height.

3.5.4. Forces in liquids

In liquids, the long-range forces are strongly modified: If the whole cantilever and its tip are immersed in the liquid together with the sample, no water/air interfaces and correspondingly no capillary forces are present. The van der Waals forces on the other hand depend crucially on the polarizability of the electron shell which is reduced by shielding in a medium which is polarizable by itself, like water. Since these two forces are the predominant contributors responsible for adhesion, the adhesion is significantly reduced or almost diminished. This behavior can clearly be observed by recording a force vs. distance curve: The snap-in and snap-out points (see Fig.3.6 for a visual explanation) are at the same location which means that there is no big difference between these two which eliminates the hysteresis between the approach and the withdraw process. Beside this, there are also forces which will only arise in liquids. When electrolytes are solved in the liquid and also when the involved surfaces i.e. the surface of the cantilever tip and/or the sample surface are charged, an electrical double layer is formed. The electrical double layer in contact with another electrical double layer or at least a polarizable surface will induce, upon contact, a repulsive force.

3.6. Force sensing

The actual cantilever height is derived from the signal of a four-quadrant photodiode detector by means of a reflected laser beam (Fig.3.4). When probing the sample topography, the cantilever bending (vertical and torsional) is changed. Simultaneously the position of the reflected laser beam reaching the photo sensitive detector (PSD) is shifted. The resulting difference signals between the coupled photodiodes are then used as the control variable for adjusting the cantilever height, i.e. for the height signal

$$\Delta I_z = (I_1 + I_2) - (I_3 + I_4) \quad \text{and} \quad (\text{Eq.3.9})$$

$$\Delta I_L = (I_1 + I_4) - (I_2 + I_3) \quad (\text{Eq.3.10})$$

for the lateral signal. In a next step, the recorded difference signal is normalized by the sum of all photodiode currents and further sampled and digitized in an A/D converter. The digitized values are processed in a computer by the pre-entered integral and proportional parameters and then fed back into the controller where the signal is again converted by a D/A converter.

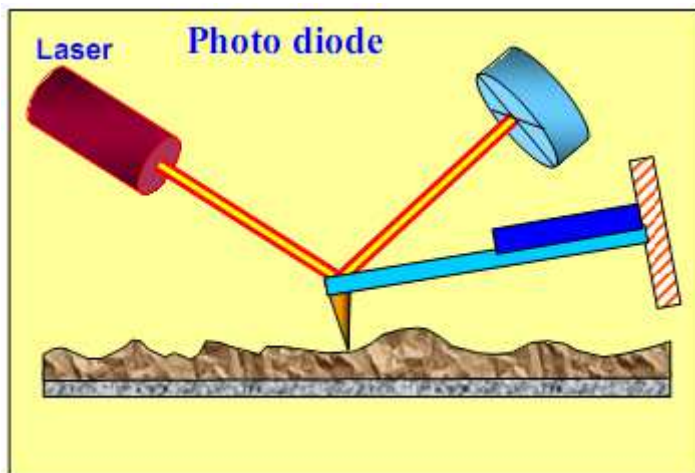


Fig. 3.4: Schematic structure of the core components of an AFM: The cantilever with the tip at the free end is scanned over a sample surface. Due to the sample topography the cantilever gets bent and accordingly the beam path of the reflected laser beam is changed. This causes a voltage difference in the photo cell. The voltage difference used for the piezoactuator is proportional to the height difference of the sample surface and is therefore used as the height indicator (Image source: [3.9]).

3.7. Force calibration

The measurable SFM signal output comes from the PSD and is a current signal which gets converted into a voltage by a current-to-voltage converter. A precise calibration is needed

to convert this signal into a quantitative force value. This has to be done independently for each of the two occurring forces i.e. for the normal as well as for the lateral force components. In figures 3.5a, the reflected laser beam in normal direction is deflected according to the topography while for the vertical signal (see figure 3.5b) frictional forces are responsible.

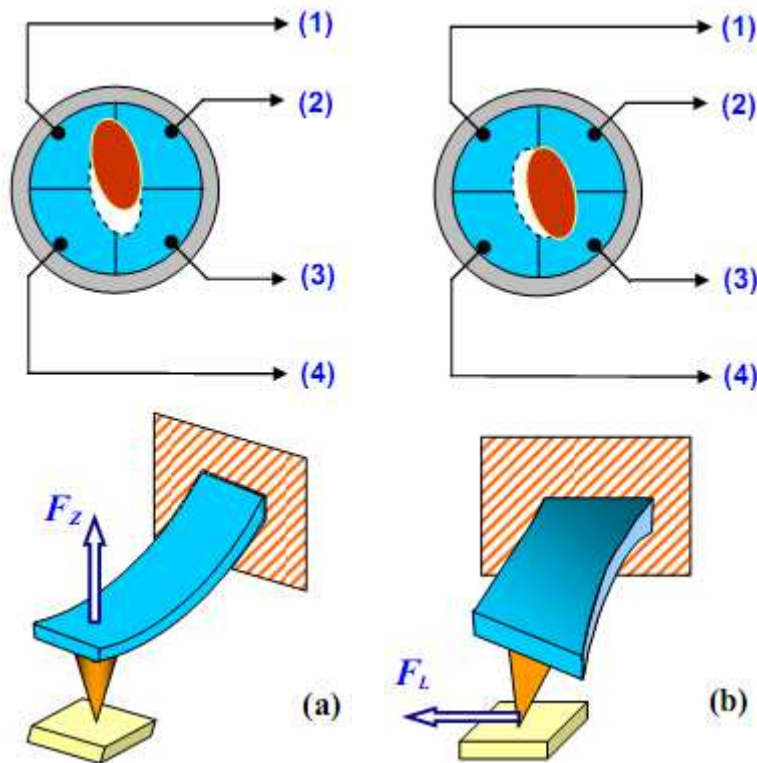


Fig.3.5: The measurement principle of the normal and lateral components through the deflection signal of a reflected laser beam: A topographical sample variation bends the cantilever in the z-direction which leads to a changed signal between the upper and lower photodiodes (a). Deviations in the material composition, or also if the cantilever tip is pushed against an object, leads to different cantilever twists. This effect deflects the laser beam in the horizontal direction (b). If the scan direction is switched, the sign of the lateral signal is changed as well. The numbers in brackets denote the individual segments of the PSD (Image source: [3.9]).

3.7.1. Normal force calibration

The normal loading force is simply calculated using Hooke's law (see equation 3.1). The displacement of the free end of the cantilever from its equilibrium position is determined by multiplying the deflection sensitivity (in nm/V) by the applied setpoint (in V). The setpoint is defined as the PSD signal difference when the cantilever is far away from the surface and when it is at setpoint i.e. "0V and 3V" or "-1V and 2V" would be equivalent setpoints. The deflection sensitivity itself is derived from such a calibration experiment (see Fig.3.6) by measuring the slope of the linear regime observed after the snap-in point. In order to get a deflection sensitivity in nm/V, the tip-sample displacement must be converted into length units by a piezotube scanner calibration. According to Hooke's law, the so derived cantilever displacement only needs to be multiplied by the spring constant as denoted by the cantilever manufacturer. Unfortunately, these nominal values differ from the true values, in some cases

by a factor of two. The spring constant determination can be carried out when the geometrical dimensions and the mechanical properties of the cantilever are known. A more accurate method is given by [3.10] where the resonance frequency is used:

$$k_N \cong \frac{2\pi^3 w (f_0 L \sqrt{\rho})^3}{\sqrt{E}} \quad (\text{Eq.3.9})$$

In above equation, w stands for the width of the cantilever, f_0 for the resonance frequency, L is the length of the cantilever, ρ is the density ($\rho(\text{Si}) = 2336 \text{ kg/m}^3$) and E the elastic modulus of silicon ($E(\text{Si}) = 176 \text{ GPa}$). An improved version of this equation [3.11] uses a value of 59.3061 instead of the $2\pi^3$ term.

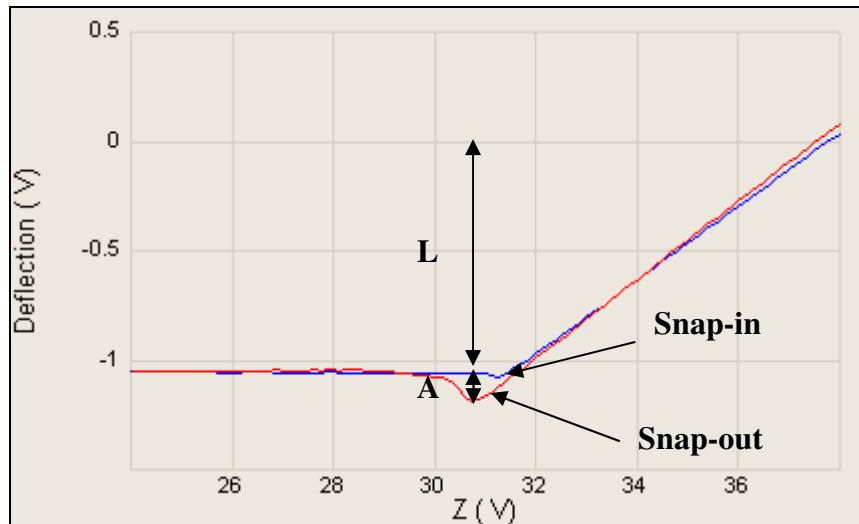


Fig.3.6: Typical force vs. distance curve received from a calibration experiment: The piezo-sample displacement x-axis must first be converted into length units by the data gained from a piezotube scanner calibration. The setpoint value is represented by the deflection signal (L) when the cantilever tip is not in contact with the sample i.e. far away from the sample surface. The blue curve represents the approach, the red curve the withdraw process. After snap-in (small bump before the blue curve changes from a horizontal to a sloped behavior) the cantilever becomes linearly compressed (Hooke's law). The slope of the curve represents the deflection sensitivity (in nm/V). By multiplying the deflection sensitivity with the setpoint value (in V) one gets the displacement from the free end of the cantilever relative to its equilibrium state. Due to adhesion forces, the snap-out position is different from the snap-in position. The difference in deflection signals corresponds to the adhesion forces (A).

3.7.2. Lateral force calibration

The lateral force calibration is based on the determination of a calibration factor α . This factor converts the halved friction loop signal W (see Fig.3.7 and its caption for an explanation) into a lateral force:

$$F_L = \alpha \cdot W \quad (\text{Eq.3.10})$$

The determination of α uses the improved wedge calibration method from Varenberg et al [3.12] which is based on the method of Ogletree et al [3.13]. The so derived calibration factor is only valid for the currently used setup i.e. the used cantilever and the position of the laser spot on it. If the cantilever is scanned across a sample surface and it changes its scan direction i.e. from left to the right, the sign of the lateral signal gets inverted (Fig.3.7).

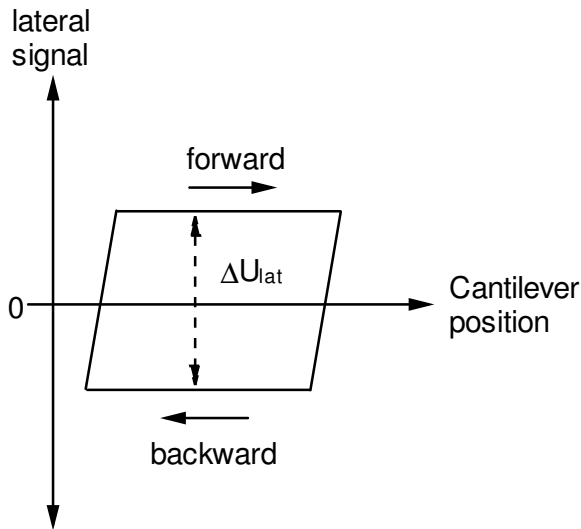


Fig.3.7: Schematic drawing of the lateral signal according to the scan direction which is also known as friction loop. The signal refers to a flat and homogeneous surface with constant scan conditions. The lateral signal changes its sign when switching between back-and forward direction. Half of this friction loop signal is proportional to the friction force during scanning F_L .

The wedge calibration method is based on the measurements of two chemically identical surfaces which are arranged by a given angle θ (in radians) to each other. With θ and the friction loop half W for the flat and the sloped surface and the friction loop offset Δ the following expression can be found for the friction coefficient μ_s for the sloped surface (see Fig.3.8):

$$\sin \theta (L \cos \theta + A) \mu_s^2 - \frac{\Delta_s - \Delta_f}{W_s} (L + \cos \theta) \mu_s + L \sin \theta \cos \theta = 0 \quad (\text{Eq.3.11})$$

The quadratic equation has two solutions but only the one which satisfies the $\mu < \tan\theta$ condition is usable. With the derived friction coefficient for the sloped surface, the universal force factor α can then be calculated according to

$$\alpha = \frac{\mu_s (L + A \cos \theta)}{W_s (\cos^2 \theta - \mu_s^2 \sin^2 \theta)} \quad (\text{Eq.3.12})$$

With α every single scan point signal can be converted into a friction force F_L as long as the setup was not changed. Otherwise the system must again be calibrated. Through the relationship

$$\mu = \frac{F_L}{F_N} \quad (\text{Eq.3.13})$$

(second law by Amontou) the friction coefficient can also be determined.

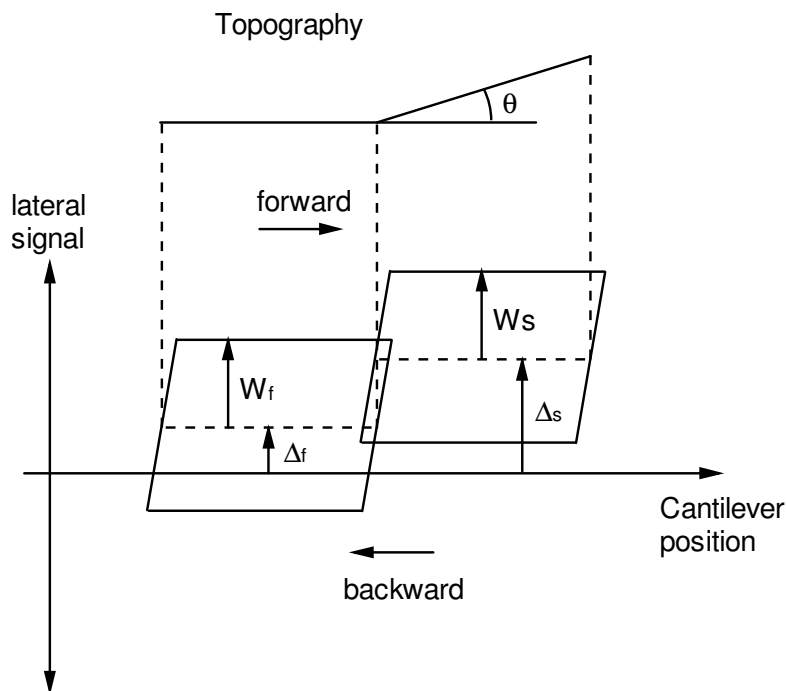


Fig.3.8: Drawing of the 'friction loops' (schematic) in function of the topography. W indicates the half height of the friction loop (subscript f stands for flat and subscript s for slope). The Δ stands for the friction loop offset and θ denotes the angle between the horizontal and the sloped surface.

3.8. References

- [3.1] Binnig, G. and H. Rohrer, *Scanning Tunneling Microscopy*. Helvetica Physica Acta, 1982. **55**(6): p. 726-735.
- [3.2] Binnig, G., et al., *7 × 7 Reconstruction on Si(111) Resolved in Real Space*. Physical Review Letters, 1983. **50**(2): p. 120-123.
- [3.3] Binnig, G., C.F. Quate, and C. Gerber, *Atomic Force Microscope*. Physical Review Letters, 1986. **56**(9): p. 930-933.
- [3.4] Villarrubia, J.S., *Algorithms for scanned probe microscope image simulation, surface reconstruction, and tip estimation*. Journal of Research of the National Institute of Standards and Technology, 1997. **102**(4): p. 425-454.
- [3.5] Colton, R.J., et al., *Procedures in Scanning Probe Microscopies 1998*, Chichester (New York): Wiley.
- [3.6] Meyer, E., H.J. Hug, and R. Bennewitz, *Scanning Probe Microscopy: The Lab on a Tip*. Advanced texts in physics 2004, Berlin: Springer.
- [3.7] Bennewitz, R., M. Reichling, and E. Matthias, *Force microscopy of cleaved and electron-irradiated CaF₂(111) surfaces in ultra-high vacuum*. Surface Science, 1997. **387**(1-3): p. 69-77.
- [3.8] Israelachvili, J.N., *Effect of Capillary Condensation on Adhesion*, in *Intermolecular and surface forces* 1991, Academic Press London. p. 330-334.
- [3.9] Mironov, V.L., *Fundamentals of Scanning Probe Microscopy* 2004, Nizhny Novgorod: The Russian Academy of Sciences.
- [3.10] Tortonese, M. and M. Kirk, *Characterization of application specific probes for SPMs*, in *Micromachining and Imaging*, T.A. Michalske and M.A. Wendman, Editors. 1997, Spie - Int Soc Optical Engineering: Bellingham. p. 53-60.
- [3.11] Clifford, C.A. and M.P. Seah, *The determination of atomic force microscope cantilever spring constants via dimensional methods for nanomechanical analysis*. Nanotechnology, 2005. **16**(9): p. 1666-1680.
- [3.12] Varenberg, M., I. Etsion, and G. Halperin, *An improved wedge calibration method for lateral force in atomic force microscopy*. Review of Scientific Instruments, 2003. **74**(7): p. 3362-3367.
- [3.13] Ogletree, D.F., R.W. Carpick, and M. Salmeron, *Calibration of frictional forces in atomic force microscopy*. Review of Scientific Instruments, 1996. **67**(9): p. 3298-3306.

4. FRACTURE EXPERIMENTS IN AIR

This chapter presents an introduction into the mechanical breaking of nanoobjects using SFM techniques and the calibration techniques needed to set-up mechanical test modi with which quantitative data on fracture strength can be obtained. The objects used as reference are nanopillars in SiO₂/Si made by standard lithography in the range below 1 μm. The fracture experiments are performed in air by lateral force of a modified SFM tip used.

4.1. Introduction

Mechanical properties are determined by the structural conditions on an atomic length scale. This includes defects such as grain boundaries, inclusions, dislocations and others [4.1]. Because of this, it should be highly interesting to perform mechanical experiments on objects as small as possible. The probability to encounter defects gradually decreases as a consequence of the defect density which remains constant. Nanostructures in various sizes and with various inherent features are producible by lithographic patterning techniques. Therefore, it should be possible to integrate artificial and well-defined defects into nanoobjects. These defects then will most likely dominate the mechanical properties. In the here shown experiments, the determination of the mechanical properties of nanostructures, altered by the presence of artificial defects, is realized with scanning force microscopy (SFM). The SFM is not only a highly sensitive microscope, it is also usable for various kinds of manipulations. Known are manipulations where nanoparticles [4.2, 4.3], single molecules [4] or even atoms [4.5] were moved on plain surfaces. In addition, carbon nanotubes have been bent in a well-defined way [4.6], indentation experiments [4.7], scratch tests [4.8], as well as friction tests [4.9] have also been carried out. In 2001, the research group led by Thomas Jung at Paul Scherrer Institute (Switzerland) has pioneered fracture experiments on nanostructures, so-called nanopillars which sometimes are also referred to as nanotowers [4.10, 4.11]. In the present chapter, this work is continued and further expanded regarding smaller structures and a better/faster fracture technique.

4.2. Nanopillar production

The nanopillar production is carried out by lithography and thin film techniques. Si(100) wafers were used as substrate material on which the top part was converted ($d_{\text{SiO}_2} =$

190 nm) into silicon-dioxide (SiO_2). The conversion occurs through an oxygen atmosphere in a low pressure chemical vapor deposition (LPCVD) apparatus. The resultant SiO_2/Si interface has an amorphous appearance and marks a well-defined grain boundary. Because of numerous defects [4.12-4.15] and the oxygen deficit at the interface [4.16], the junction between these two materials is mechanically weakened. As a consequence, the SiO_2/Si interface acts as a predetermined breaking point. A polymethyl methacrylate (PMMA) layer is deposited on the as prepared wafers by spin-coating (Fig.4.1). In a direct write process, nanopillar copies are generated by a focused electron beam (EBL). The PMMA thin film acts as a positive photoresist, i.e. the parts which are exposed to the electron beam were converted by absorbing energy (chain scission). The remaining polymer fragments are dissolved using a polar solvent mixture (1:1 mixture of isopropyl alcohol (IPA) and methyl-isobutyl-ketone (MIBK)).

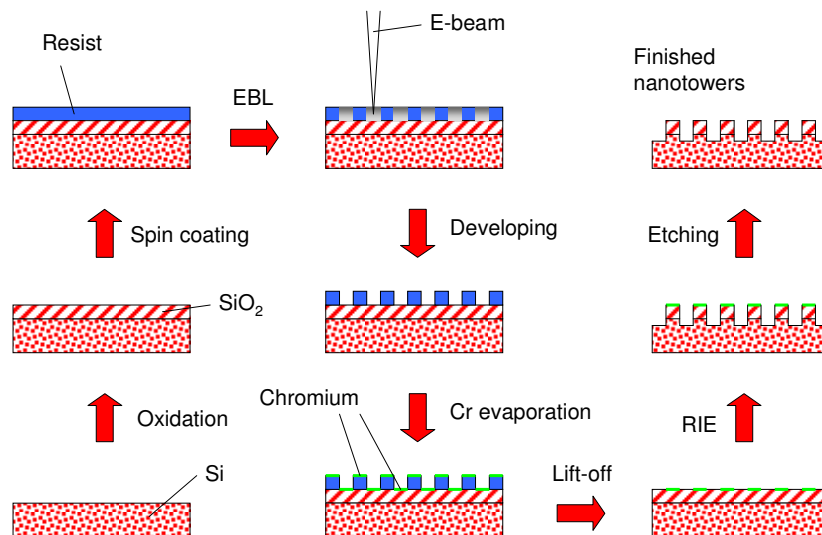


Fig.4.1: Schematic process of the nanopillar production: The surface of a Si(100) wafer is partially converted to SiO_2 by a LPCVD process. Fields of nanopillars with different diameters will be copied by means of PMMA photoresist and electron beam lithography. After development, chromium is evaporated onto the surface and a lift-off is carried out. Finally, the material is etched by RIE and the protective chromium layer is removed with an acidic solution of cerium nitrate.

In a further step, chromium is evaporated in order to form a chemical resistant layer (hard mask) for the subsequent reactive ion etching (RIE). The lift-off process takes place in an acetone or dichloromethane bath. Finally, the substrate is etched (O_2/CHF_3 1:1 mixture (100 mTorr) in a 100 W RF plasma) to a depth of 250 nm (in SiO_2 the etch rate is approximately 100 nm/min), i.e. 60 nm deeper as the position of the SiO_2/Si interface. The remaining chromium can be removed with a mixture of perchloric acid (HClO_4) and ammonium cerium

nitrate ($(\text{NH}_4)_2[\text{Ce}_2(\text{NO}_3)_6]$) in water. The so prepared Si wafer is then sawn into $10 \text{ mm} \times 10 \text{ mm}$ large pieces and glued onto nickel plates as a support for better handling. Fig.4.2 shows a schematic overview of such a chip:

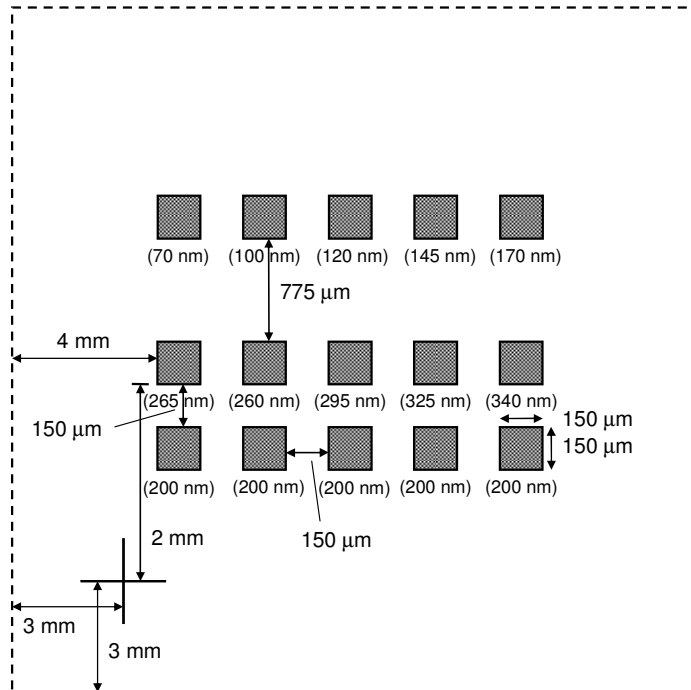


Fig.4.2: Schematic illustration of the quadratic pillar arrays which are located on a $10 \text{ mm} \times 10 \text{ mm}$ sample chip. A single array has an edge length of $150 \mu\text{m}$ while the pillars have a periodicity of $1 \mu\text{m}$. Therefore, 22500 pillars in total are arranged in such a gray labeled box. The cross at the left bottom of the diagram serves as an orientation mark and allows a faster localization of the pillar structures. The numbers in parentheses below an array box indicate the nanopillar diameter.

The so prepared nanopillars have a periodicity of $1 \mu\text{m}$ (Fig.4.3). At the bottom of the chip surface, which should consist of pure Si, granular deposits are visible. These deposits consist of native SiO_2 („ SiO_2 grass“). Based on the slightly different radiation dosage per volume element as a function of the photoresist depth, the pillars have a slightly conical shape (areas close to the surface receive a higher radiation dose).

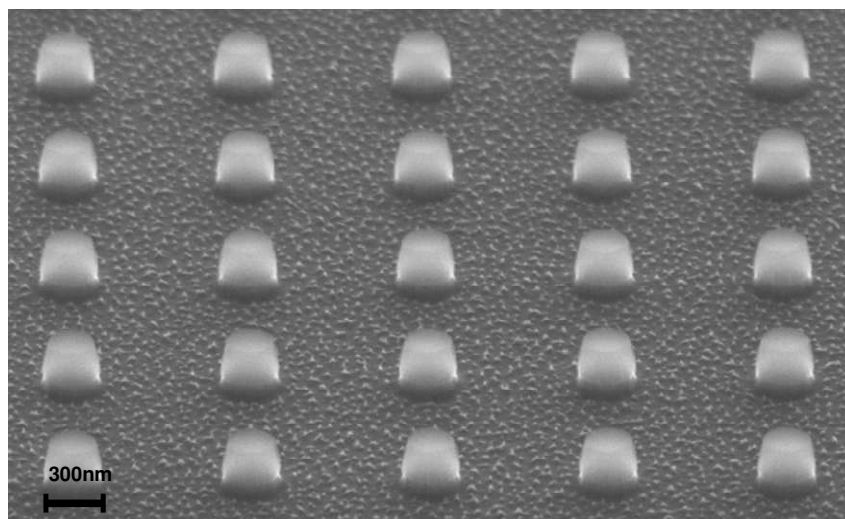


Fig.4.3: SEM micrograph of nanopillars with a diameter of 300 nm . The interface between the Si basis and the SiO_2 top is clearly visible. Since the sample was not coated with gold, the SiO_2 parts are blurred (charge effect). On the bottom of the sample chip, the so-called SiO_2 grass is visible.

4.3. Fracture mechanics using SFM

4.3.1. Conditions

All shown experiments were carried out with a ‚Dimension 3100‘ SFM from Veeco Inc. [4.17] (Note: Veeco was taken over by Bruker at the end of 2010). The ‚Dimension 3100‘ is operated in an air-conditioned room and is situated on an actively damped table to minimize distracting vibrations. The measurement principle of this instrument is based on the method of a reflected laser beam that is detected within a four-quadrant photocell. Furthermore, the ‚Dimension 3100‘ can be used for measurements in contact as well as in tapping mode. The SFM controller (A/D resp. D/A converter and processing unit) can simultaneously record three channels (e.g. height, error and friction signal), which, for recording purposes, are forwarded to a microcomputer. Mechanical experiments on nanostructures must be performed in the contact mode. Here, it is important that the used probe, while scanning, is not affected to changes concerning shape and surface texture. Based on this, the probe needs a hard and persistent coating such as Si_3N_4 or DLC. Tab.4.1 compares the SiO_2 hardness with the hardnesses of Si_3N_4 and DLC:

Material:	SiO_2 [4.18]	Si_3N_4 [4.19]	DLC [4.20]
Vickers hardness [kg/mm^2]	500	700... 1650	2000... 9000

Tab.4.1: Vickers hardness for the pillar material (SiO_2) and substances used for cantilever coatings i.e. for Si_3N_4 and DLC.

First experiments with Si_3N_4 coated cantilevers have shown that the cantilever tip erodes very quickly (see Fig.4.4). These experiments indicate that Si_3N_4 , although harder than SiO_2 , is not an appropriate material for fracture experiments. For this reason, all here mentioned experiments were performed with DLC coated tips.

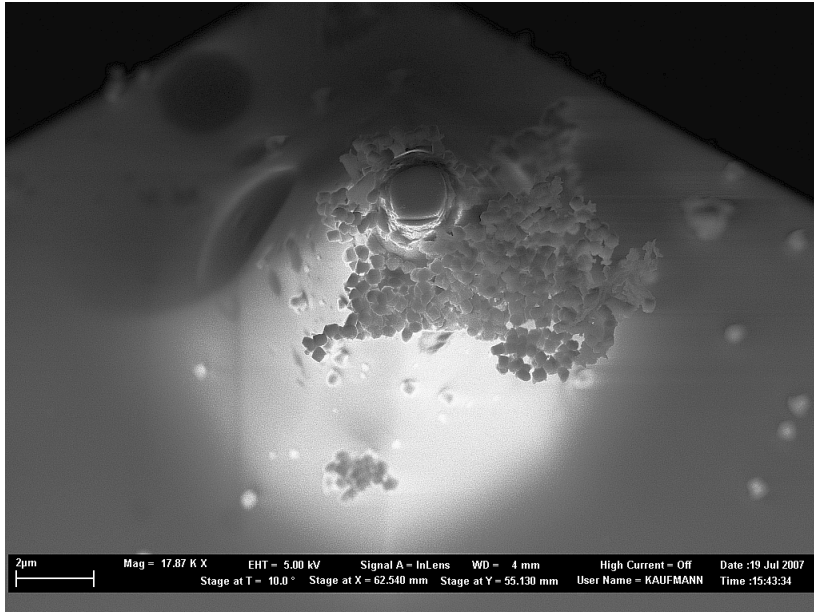


Fig.4.4: SEM micrograph of a Si₃N₄ cantilever tip. The flattened tip, which has been eroded by friction forces (the formed plateau has a diameter of about 1 μm), is clearly visible. At the top of the tip, the SiO₂ pillar remainders are sticking together in a grape-like fashion. Only DLC coated cantilevers can be used for fracture experiments due to outstanding hardness of DLC.

Fracture experiments with Si₃N₄ coated cantilever tips showed some interesting behavior: Experiments with new tips (CSC21 from MikroMasch [4.21]) caused that almost 100% of the pillars were broken even with minimal normal forces. After the tip was in use for a while and therefore a little bit eroded, the tip could be used for measurements. However, after a certain time the tip got too much eroded so that no pillars could be broken anymore, even with increased normal forces. This shows that the tip radius is of high importance. The same phenomenon was noticed with DLC coated cantilevers (DT-FMR cantilevers from NanoSensors, see Tab.4.2 for more information [4.22]): New cantilevers have the ability to break every pillar during a measurement even with low normal forces.

Technical Data:	Nominal Value:	Common interval:
Thickness t (in μm):	3	2.0 – 4.0
Tip height h (in μm): (the tip height is the distance from the middle of the cantilever to the tip end)	13	10 - 15
Width w (in μm):	28	20 - 35
Length L (in μm):	225	215 - 235
Spring constant k_N (in Nm ⁻¹):	2.8	0.5 – 9.5
Resonance frequency f_0 (in kHz):	75	45 - 115

Tab.4.2: Technical information concerning the cantilevers used in experiments described

herein. The cantilevers with the description DT-FMR originate from the company NanoSensors and are coated with an approximately 100 nm thick DLC layer as protection against abrasive friction forces. The macroscopic tip radius is specified with 100 to 200 nm. However, the DLC coating is rough and therefore a nanoscopic tip radius of 10 nm is achievable.

As the DLC coating is extremely robust, the coating remains perfectly intact even after several hours of measurements and therefore also the characteristic tip behavior stays unchanged, i.e. all pillars will be broken off independent of the applied normal force. Hence, the tip radius had to be increased artificially by the use of a focused ion beam (FIB) instrument and also to smooth the nano-roughness of the coating. For this purpose, some tip coating was removed from the free end and from the sidewalls. The modified DLC tips showed a tip radius of about 200 nm and could then be used for the aimed fracture experiments. With appropriate caution, so prepared tips can be used without difficulty for half a year or even longer (Fig.4.5).

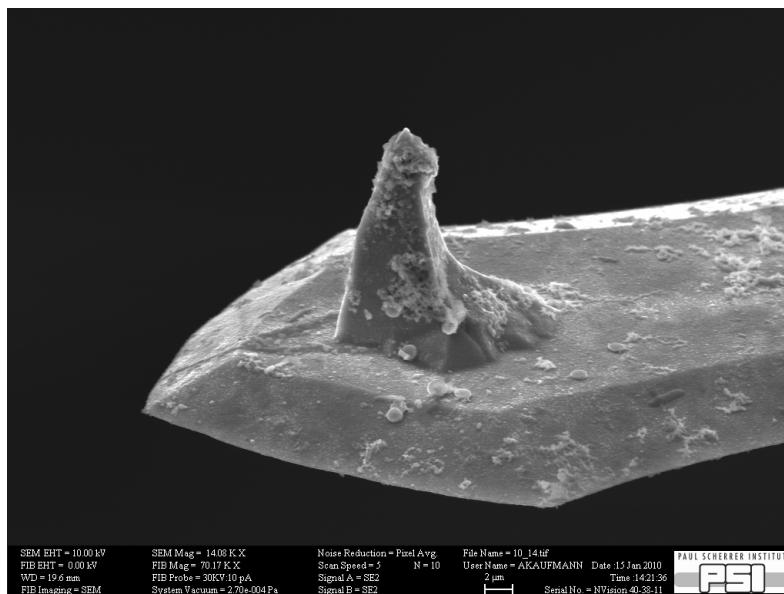


Fig.4.5: SEM micrograph of a modified DLC tip. Some tip material was removed with the FIB to increase the tip radius. Furthermore, also the nano-roughness of the DLC coating was decreased that way. The FIB directs a focused ion beam of gallium ions onto the relevant places whereby material is ejected. The here shown tip was already in use that is why debris is attached to the tip.

4.3.2. Interactions between tip and pillar

It is of interest to know how the tip comes in contact with the pillar and how the forces begin to act. Here, only the tip movement, while pushing to the center of the pillar, is considered (Fig.4.6). When the tip is approaching a pillar, mainly two forces come into play: The normal force F_N , which is adjusted via setpoint and secondly, the lateral force F_L which acts opposite to the scan direction. In the contact mode, the cantilever is guided over the sample surface with a 90° angle with regard to the scan direction. The normal force F_N leads

to a bending of the entire cantilever, while the lateral force F_L leads to a cantilever twist. The lateral force occurs due to sliding friction between tip and substrate. When a cantilever tip approaches a pillar, the tip touches the pillar at point A for the first time (1). Further movement results in a twisted cantilever (2) and therefore a lateral force begins to act. Because of the retarded response of the feedback, mainly based on the integral control parameter, the lateral force achieves its maximum here. Moreover, the tip is also lifted up a little bit from the base level due to the twisting in (2). In function of the control parameters, i.e. in function of the proportional as well as the integral parameter, the tip is moved alongside z (3) to regain a height which fulfills the previously adjusted setpoint.

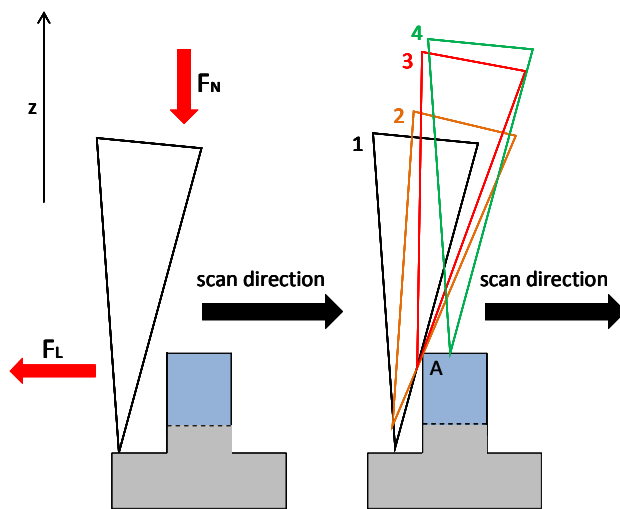


Fig.4.6: Schematic overview of the movement of the cantilever tip at the scanning of a pillar. In position 1, the tip gets in first contact with the pillar. The mechanical resistance leads to a twisting of the tip whereby a lateral shear force can be developed (2). Defined by the adjusted parameters, the tip starts to lift up after a small time delay to achieve the preset set point (3). Here, a tension occurs based on the friction in point A. After a while, the cantilever is on the plateau of the pillar. The twisting takes a constant value (4) given by the sliding friction between the tip and the pillar material (SiO_2).

Additionally to the lateral force, also a new force component begins to act: Because of the friction between tip and pillar in point A, based on the upward movement of the tip, the pillar experiences a force in vertical direction (tensile stress). That means that, in addition to the crack opening mode II (see chapter 2), which describes a shear strain, also mode I is involved which describes a crack opening under a tensile load. This shows that several crack opening modes are responsible for pillar fracturing. After a certain time, given by the scan speed, the pillar plateau is reached (4) and the tip is on the flat surface, i.e. no changes regarding z -position must be done. Depending on the control parameters, the tip needs to settle itself a little. With unfavorable control parameters, a periodic oscillation can appear. Since scanning does not start in the middle of a pillar, the tip behavior is not identical for each contact point. When the tip hits the pillar off-center, the cantilever will not only experience twisting (torsion), additionally the cantilever will also be bent in lateral direction. For this, the two lateral forces are lying orthogonal to each other while acting against the pillar.



Fig.4.7: Schematic image for the illustration of the lateral and torsional twisting of the cantilever tip when the pillar is not hit centrally. The cantilever gets twisted by the mechanical resistance of the pillar but also experience a lateral bending.

This new situation produces a torsional moment which could initiate a crack opening according to mode III (Fig.4.7). All in all, it has to be mentioned that here all three crack opening modes are involved and that therefore the pillar fracture process is of multiaxial nature.

4.4. Statistical fracture experiments

The here shown experiments were carried out in air: The statistical behavior was evaluated in function of the preset measuring parameters. In a first and mandatory required step, prior to the actual experiments, the fracture behavior of the FIB prepared tips has to be identified. The pillars must break exactly at the position of the interface, i.e. 60 nm above the base level. As shown in Fig.4.8, a pillar can be broken off in different ways.

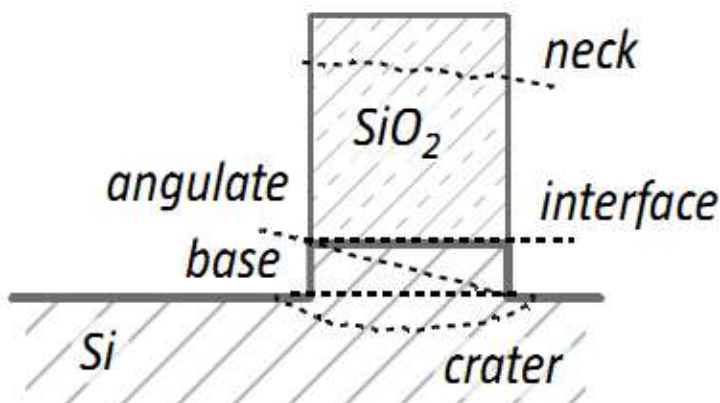


Fig.4.8: Schematic drawing of the possible and also observed fracture types of a nanopillar. It could be shown that the type of fracture is strongly related to the condition of the tip. The tip radius and the roughness of the tip seem to be the relevant parameters. Blunt tips can no more be used to break off pillars, while new tips break off pillars at different heights. For stump tips only a slow erosion of the pillar height was observable.

The different fracture types were not systemically studied but they show the potential difficulty in fracture experiments related to nanopillars. However, this behavior is noteworthy because if one doesn't pay enough attention to it, it can be a source of errors. Of course, the here shown experiments were carried out with cantilevers able to fracture in a controlled way at the position of the interface.

For each realized experiment, the scanned quadratic area had an edge length of 10 μm . With a pillar periodicity of 1 μm this results in a total of 100 pillars per scanned area. Such an area was processed with 512 scan lines with 512 data points per scanned line. By this, one scan point is recorded every 20 nm. Therefore, a single nanopillar with a diameter of 300 nm experiences about 15 line scans which results in about 175 data points per scanned pillar. In the breaking experiment, however, every single scan can lead to fracture, and depending on the location of the mechanical contact, different lateral forces apply. The shown experiments were carried out with parameters listed in Tab.4.3.

Scan size (in μm):	10	Aspect ratio:	1:1
Scan angle:	90°	Scan rate (in Hz):	1.0
Tip velocity (in $\mu\text{m/s}$)	20.0	Data points/line:	512
Lines:	512	SPM feedback:	Deflection
P-Gain:	2.0	I-Gain:	3.0

Tab.4.3: Scan parameters as used for statistical fracture experiments in air. The amount of broken pillars per full scan was evaluated in function of the exerted normal force F_N .

A scan always starts in the middle of a pillar array area. Since the statistical investigation refers to the entire area, the scan position was changed to the top right after the start of a measurement. After a scan, with a preset normal force (modification mode), the normal force was decreased in such a way, that no pillar breaking will further occur to count the amount of broken nanopillars (detection mode). The percentage of broken nanopillars, depending on the number of scan pairs, was then evaluated. This process has been further improved in the course of the liquid experiments (see chapter 5), for which no detection mode is needed anymore. This allows a higher throughput of experiments. The statistical

experiments were performed on pillars with diameters of 120 nm, 145 nm, 170 nm and 200 nm (Fig.4.9).

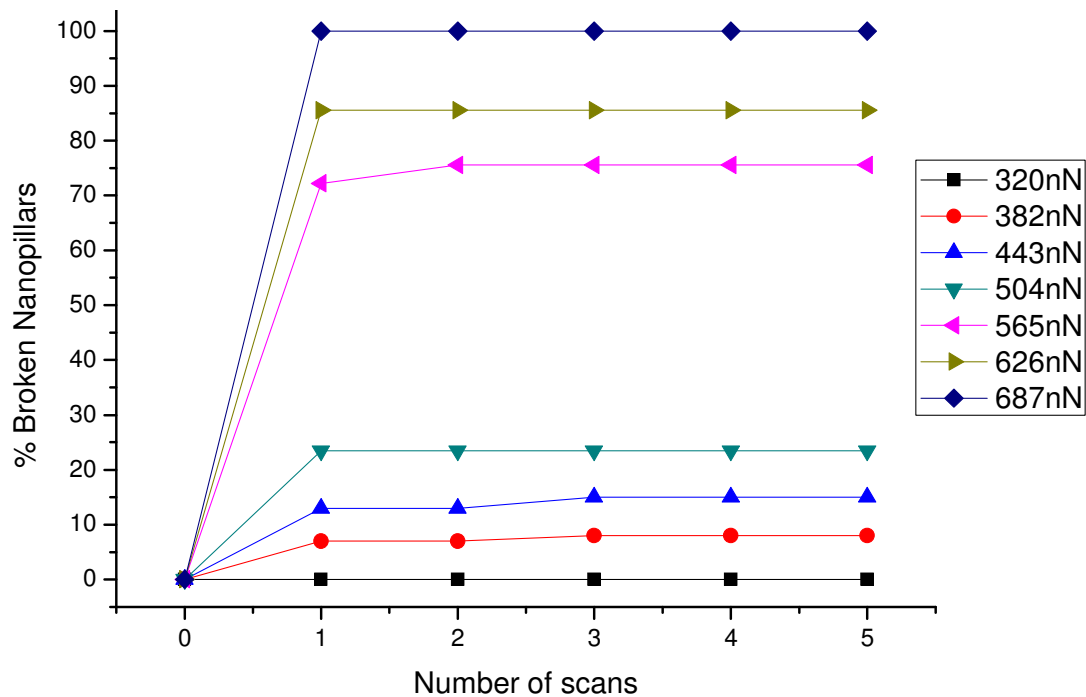


Fig.4.9: Percentage of broken pillars (200 nm \varnothing) in function of a scan pair. A scan pair consists of a scan with an increased normal force (modification mode) and a scan with a low normal force, where no pillars will fracture in order to count the number of broken pillars (detection mode). In the graph above, two main findings are shown: (1) No significant signs of fatigue are detectable and (2) the graphs are divided into two bands. The distance between these two bands is an indicator for the pillar uniformity and can therefore be regarded as a parameter for the overall manufacturing quality.

Two things are worth mentioning: After the first modification scan no significant changes occur and second, a splitting of the graphs in two bands is observable. The first observation means that no distinct fatigue is present. The second observation says something about the uniformity of the pillars. If the pillars would be 100% uniform, i.e. absolute identical to each other, only two graphs should be visible, one at 0% and the other at 100%. Therefore, the width of these two bands gives information about the quality of the pillars: The distributions of e.g. diameter, height, form, material appearance and interface indicate the width of these two bands shown in Fig.4.9. This method can, for a fixed normal force increment, be used to compare the integral quality of the used manufacturing steps. A plot of the experiments, after the fifth scan pair as function of the normal force F_N , results in curves that can be found at different forces (Fig.4.10). The curves show, except for the “170 nm”

curve, a sigmoid character. The position of the inflection point ($f''(x_w) = 0$ and $f'''(x_w) \neq 0$) seems to shift to 100% broken pillars with decreasing pillar diameters.

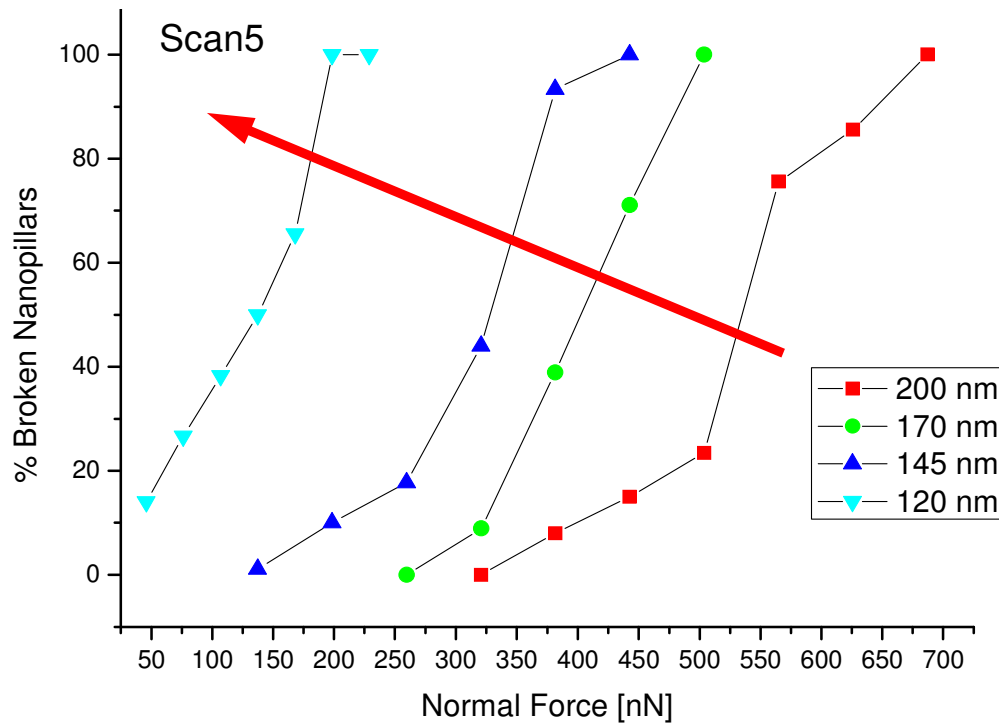


Fig.4.10: Fracture behavior of nanopillars with different diameters: Pillars with small diameters are shifted to the left, i.e. to smaller forces. At this, the sigmoidal character of the curves decreases. The drawn arrow shows the approximate position of the inflection point. The y-value of the inflection point increases with smaller pillars.

The inflection point indicates the location at which even a small force variation would induce a major change in the number of broken nanopillars. Hence, the inflection point can be seen as the force which would best characterize the probed pillars. Furthermore, it also approximately marks the center position of the band gap. In Fig.4.10, the shown arrow marks the shift of the band gap towards higher values within smaller pillar diameters. This means, according to 120 nm thick pillars, that thinner pillars possess no characteristic fracture force. This observation could maybe be attributed to an evolving size effect phenomenon.

4.5. Nanopillar - Lithography

Experiments on individual pillars were carried out, additionally to the statistical experiments shown before. Here, the goal is to modify individual pillars and to break them in a highly directed way. Such experiments were also performed in the contact mode but it turned out to be very difficult. The main problem is that the cantilever tip first must come

close to the selected pillar at low normal forces. After that, the scan area needs to be minimized in such a way that only the selected pillar is visible. Then the normal force can be increased to an adequate level with which the pillar can be broken. But here, the cantilever is bent whereby it happens that the cantilever scans all over the selected pillar. This phenomenon as well as the creeping of the piezo, favored by the approach process and the normal force changes, leads to a large lateral uncertainty and to a general tip instability.

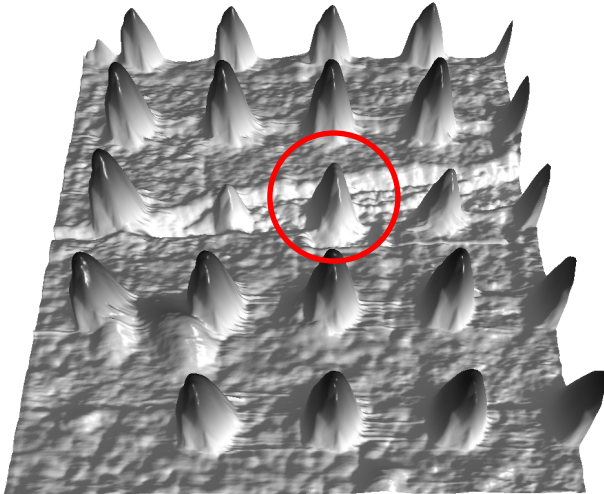


Fig.4.10: SFM topography image of a contact mode fracture experiment on a single nanopillar. The goal of this experiment was to break the marked pillar. But instead of breaking the intended pillar, the pillar on the left was broken and the pillar on the right was eroded. This instable behavior can be attributed to the bending of the cantilever when the force is increased as well as to creeping of the piezo actuator.

Fig.4.10 shows an attempt to break a single pillar in contact mode. Here, the result was disappointing: Instead of breaking the encircled pillar, the pillar on the left was broken and the pillar on the right was eroded. After several unsuccessful attempts, we switched to the so-called tapping mode. The tapping mode is often regarded as a non-contact mode but this is not the case. In the tapping mode, the cantilever is periodically excited by the piezo to induce oscillations. As a variable, often the RMS signal of the amplitude is used. This is also the case for the here shown experiments. The RMS amplitude is measured in volts whereas a small value corresponds to an increased normal force. The oscillating cantilever is then guided over the sample surface. For a short time, the cantilever, at maximum negative amplitude, gets in close contact with the sample surface. During that time, the tip can interact with the pillar and possibly break it as long as a sufficiently high force is exerted.

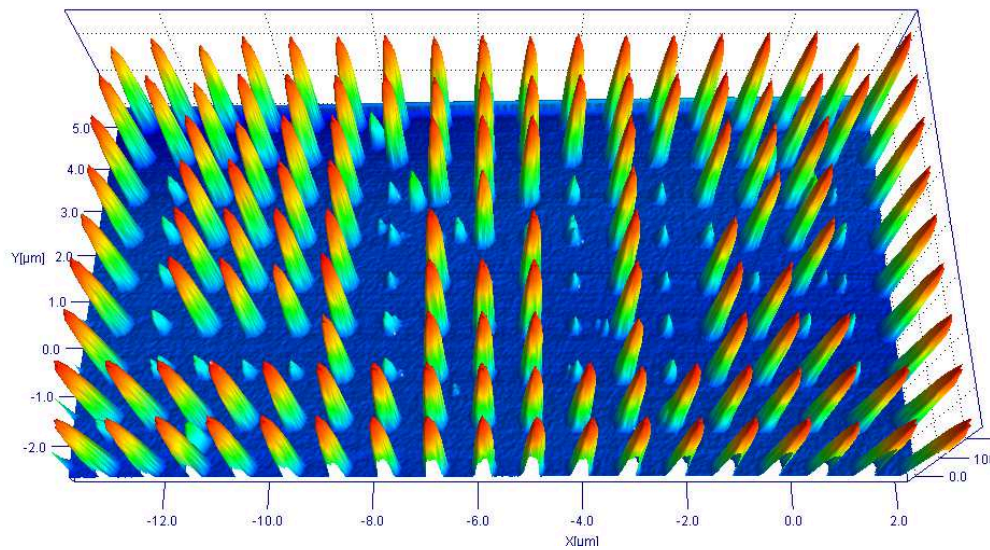


Fig.4.11: “LMN” writing that was written in an array of nanopillars. LMN stands for Laboratory for Micro- and Nanotechnology, located at the Paul Scherrer Institute in Würenlingen (Switzerland). This writing was created within half a day using a modified tapping mode technique. Furthermore, this technique can be used for 2D data storage applications.

The big advantages of the tapping mode are the less strong piezo creep as well as the diminished cantilever bending. With the right technique, a pattern such as “LMN” (Fig.4.11) can manually be written within half a day. To increase the writing speed and to increase positioning accuracy after a pillar was broken, the field of view was not increased to the initial state but kept constant, going on with the given scan area (about $1 \mu\text{m}$). The used method is described in detail as follows:

- 1.) The scan area is reduced in such a way that only one pillar is visible in the middle of the scan area (approximately $1 \mu\text{m}$). It will be scanned until the piezo creep has fully disappeared.
- 2.) The scanning rate is increased to 5 Hz, which corresponds to a tip velocity of about $5 \mu\text{m/s}$.
- 3.) When the scan line reaches the pillar center, the slow-scan-axis (y-direction) is turned off. For the shortest possible time interval (less than a second) the preset setpoint is decreased to 0.1 V RMS amplitude and then switched back to the initial value.
- 4.) The lateral position is moved by the piezo actuator in such a way that the next pillar gets centered.

5.) The process is completed and can now again be started from point 1.

With this technique, written fields can be used as a data storage, i.e. a so-called WORM (Write Once Read Many times) device. Furthermore, one can think of using this technique to produce stamps for nanoimprint lithography [4.23]. This process is usable for e.g. prototype stamps where the production of a real stamp would be too expensive.

4.6. *Summary/Discussion*

The SFM has proven as a powerful tool for investigations concerning fracture phenomena related to the nanoscale. In contrast to traditional fracture experiments, such as tensile tests, the SFM can examine fracture characteristics on the basis of atomic conditions. For macroscopic bodies, the integral behavior is usually probed. This means that instead of the material, the sum of the defects lying in the probed body are examined. Individual defects, such as a single grain boundary, can be integrated into nanostructures by lithographic techniques. This advantage, coupled with the sensitivity of a SFM, allows the determination of the influence of single defects on the behavior of a body. Defects play an important role for the mechanical stability which can be of crucial importance for MEMS/NEMS devices. It was shown that statistical experiments allow conclusions about the quality of the used production processes. Furthermore, the selective breaking of nanopillars can be used to store information permanently. Magnetic storage devices for example have the disadvantage that the magnetic domains align to the terrestrial magnetic field lines over time. Optical encoded media, such as DVDs, are written in a polymer material (polycarbonate) and therefore also have a limited durability caused by embrittlement. Pillars of SiO₂ and Si seem to be robust and can be read-out countless times in the tapping mode which would make them a favorable choice for long-time data storage devices.

4.7. References

- [4.1] Mielke, S.L., T. Belytschko, and G.C. Schatz, *Nanoscale Fracture Mechanics*. Annual Review of Physical Chemistry, 2007. **58**: p. 185-209.
- [4.2] Hansen, L.T., et al., *A technique for positioning nanoparticles using an atomic force microscope*. Nanotechnology, 1998. **9**(4): p. 337-342.
- [4.3] Junno, T., et al., *Controlled manipulation of nanoparticles with an atomic force microscope*. Applied Physics Letters, 1995. **66**(26): p. 3627-3629.
- [4.4] Jung, T.A., et al., *Controlled Room-Temperature Positioning of Individual Molecules: Molecular Flexure and Motion*. Science, 1996. **271**(5246): p. 181-184.
- [4.5] Eigler, D.M. and E.K. Schweizer, *Positioning single atoms with a scanning tunneling microscope*. Nature, 1990. **344**(6266): p. 524-526.
- [4.6] Avouris, P., et al., *Carbon nanotubes: nanomechanics, manipulation, and electronic devices*. Applied Surface Science, 1999. **141**(3-4): p. 201-209.
- [4.7] Bhushan, B. and V.N. Koinkar, *Nanoindentation hardness measurements using atomic force microscopy*. Applied Physics Letters, 1994. **64**(13): p. 1653-1655.
- [4.8] Jung, T.A., et al., *The atomic force microscope used as a powerful tool for machining surfaces*. Ultramicroscopy, 1992. **42**: p. 1446-1451.
- [4.9] Meyer, E., et al., *Friction and Wear of Langmuir-Blodgett Films Observed by Friction Force Microscopy*. Physical Review Letters, 1992. **69**(12): p. 1777-1780.
- [4.10] Baumeister, B., T.A. Jung, and E. Meyer, *Nanoscale fracture studies using the scanning force microscope*. Applied Physics Letters, 2001. **78**(17): p. 2485-2487.
- [4.11] Baumeister, B., T.A. Jung, and E. Meyer, *Tribological studies on fracture and erosion of nanostructures*. Tribology Letters, 2001. **11**(2): p. 107-110.
- [4.12] Helms, C.R. and E.H. Poindexter, *The silicon-silicon-dioxide system: its microstructure and imperfections*. Reports on Progress in Physics, 1994. **57**(8): p. 791-852.
- [4.13] Himpsel, F.J., et al., *Microscopic structure of the SiO₂/Si interface*. Physical Review B, 1988. **38**(9): p. 6084-6096.
- [4.14] McKee, R.A., F.J. Walker, and M.F. Chisholm, *Crystalline Oxides on Silicon: The First Five Monolayers*. Physical Review Letters, 1998. **81**(14): p. 3014-3017.
- [4.15] Williams, R., *Properties of silicon-SiO₂ interface*. Journal of Vacuum Science & Technology, 1977. **14**(5): p. 1106-1101.
- [4.16] Carniato, S., G. Boureau, and J.H. Harding, *Modelling oxygen vacancies at the Si(100)-SiO₂ interface*. Philosophical Magazine a-Physics of Condensed Matter Structure Defects and Mechanical Properties, 1997. **75**(5): p. 1435-1445.
- [4.17] *Scanning Probe Microscopy (SPM) Service Lab*. [cited 2011, 3.2.]; Available from: <http://lmn.web.psi.ch/molnano/spm/index.html>.
- [4.18] Groover, M.P., *Fundamentals of modern manufacturing : materials, processes, and systems* 2010, Hoboken, NJ: J. Wiley & Sons.

- [4.19] Shukla, P.P. and J. Lawrence, *Fracture Toughness Modifications By Means of CO₂ Laser Beam Surface Processing of a Silicon Nitride Engineering Ceramic*, in *Proceedings of the 36th International MATADOR Conference*, S. Hinduja and L. Li, Editors. 2010, Springer London. p. 519-522.
- [4.20] Pierson, H.O., *Handbook of carbon, graphite, diamond and fullerenes : properties, processing and applications* 1993, Park Ridge, New Jersey: Noyes Publications.
- [4.21] MikroMasch. *CSC21/Si₃N₄*. [cited 2011, 3.2.]; Available from: <http://www.spmtips.com/csc/c21/si3n4>.
- [4.22] Nanosensors. *DT-FMR*. [cited 2011, 3.2.]; Available from: <http://www.nanosensors.com/DT-FMR.htm>.
- [4.23] Schiff, H., *Nanoimprint lithography: An old story in modern times? A review*. *Journal of Vacuum Science & Technology B*, 2008. **26**(2): p. 458-480.

5. FRACTURE MECHANICS IN A CORROSIVE ENVIRONMENT

In this chapter, fracture experiments are performed in a liquid environment. In contrast to those in air, SFM experiments in liquid eliminate the effect of a water meniscus formed from humidity in air. Furthermore, liquids can be exchanged, contain chemical reactants and the influence of corrosive media can be studied. The main disadvantages are an increased complexity of the experimental setup, time dependent contamination of the samples and their surface and permanent modification of their properties. Samples once exposed to liquid can therefore not be considered as original and untouched as those stored in air.

5.1. Introduction

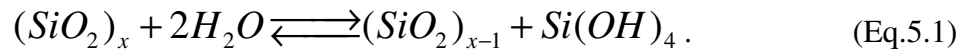
Fracture processes are mainly determined by the conditions on an atomic length scale. Therefore, chemical and/or physical processes, which are able to affect these conditions, can influence the mechanical behavior of a material. In this chapter, the influence of a liquid (water) as well as a corrosive agent (NaCl), on the fracture behavior of SiO₂/Si nanopillars, is studied. In the case of the experiments in NaCl solution, the chronological behavior as well as the concentration dependency is of central importance. In contrast to macroscopic bodies, nanopillars have an increased surface-to-volume ratio, or more precisely surface-to-bulk ratio, since also part of the volume atoms are contributing to the surface properties in contrast to the bulk. Due to this fact, it should be possible to determine to what extent the surface may dominate the overall behavior of such nanopillars. Therefore, a kind of competition between the volume and the surface respectively between adsorption and diffusion processes should become observable. This behavior is proven valid as can be shown within the results in this chapter.

5.2. Theory

5.2.1. Influence of water

According to Griffith's fracture theory [5.1], a fracture process is initiated through microscopic defects, e.g. so-called microcracks. These microcracks are occurring occasionally and exhibit a dynamic behavior which means, that they can be generated by tensions but that

they also get closed from themselves if the acting forces disappear and their length is under critical size (see Fig.2.6). Polar chemicals, as for instance water, are able to stabilize microcracks and therefore increase their lifetime. Therefore, a crack has more time for propagation. The stabilization of a crack occurs, among other effects, due to steric hindrance of the crack closing process. The displacement of the chemical species from the gap would consume energy which explains why it is unfavorable for the system. The crack stabilization in dipolar substances, such as water, can also take place due to the fact that the ionic broken Si-O-Si bonds are stabilized by van-der-Waals forces as well as hydrogen bonds. Furthermore, water itself is able, in form of a chemical reaction [5.2], to interact with SiO₂. SiO₂ is the acid anhydride of the *ortho*-silicic acid (H₄SiO₄ ≡ Si(OH)₄). Water can dissolve SiO₂ according to the following principle:



Acids in general, as well as bases, react in a similar manner, the latter posses a higher dissolution rate for SiO₂. Performed experiments showed that with increasing humidity, the energy needed for the opening of a crack, is reduced [5.3]. This phenomenon is based on the same chemical reaction as shown in Eq.5.1 while mechanical stress renders the bond parameters sub-optimal and thereby decreases the activation energy. This energy decrease facilitates the crack growth [5.4]. In addition, experiments related to SiO₂ showed that chemical species, which present electron as well as proton donor properties (e.g. water), are the main reason for stress corrosion phenomena [5.5]. For chemically inert electrolytes, such as sodium chloride (NaCl), additional mechanisms are involved. As shown in [5.6], the ionic strength has a prominent influence on the corrosion behavior of glass fibers. According to [5.7], alkali metals become chemically reduced by the SiO₂/Si interface, whereby positive charges are transmitted to the interface region. A general accumulation of alkali metal ions at the interface was observed in [5.8]. This effect is explainable by the low interface packing density. As a result, the diffusion rate at the interface is increased which may explain the ion accumulation at that position. The formation of an electric dipole between the silicon and the SiO₂ was shown in [5.9]. The formation of such an electric dipole would lead to a stabilized interface.

5.2.2. Interactions between electrolytes in general and in particular of sodium ions with charged surfaces

The accumulation of sodium ions on SiO_2 surfaces was shown in [5.10]. It was found that sodium ions can diffuse several 100 nm deep into the bulk material. In case of a nanopillar, this would mean that along the entire pillar cross-section sodium is accumulated. The SiO_2 surface consists of hydroxyl groups originating from the partially condensed *ortho*-silicic acid. The acidic nature of these groups leads to deprotonation and therefore to a negatively charged surface. If cations are present in solution, these then would accumulate on top of the surface to compensate the negative charge. A so-called electrical double layer (EDL) is formed [5.11]. A layer of strongly bound ions is generated directly on the surface. This layer is called Helmholtz double layer which can be divided into two zones: The inner Helmholtz layer (IHL), also called Stern layer, and the outer Helmholtz layer (OHL).

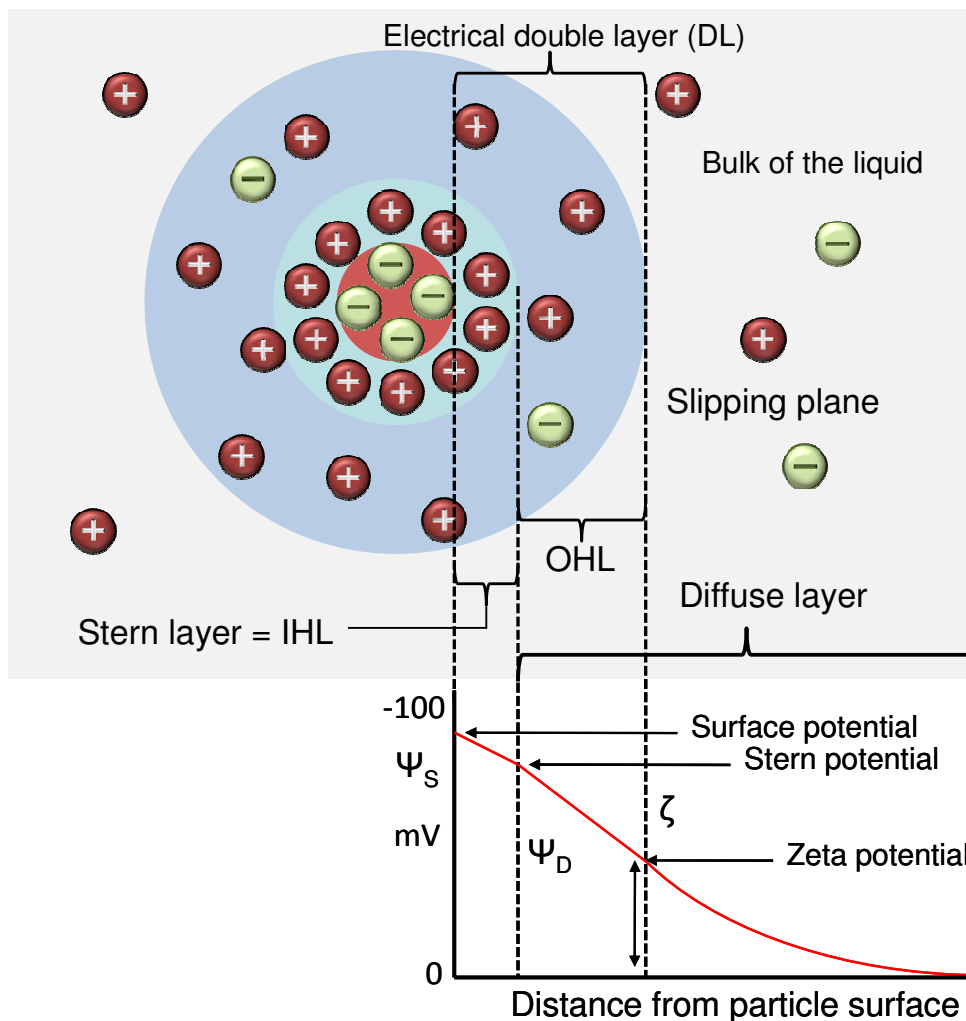


Fig.5.1: Schematic illustration of a negatively charged particle in a liquid medium that contains electrolyte. The negative surface charge of the particle is compensated with positively charged ions (cations). The particle appears electrical neutral seen from outside respectively from an infinite distance. Different characteristic zones form around the particle: The layer that is in direct contact with the particle is called inner Helmholtz layer. In this layer the cations obey only limited transitional freedom. The next layer is the outer Helmholtz layer. In this segment, the ions have a diffuse mobility while still being bound to the surface. The outer border of this layer is called slipping plane and marks the position where the so-called zeta potential is measured.

The IHL marks the zone where the involved ions are so strongly bound that no or only minimal lateral ion movements are expected. In the OHL the ions are also strongly bound to the charged surface. However, the ions have an increased but still limited mobility. The boundary between the OHL and the medium is called slipping plane with the included zeta potential (ξ potential, see Fig.5.1). Outside of the ξ potential, ions accumulate rather loosely in a diffuse, uncorrelated manner. The surface appears electrically neutral from large distances because all surface charges are compensated by the ions associated to the surface. Frictional forces can shear off the loosely bound diffuse layer, whereby the surface appears no longer electrically neutral to the outside. This situation is immediately brought back to the original state after the frictional penetration stops acting. In aqueous NaCl solutions ($\text{pH} \cong 7$), the ξ potential of SiO_2 is approximately -20mV for 10^{-1} M , -45 mV for 10^{-2} M and -65 mV for 10^{-3} M NaCl solutions [5.12].

5.3. *Nanopillar experiments in liquids*

The here shown experiments were carried out with a SFM liquid cell. In this liquid cell (Veeco Direct Drive Fluid Cantilever Holder), the cantilever is completely surrounded by the liquid medium. The same cantilevers (DT-FMR of Nanosensors), as used in the experiments in air, were used. The scanning conditions were also the same and therefore have the same characteristic values as shown in Tab.4.3. In one of the first experiments, a sample chip, prior to the measurements, was stored in pure water (the specific resistance ρ of the used water was $\geq 18\text{ M}\Omega\cdot\text{cm}$) for several days for sample equilibration. It is important that only plastic containers are used to store sample chips because glass is known as a source of alkali metals. The conducted experiment, i.e. the data points scattering determination, provides information about the uncertainty of the measurements in liquids (Fig.5.2). In this series, 170 nm thick nanopillars were scanned with a constant normal force of 200 nN . The measurement was performed within two days. It shows that the measured values for broken nanopillars are

between 70% and 100%. The scatter of the fracture threshold forces for nanopillars immersed in water is higher than for the corresponding measurements in air. This can be explained by the fact that water affects the surface and/or the SiO₂/Si interface and actively interferes with the fracture process by itself (see chapter 1.1.1).

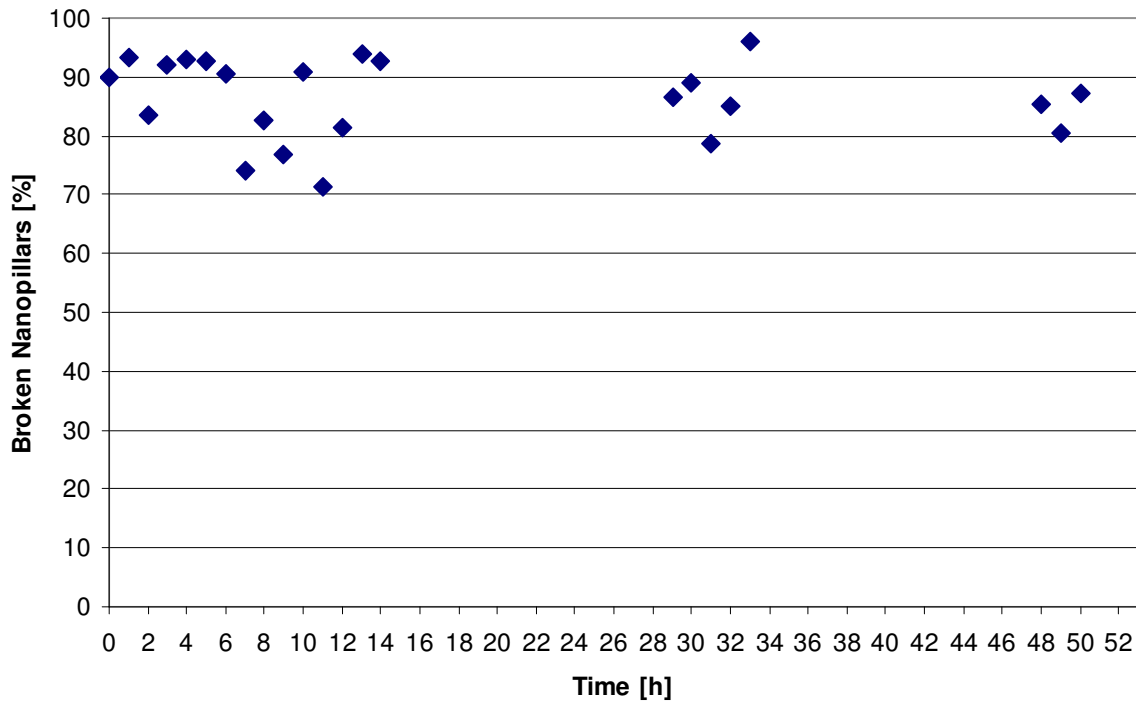


Fig.5.2: A field of 10 $\mu\text{m} \times 10 \mu\text{m}$ with 100 nanopillars inside was scanned in water. The 170 nm thick pillars were exposed to a normal force of 200 nN. The sample chip was equilibrated for several days in water. The graph shows scattered data points ranging from 70% to 100% for constant consitions.

Further, a sample chip, which was never exposed to water before, was immersed into water to study hydration. For this experiment, nanopillars with a diameter of 260 nm were used and a normal force of 1000 nN was applied. Here, a modified scan procedure was used: The measurement was only performed in the modification mode instead of the so far used scan pair, which consists of a modification and detection scan, because the amount of broken nanopillars is also identifiable during the modification scan (height image, Fig.5.3). In the shown image, the scan was directed from top to bottom at which a fraction of pillars was broken. At the beginning, the pillars were measured at their full height until they were broken. In the height image, instead of the intact pillar, now the associated socket gets visible. For the analysis of such measurements, only the pillars, which were intact as from the beginning,

were considered. As can be seen in Fig.5.3, four pillars out of 100 pillars were broken apart the measurement which means that 100% corresponds to a number of 96 pillars.

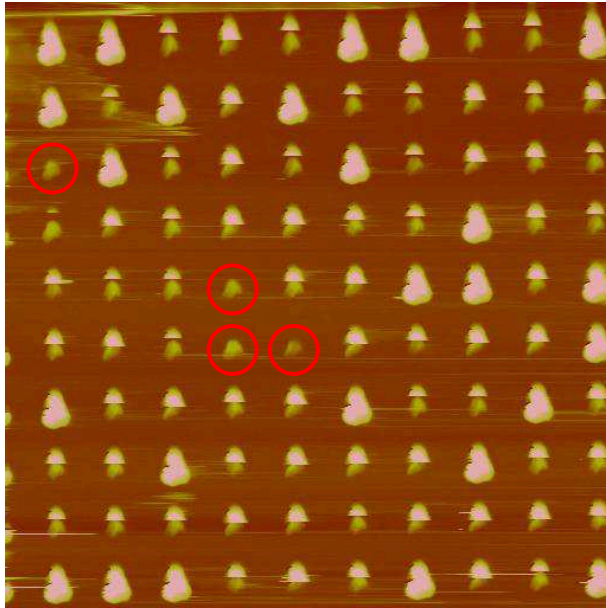


Fig.5.3: On the left a SFM topography image (height signal) is shown. The measurement was performed at an increased normal force F_N . Intact (bright and larger spots) but also broken pillars (smaller spots) are visible. At the beginning, the broken pillars were imaged at their full height. During scanning, some of the pillars were broken off at the interface, by what only the socket remains visible. Four pillars were already broken prior to the scan (encircled) and were therefore not used for the statistical analysis.

As can be seen from the experiments presented, water causes a weakening of the pillars (Fig.5.4a). At the beginning of the water exposure, the number of broken pillars was about 30% which then steadily increased to a value of approximately 80% within the next six hours, each value gained after one scan of a new area. This weakening, as described in the theory part, can be explained by stabilizing the microcracks that were created through the mechanical penetration. After this initial stage, the nanopillars showed a constant fracture behavior.

In the next shown experiments, the potential influence of aqueous electrolyte solutions regarding the fracture behavior of SiO_2/Si nanopillars is studied. As an electrolyte, NaCl was chosen because it has numerous advantages: NaCl is ubiquitous, nontoxic and consists of a single charged cation, the Na^+ ion, as well as a single charged anion, the Cl^- ion. Furthermore, NaCl possess a satisfactory solubility in water (360 g/L at 20°C) and in case of sodium, a small ion radius ($r(\text{Na}^+) = 102 \text{ pm}$) which should make diffusion processes easier.

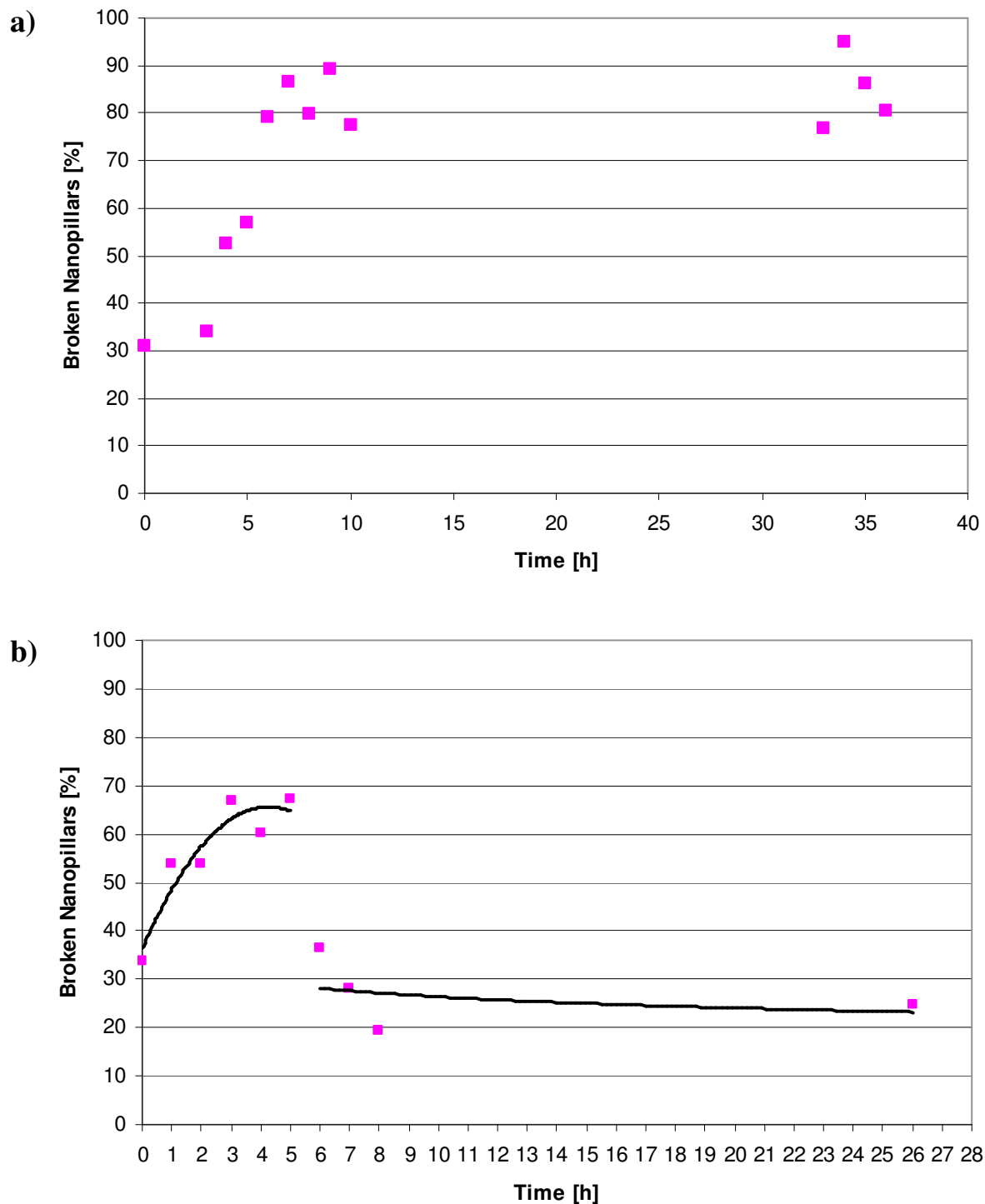


Fig.5.4 (a): Here, the hydration of the pillars is shown. The measured nanopillars are initially completely dry and are then submerged in water. Water causes a significant weakening. At the beginning, only 30% of the pillars broke at the given conditions. After approximately six hours, the pillars were weakened in such a way that 80% will break. **(b):** Here, the influence of NaCl is shown. First, the pillars were equilibrated in water before the solution was changed. At the beginning, a weakening of the pillars can be seen. After about six hours, the fracture behavior changes and the pillars get strengthened. This means that here at least two counteracting processes are involved (the black curves are guidelines for the eye and do not correspond to real values).

An unexpected phenomenon can be seen when a pillar array, which was well equilibrated in water, is stored in an aqueous NaCl solution ($\varnothing = 200$ nm, $c(\text{NaCl}) = 0.25$ M, $F_N = 300$ nN). During the first five hours a weakening of the pillars occurs, which stops after the sixth hour and finally the pillar breaking strength increased (Fig.5.4b). The following conclusions can be deduced based on this behavior: At least two processes are involved in this phenomenon, one that weakens the pillars while the other strengthens them. Both processes are time dependent, but the process that leads to a weakening has a smaller time constant than the process that leads to a strengthening. After a certain time, the process that leads to a strengthening dominates over the weakening process.

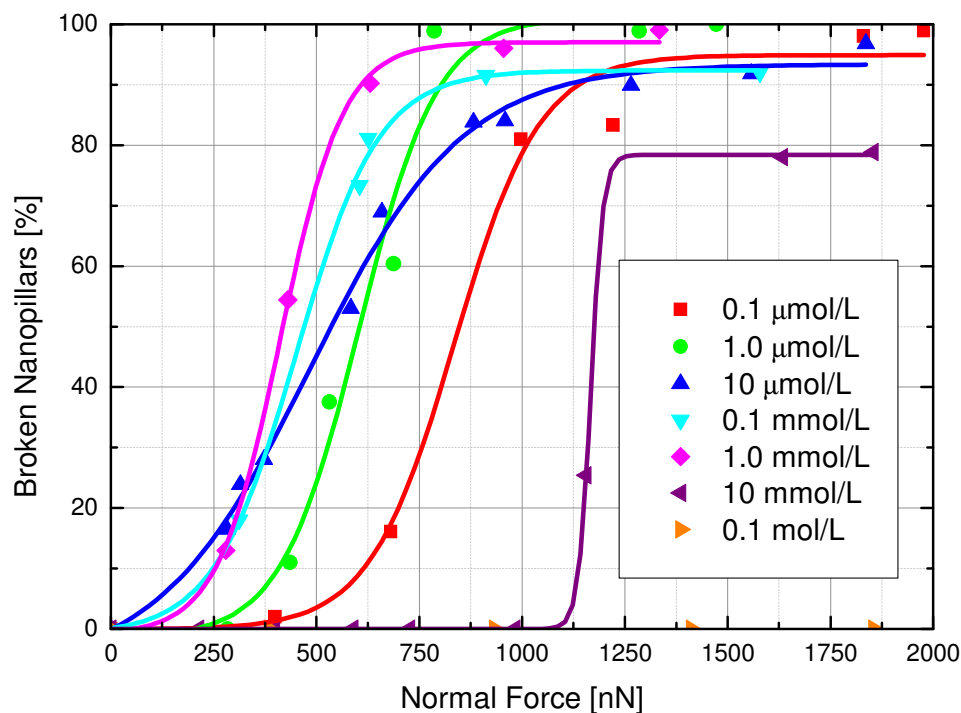


Fig.5.5: Fracture experiments in solution ($\varnothing_{\text{nanopillar}} = 260$ nm): The experiments were performed in aqueous NaCl solutions with different concentrations, using different normal forces. First, the pillars were equilibrated for approximately 24 hours in the corresponding solution. The NaCl concentration was increased with each experiment. After each solution change, the pillars were equilibrated for at least 14 hours.

In a further experiment, the concentration dependent behavior at different normal forces was examined. A nanopillar sample chip was equilibrated in an aqueous $0.1 \mu\text{mol/L}$ NaCl solution and measured within the next day at different normal forces. After such a measurement, the sample chip was equilibrated in a 10-fold higher concentrated solution for at least 14 hours. This procedure was repeated until the NaCl concentration reached 0.1

mol/L. The shown sigmoid curves in Fig.5.5 shifted to the left with the increase in concentration. This phenomenon occurs only for experiments with a concentration up to 1.0 mmol/L. Pillars equilibrated with higher NaCl concentrations (e.g. 10 mmol/L) showed a different behavior: The pillars showed a considerable strengthening instead of a weakening (Fig.5.6). This means that now the curves are shifted to the right. A further increase of the NaCl solution to 0.1 mol/L leads to a complete stabilization. It was no longer possible to break pillars, not even with normal forces of up to 2 μN .

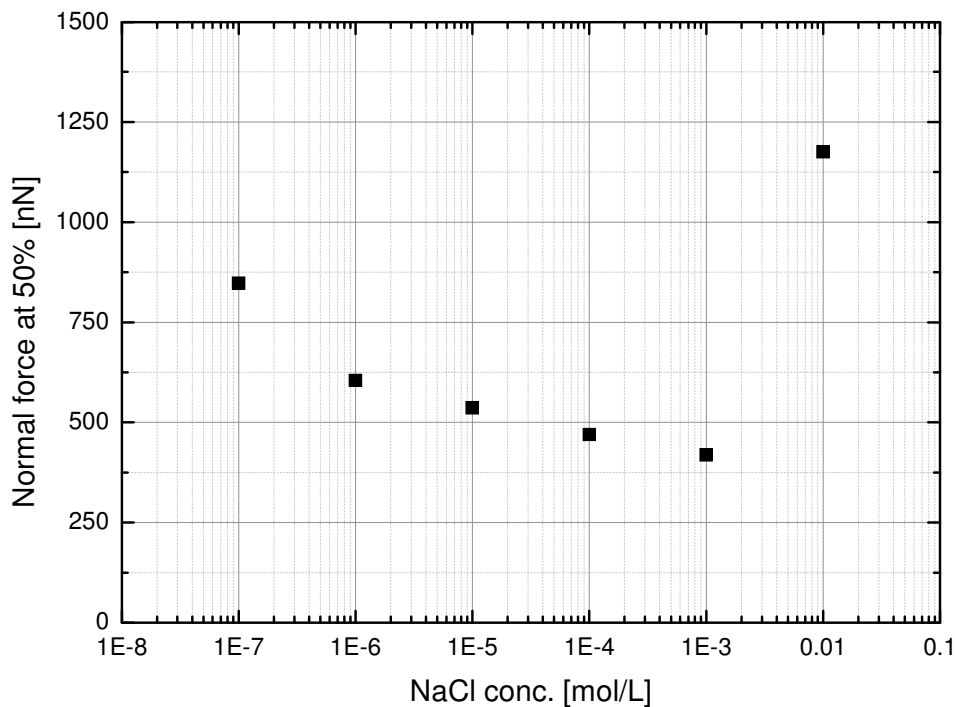


Fig.5.6: In this graph the 50% values, of the sigmoid curves (see Fig.5.5) as a function of the concentration, are shown. Clearly visible is the decrease of the normal force (weakening of the pillars) until a concentration of 1.0 mmol/L NaCl is reached. Obviously, there is no 50% value for the 0.1 mol/L concentration because no pillars were broken. This means that a total stabilization of the pillars occurred.

In another experiment, the kinetic behavior was scrutinized. Here, the nanopillar sample chip was first measured in water, then the fluid medium was changed to NaCl and then back to water again (Fig.5.7). The used nanopillars had a diameter of 260 nm and a normal force of 1000 nN was applied to test their fracture behavior. In Fig.5.7, the first, yellow colored section was measured in water. The increase at the beginning occurs due to the hydration effect. The following change to an aqueous 0.1 mol/L NaCl solution is shown in the middle zone. As expected, the change from water to NaCl causes a weakening. However, there was no initial increase contrary to the data shown in Fig.5.4b. This effect may be caused

by the used NaCl solution because the NaCl concentration in Fig.5.4b was 0.25 mol/L whereas the NaCl concentration in this experiment is lower, i.e. 0.1 mol/L.

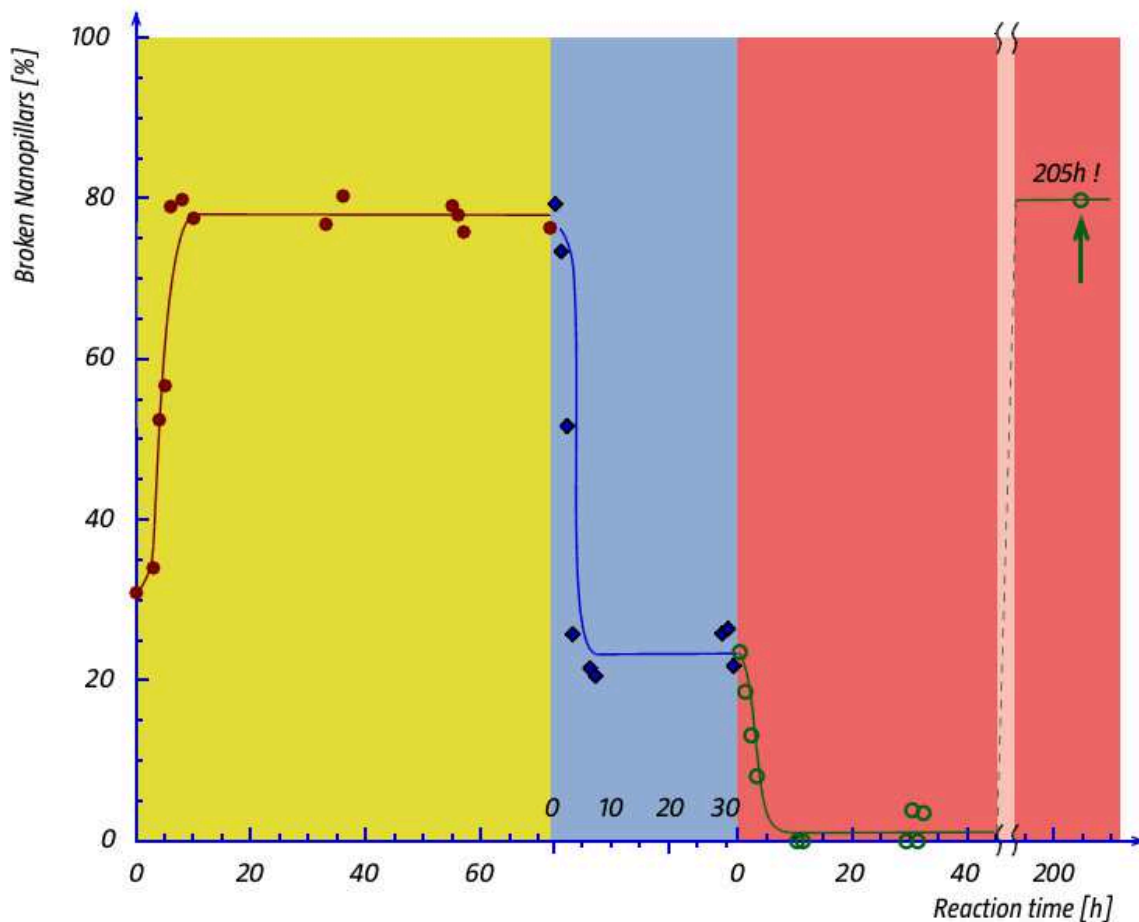


Fig.5.7: Fracture experiments with changing liquid phases. In the first phase, a new sample chip, which wasn't exposed to water previously, was measured in water. The increase of the fracture rate can be interpreted as a consequence of the hydration of the nanopillars and consequent weakening of the pillars. In the second phase, the water was exchanged with a 0.1 mol/L NaCl solution. After approximately six hours, the NaCl solution caused a stabilization of the pillars from 80% to approximately 20% of broken pillars. In the last phase, the sample chip has been exposed to water again. Interestingly, there is no weakening visible, i.e. the initial state can not be reached but a nearly 100% stabilization occurs. The initial state of approximately 80% of broken nano pillars can be reached after some days.

The nanopillar stabilization occurs after approximately six hours. In the third section, the sample chip was measured in water again. Interestingly, a stabilization of the nanopillars is noticeable. This stabilization lasts for a very long time. However, after about a week (i.e. around 150 hours) the amount of broken pillars was again at around 80%. This demonstrates that changes from water to an electrolyte solution and then back are all in all entirely reversible even though they need some time until they reach the value from the beginning.

5.4. *Interpretation of the measured data*

The weakening of fresh nanopillars, which were never before exposed to water, can be explained by microcrack stabilization. This stabilization occurs due to water molecules diffusing into the crack gap. The crack closing process needs energy for liquid displacement, hence it will stabilize the crack. Furthermore, stabilization occurs through the dipolar nature of the water molecules. A crack always means that a multitude of chemical bonds have been broken. The binding electrons, as a result of the higher electronegativity of oxygen compared to silicon, are not divided equally among the atoms. Hereby, the atomic groups, which are shielded by the water dipole, become positively and negatively charged. As a consequence, the attractive Coulomb interaction between the ionic groups is weakened.

Certainly two or more processes are involved in the NaCl experiments. As already mentioned, a fast, weakening and a slow, stabilizing effect are involved. Furthermore, it could be shown that a strengthening of the nanopillars occurs only above a certain NaCl concentration and after some time. Therefore, it can be imagined that the fast process is linked to the surface, while the slow process can be associated with the interface and/or the bulk of the pillar. A most plausible explanation for the surface process is the ion adsorption and the formation of an electrical double layer, respectively. The weakening can be explained by the increased stabilization of cracks, also in the vicinity of the interface.

The nanopillar strengthening most probably occurs due to a bulk or more precisely due to an interface related phenomenon. Particle diffusion into a material is considerable slower than any adsorptive process. The velocity of an adsorption process is determined by the flow of particles per unit area and per unit time, i.e. the flow is essentially given by the particle concentration. The observed latency for the strengthening effect would therefore better fit to a diffusive process. Further evidence, which anticipates diffusion for the strengthening, is its dependency on the involved concentrations. As already known [5.8], alkali metal ions accumulate at the SiO₂/Si interface which can be explained by the lower packing density compared to the volume SiO₂. In literature [5.9], one explanation for strengthening involves the formation of electrical dipoles at the interface. The experiment presented in Fig.8 can now be explained with the aid of the following illustration (Fig.5.8):

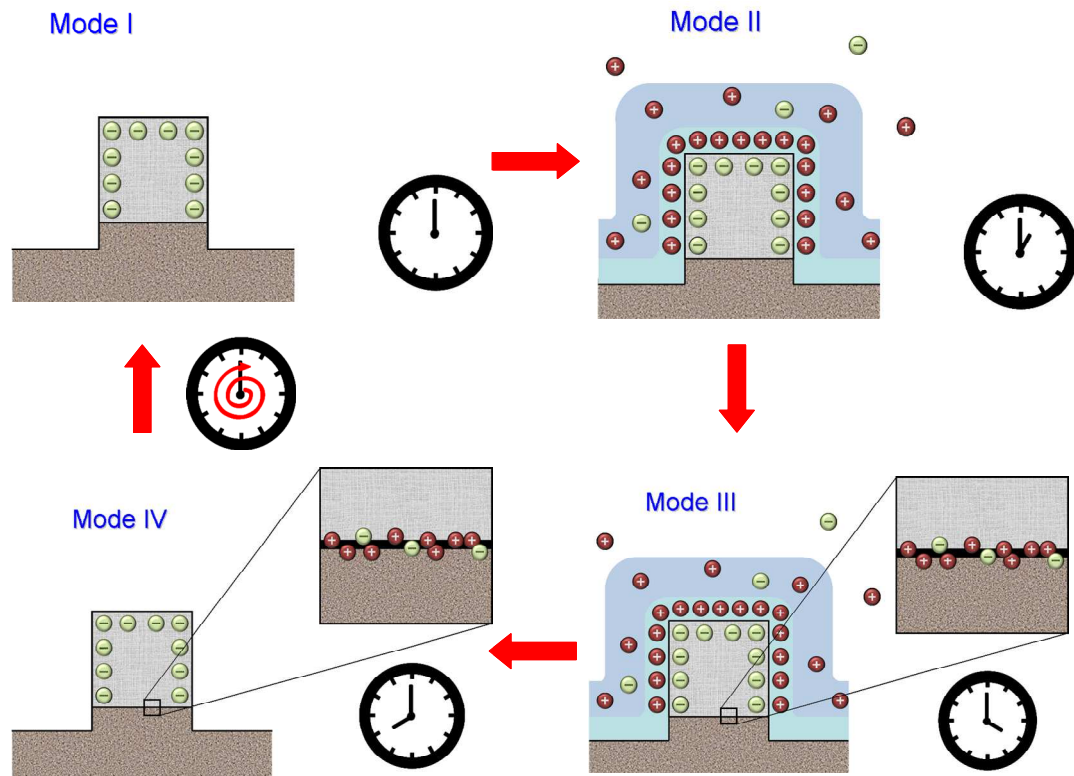


Fig.5.8: Schematic overview of the processes that probably occur in the experiment shown in Fig.8. **Mode I** shows a pillar in pure water. The surface is charged negatively because the surface silanol groups were partly deprotonated. An electrical double layer forms around the nanopillars after the exchange of water with an aqueous NaCl solution (**Mode II**). If the NaCl concentration is high enough and after some time, the ions will diffuse into the material, mainly to the region of the interface (**Mode III**). After the pillar is washed with pure water, the electrical double layer disappears but the ions remain on the surface (**Mode IV**). After an enough long period of time in water, the ions at the interface disappear. The pillar can achieve its initial state as long as the sample is washed several times with fresh water (again **Mode I**).

In water, the SiO_2 surface is negatively charged (Mode I). The negative charge comes from the partly deprotonated silanol groups ($\equiv\text{Si-OH}$). An electrical double layer (EDL) is formed (Mode II), when an electrolyte, as for example NaCl, is added to the solution. The pillar is weakened by the ions which have a stabilizing character onto the microcracks. Ions (mainly cations, as SiO_2 in water is negatively charged) diffuse into the interface region as long as the electrolyte concentration is high enough (Mode III). Based on the decreased packing density at the interface, the diffusion rate at this position is enhanced. The pillar strengthening occurs because an electrical dipole is formed alongside the boundary of the two involved materials. The electrical double layer at the surface gradually disappears, when the NaCl solution is removed and the environment changed back to pure water (Mode IV). This means that the weakening effect by the surface ions disappears while the interface strengthening persists.

During this stage, the pillars gain their maximum stability. After a certain time, the ions will also diffuse out of the interface. The pillars can achieve their initial state, as long as the water is periodically exchanged with fresh water.

A final point has to be mentioned: In solution, not only the surface chemistry can be modified, but also the friction. Therefore the tip-pillar interaction has to be taken into account when a liquid environment is present. Due to the variation of NaCl concentration, this can be further varied. An enhanced friction can be the reason for higher impact and lower forces for breaking. Furthermore, the removal of broken pillars may be different. While in dry environment the pillars stick to the tip due to electrostatic charging, in water this tendency is removed, leading to a better detachment of pillars from the tip. The result would be a more defined breaking of pillars since the tendency of debris to stick to the tip would be lowered. In this research, these effects have not been seen to be present or significant, so we assume that our conclusions are valid.

5.5. References

- [5.1] Griffith, A.A., *The Phenomena of Rupture and Flow in Solids*. Philosophical Transactions of the Royal Society of London, 1920. **221**: p. 163-198.
- [5.2] Sjoberg, S., *Silica in aqueous environments*. Journal of Non-Crystalline Solids, 1996. **196**: p. 51-57.
- [5.3] Lane, M.W., J.M. Snodgrass, and R.H. Dauskardt, *Environmental effects on interfacial adhesion*. Microelectronics Reliability, 2001. **41**(9-10): p. 1615-1624.
- [5.4] Wiederhorn, S.M., E.R. Fuller, and R. Thomson, *Micromechanisms of crack growth in ceramics and glasses in corrosive environments*. Metal Science, 1980. **14**(8-9): p. 450-458.
- [5.5] Michalske, T.A. and S.W. Freiman, *A molecular interpretation of stress corrosion in silica*. Nature, 1982. **295**(5849): p. 511-512.
- [5.6] Overgaard, J.V., *Experimental results of the influence of ionic strength in liquid environment on fibre life*, in *Optical Network Engineering and Integrity*, H.H. Yuce, D.K. Paul, and R.A. Greenwell, Editors. 1996, Spie - Int Soc Optical Engineering: Bellingham. p. 64-71.
- [5.7] Kooi, E. and M.V. Whelan, *On the role of sodium and hydrogen in the Si-SiO₂ system*. Applied Physics Letters, 1966. **9**(8): p. 314-&.
- [5.8] Gershinskii, A.E., et al., *Investigation of alkali metal migration and accumulation in the SiO₂/Si system: Structure of the interface*. Thin Solid Films, 1980. **70**(2): p. 341-349.
- [5.9] Distefano, T.H. and J.E. Lewis, *The influence of sodium on the Si-SiO₂ interface*. Journal of Vacuum Science & Technology, 1974. **11**(6): p. 1020-1024.
- [5.10] Buck, T.M., et al., *Studies of Sodium in SiO₂ Films by Neutron Activation and Radiotracer Techniques*. Journal of the Electrochemical Society, 1967. **114**(8): p. 862-866.
- [5.11] Delgado, A.V., et al., *Measurement and interpretation of electrokinetic phenomena - (IUPAC technical report)*. Pure and Applied Chemistry, 2005. **77**(10): p. 1753-1805.
- [5.12] Bousse, L., et al., *Zeta Potential Measurements of Ta₂O₅ and SiO₂ Thin Films*. Journal of Colloid and Interface Science, 1991. **147**(1): p. 22-32.

6. THE TITANIUM POLYIMIDE INTERFACE

Polyimides have gradually increased their importance for numerous microtechnological applications. They serve as substrates for flexible electronic devices which are achievable by the realization of printed circuit board (PCB) tracks on top of a polyimide (PI) foil. Despite the large efforts to increase the metal-PI adhesion, e.g. by activation with reactive plasmas [6.1-6.4], it still happens that the reliability of such a product will lie below demanded expectations. It is believed that this is caused by water contaminations on top of the PI surface [6.5].

6.1. Introduction

Polyimides are thermoplastic polymers, which are characterized by a high thermal endurance (up to $\sim 400^{\circ}\text{C}$) and a high electrical resistivity [6.6]. These properties render them ideal in microtechnological applications. Furthermore, thin PI films provide the base for their application as flexible circuit boards interconnecting small electronic devices (e.g. surface mounted device (SMD) technology) in a multitude of applications [6.7]. Thereby, these boards can be bent easily to facilitate assembly of electronic circuitry in compact housings like cellular phones or for devices used in invasive surgery. Unfortunately, the adhesion of PI to metals, e.g. to copper or gold, is often limited and at times insufficient for a particular application demanding a certain number of load or heating/cooling cycles [6.1]. Despite the large efforts to increase the adhesion between PI and metals, e.g. by plasma activation [6.2], the reliability of the interface, as well as the reproducibility of the manufacturing processes with regard to interface strength can provide a technological challenge. For this reason, titanium (Ti) is used as an adhesion promoter, which shows a sufficient adhesion between the PI and the following metal. However, it still happens that the Ti lacks sufficient adhesion. A possible explanation for this behavior may be that, based on different holding times of the semi-finished products as well as the differing air humidity during production, water layers [6.8] will form on top of the PI, which then will affect the adhesion to the Ti [6.9]. Based on this hypothesis, samples with 0, 1 and 5 Langmuir (L) of water between the Ti and the PI layer were prepared.

The purpose of this work is to examine whether water is responsible for the sporadic observed insufficient adhesion between Ti/PI or not. The SFM technique, as described in this

work (chapter 4) was used to determine this problem. Furthermore, measurements were performed using TEM, which should enable a comparison between TEM and SFM technique and should demonstrate the possibilities respectively the limitations of both techniques.

6.2. TEM, FIB and XPS

6.2.1. Transmission electron microscopy

Transmission electron microscopy is used for observations regarding very small structures (few μm down to some \AA). A sample is illuminated in transmittance by electron waves in analogy to the light radiation in optical microscopy. For this reason, the sample must be very thin (50 to 100 nm). The demanded sample thickness depends on the atomic number and the used acceleration voltage. That means, the higher the atomic number and the lower the acceleration voltage, the thinner the sample must be. Typical acceleration voltages range between 100 and 300 kV.

Electrons are emitted by thermal (e.g. by a LaB_6 filament) or by field emission and then routed by a lens system onto the observed sample. The electrons are collimated by magnetic lenses to uniformly illuminate the sample. The electrons are then scattered by the sample, where some of them lose kinetic energy (inelastic scattering). In the afterwards emerging focal plane, the electrons leaving the sample at the same angle are focused into one point. In this plane one can selectively pass the unscattered electrons with the help of an aperture. Atoms scatter more strongly the higher the atomic number respectively the bigger their radius are. The resulting contrast is called mass-thickness contrast.

Finally, the electrons of the image plane are expanded and therefore the object is seen strongly enlarged on a fluorescent screen which can further be captured by a CCD camera.

6.2.2. Focused Ion Beam (FIB)

FIB stands for focused ion beam and is used in micro- and nanotechnology. With focused ion beam systems one can depict sample surfaces with a high resolution. Furthermore, arbitrary structures can be realized by sputter erosion, chemically induced etching and material deposition. A FIB is operated similar to a scanning electron microscope (SEM). Instead of an electron beam, in FIB an ion beam (usually gallium ions) is used to obtain the structure of the sample surface. If the device is equipped with an ion and an

electron beam (called cross beam or dual beam) the simultaneous processing and monitoring of the sample is possible. In FIB the ion beam hits a sample surface with a high kinetic energy to eject the atoms out of its surface network. The resulting secondary ions and secondary electrons can be used to map the surface. This technique can also be used for material processing in the nanometer range. Especially for the preparation of TEM lamellae the FIB has proved indispensable.

6.2.3. X-ray induced photoelectron spectroscopy (XPS)

The photoelectric effect was first described by Einstein. PES (photoelectron spectroscopy) can reveal information about the chemical composition of a surface. If a substance is exposed to X-ray radiation two different interactions are possible: There is the absorption of X-rays followed by the emission of low energy X-ray radiation (X-ray fluorescence). The other possibility is the knocking out of a valence electron (photoelectron). In this case a core level electron can jump into the remaining electron hole (external photoelectric effect). If the energy difference is high enough it can trigger another electron, the so-called Auger electron, to leave the atom (internal photoelectric effect). Both types of electrons are accelerated towards an analyzer and evaluated according to their kinetic energy. The kinetic energy of the emitted photoelectrons can be described as follows:

$$E_{kin} = h\nu - E_b - \Phi_{spect} . \quad (\text{Eq.6.1})$$

Here, $h\nu$ is the used X-ray energy ($\text{MgK}\alpha$ or $\text{AlK}\alpha$), E_B the binding energy of the valence electrons (refers to the chemical potential) and Φ_{spect} the spectrometer work function which must be determined by a calibration.

6.3. *Material and methods*

6.3.1. Overview

Figure 6.1 shows a schematic representation of the experimental procedure: The drawing is divided into three areas (color online), corresponding to (i) the fabrication of the probed interface, (ii) the structuring of the nanopillars and (iii) the investigation by SFM. The procedure starts with the preparation of a PI thin film in the UHV (1). After H_2O dosing onto

the cured PI film (2) and X-ray photoelectron spectroscopy (XPS) characterization (3), a thin layer of Ti is deposited (4). The samples are then transferred through ambient air to a FIB lithography setup in order to produce nanopillar patterns with specifically chosen dimensions (5). Subsequent SFM experiments are performed in air (6) and reveal the statistical fracture behavior of the nanopillars. Notably, the depth of the trenches between the pillars determines the height of the pillar and the elevation of the interface above the pillar base.

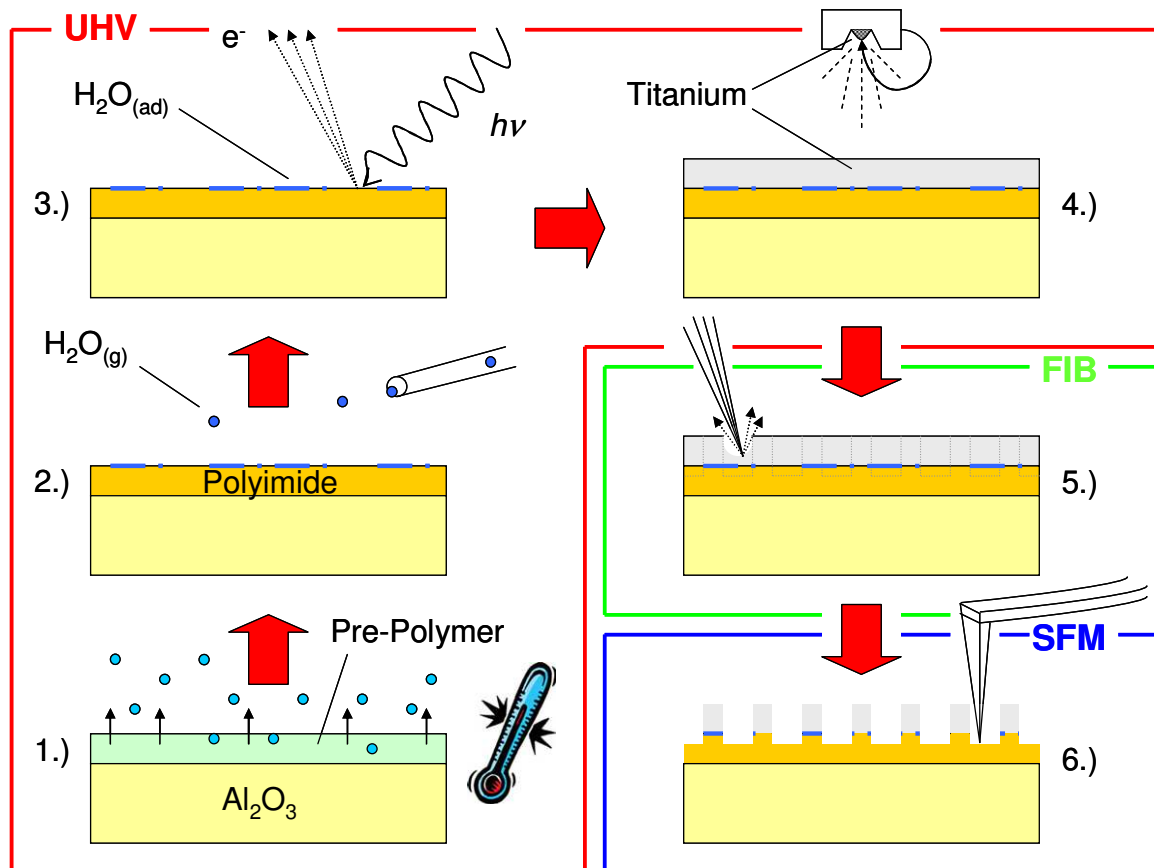
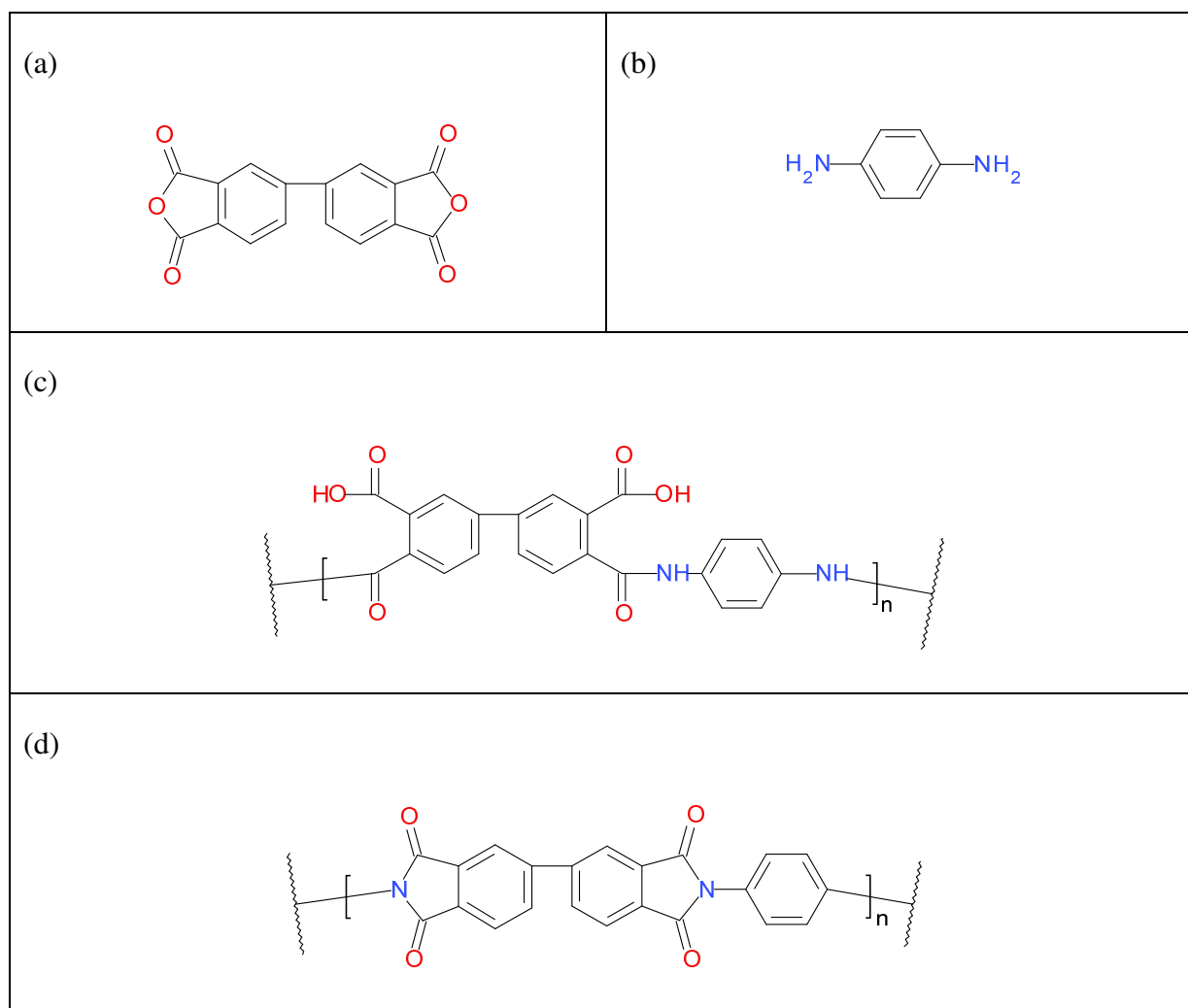


Fig.6.1: Schematic figure of the individual process steps: 1.) Hardbake of the polyimide pre-polymer, 2.) water deposition from the gas phase, 3.) XPS measurement as control, 4.) titanium evaporation of the with water modified surface, 5.) pillar structuring by FIB, 6.) fracture experiments by the SFM.

6.3.2. Used materials

For easier handling an Al_2O_3 ceramic of Ceramtec was used as a sample support material ($4'' \times 4'' \times 0.025''$). The polyimide (to be precise, the polyamidic intermediate (Tab.6.1c)) was obtained as 13.5 wt-% solution in NMP (N-methyl-2-pyrrolidone) from HD Microsystems (Pyralin PI-2611). A polyimide is a polycondensate of the AA/BB type which

must be converted thermally (hardbake) into the final product (Tab.6.1d). The thermally induced ring closure reaction is carried out by the loss of two water molecules per monomer unit. The here used monomer consists of a BPDA (biphenyl dianhydride) (Tab.6.1a) and a PPD (para-phenylene diamine) (Tab.6.1b) unit.



Tab.6.1: (a) BPDA (biphenyl dianhydride), (b) PPD (paraphenylene diamine), (c) Polyamic precursor of Pyralin PI-2611, (d) Polyimide (Pyralin PI-2611).

6.3.3. Preparation of the samples

The polyimidic precursor was spun on top of the Al_2O_3 ceramic wafer for 15 min using a spincoater at 105 °C (softbake). With a wafer saw the ceramic wafer was cut into 10 mm × 10 mm pieces. The transformation (hardbake) of the polyamic precursor into the final polyimide was performed in a UHV chamber ($p \sim 10^{-9}$ mbar) by heating the sample piece with a resistance heater (filament) located below the sample. First the sample temperature was raised by 2 °C / min up to a level of 200 °C and then kept constant for 1h. Next, the sample

was brought up to a temperature of 380 °C (2 °C / min) and was held there for 30 min (verified by a pyrometer). In an adjacent chamber containing some water vapor (from thermally decomposed $\text{CaSO}_4 \cdot 2 \text{H}_2\text{O}$ (gypsum)) the required amount was introduced into the sample chamber via a precise dosing valve. The pressure in the sample chamber was always maintained in the UHV range during the water deposition process. By regulating the exposure time $t_{\text{exposition}} = f(p)$ the desired coverage was adjusted. The characteristic quantities are based on the kinetic gas theory (Maxwell-Boltzmann distribution). The mean particle velocity (in our case of water) is defined by

$$\bar{v}(\text{H}_2\text{O}) = \sqrt{\frac{8kT}{\pi \cdot m(\text{H}_2\text{O})}} \quad (\text{Eq.6.2})$$

Here, k stands for the Boltzmann constant, T is the temperature and m is the mass of a water molecule. The particle flow to the surface, the collision rate $Z_{(s)}$ (number of particles per unit time and unit area) is calculated by

$$Z_{(s)} = \frac{1}{4} N_{(v)} \bar{v}(\text{H}_2\text{O}) \quad (\text{Eq.6.3})$$

where $N_{(v)}$ is the particle density in a given volume. The gas pressure depends on $N_{(v)}$ which is defined through the ideal gas law:

$$p = N_{(v)} kT \quad (\text{Eq.6.4})$$

t_{mono} is derived from the assumptions that the sticking coefficient S is equal to 1 and that the particles are separated by each other by a value of about 3.8 Å. The mean free path Λ_M is given by

$$\Lambda_M = \frac{1}{\sqrt{2} \cdot N_{(v)} \cdot q} \quad (\text{Eq.6.5})$$

where q is the effective collision cross section parameter ($q(\text{water}) = 5 \cdot 10^{-19} \text{ m}^2$).

Samples with 0, 1 and 5 L of water at the interface position were prepared. Every sample was manufactured twice. One part of the samples was used for XPS while the other part was processed. The experiment was performed this way because the holding time in vacuo must be chosen as short as possible to avoid any further adsorption of water particles and diffusion into the polyimide. After water deposition, the titanium was immediately deposited (200 nm thickness) on top of the modified surface (via e-beam evaporator).

6.3.4. Nanopillar production using FIB

The nanopillar production was done by means of FIB and not by traditional lithography. The major advantage of the FIB technique is that it is a direct write process. This means that no resist, no mask and no post-processing (wet-chemical steps) are needed. In particular, the wet chemical processing would probably have destroyed the polyimide. A major FIB disadvantage is the sequential operation mode which makes it very slow. Furthermore, by approaching the nanometer scale, the FIB slowly comes to its resolution limit. The pillar size and depth were indirectly set, as the removal rates for titanium and polyimides are not known. SFM experiments for fracture mechanics are only accomplishable in a “small” force window, therefore appropriate pillar dimensions had to be found by trial and error. For this purpose, pillar arrays (each field consisting of 16 pillars) are made by FIB (Fig.6.2).

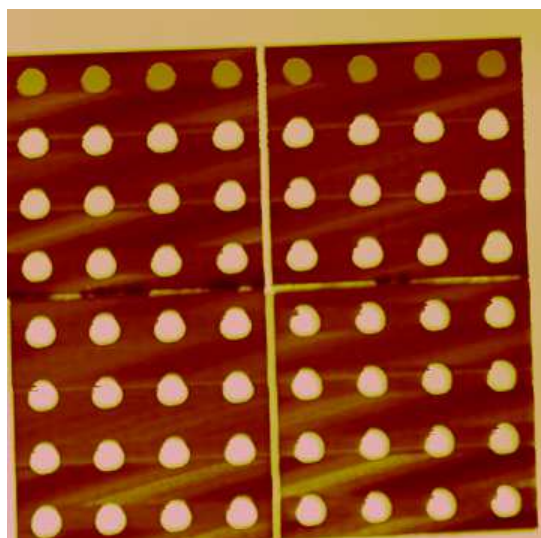


Fig.6.2: SFM height image of a Ti/PI nanopillar array. The pillars were made by means of a FIB. For this purpose a gallium ion beam is directed over the sample surface while milling away the material underneath. In this process the actual etching depth is always deeper than the thickness of the Ti layer ($d \sim 200$ nm). In this graph, the top line of nanopillars is already broken off at the position of the interface.

Finally, the used nanopillars were manufactured by the following FIB parameters: Magnification of 1:70000, beam current of 80 pA, acceleration voltage of 30 kV, relative etching depth of $0.8 \mu\text{m}$ related to SteelHT (high tensile steel) with a total production time

(per field with 16 pillars) of 22 min. In metric units this corresponds to a diameter of 1.0 μm and a period of 2.1 μm . However, due to the different thicknesses of the Ti layer the characteristic pillar heights are slightly different (see Table 6.2):

	Thickness of the Ti layer [nm]	Total pillar height [nm]	Interface height from the basis [nm]
0 L	220	380	160
1 L	160	420	260
5 L	170	390	220

Tab.6.2: Tabulated thicknesses of the titanium layers, the entire nanopillar heights and the heights of the interface position as seen from the base up to the boundary layer position.

6.4. Results

6.4.1. XPS

As expected, XPS measurements show an oxygen increase (At-%) as a function of the surface water coverage. One Langmuir causes a nearly imperceptible increase of the O1s signal whereas five Langmuir show a significantly larger signal (Tab.6.3).

	0 L [At-%]	1 L [At-%]	5 L [At-%]
O1s	13.7	13.9	16.1
C1s	78.1	78.3	77.6
N1s	8.0	7.7	6.2

Tab.6.3: Element concentration in atom-% of oxygen, nitrogen and carbon for samples with 0, 1 and 5 Langmuir each of adsorbed water on the surface.

The unfolded spectra of the O1s peaks show a signal for the water oxygen and one for the polyimide oxygen. This result demonstrates the successful deposition of water (Fig.6.3) on top of the polyimide surface.

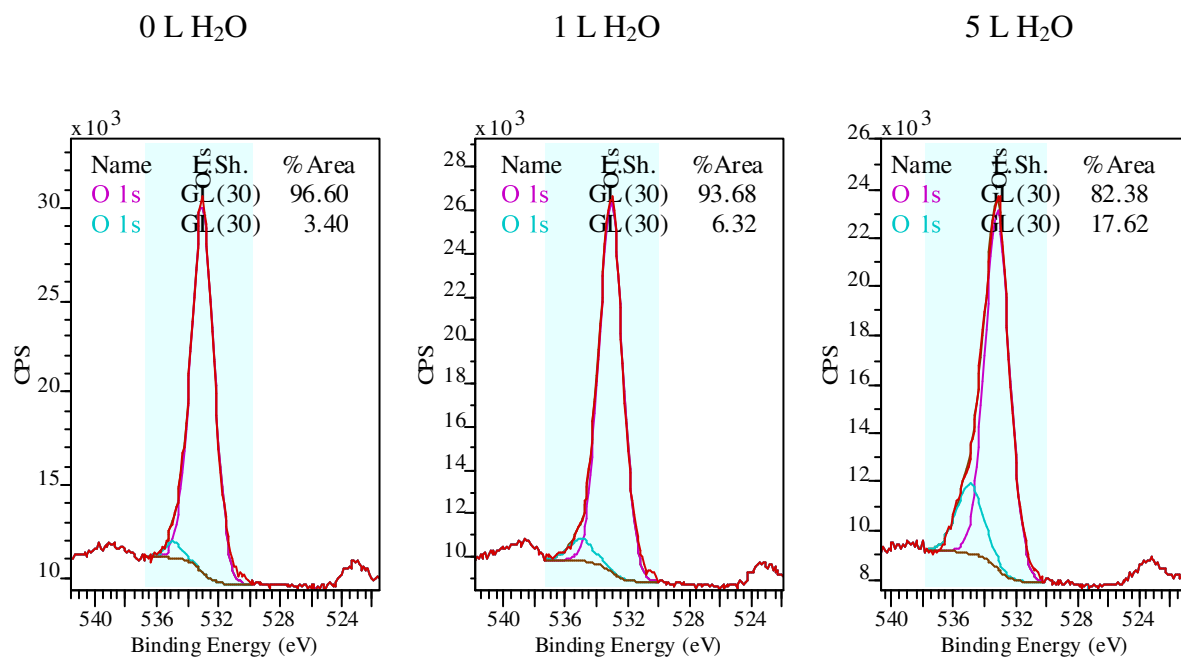


Fig.6.3: Detailed spectra of the O1s signal of all three samples. The O1s peaks were unfolded to show a signal increase which originates from the adsorbed water.

The measured signal of 3.4 At-% for the 0 L sample means that a small amount of water is already present. This water may originate from residual bulk water which diffused to the sample surface. Correcting the sample values with this 3.4 At-% one obtains the values in Table 6.4:

	0 L [At-%]	1 L [At-%]	5 L [At-%]
O1s (H2O)	3.4	6.3	17.6
O1s (H2O) corrected	0	2.9 (2.9 pro L)	14.2 (2.8 pro L)

Tab.6.4: Presented here is a fraction of the O1s signal which originates from adsorbed water. Also the sample where no water was deposited contains some water traces on its surface. Correcting all samples with this value, a mean O1s water signal increase of approximately 2.9 At-% per L of water is obtained.

6.4.2. Fracture experiments with the SFM

The realization of fracture experiments with Ti/PI nanopillars proved to be very difficult. Due to the non-statistical fracture behavior, a statistical analysis was often not possible. Many times it happened that an entire row (see Fig.6.2) or a whole field with 16 pillars in it was broken off, whereas the other pillars remained intact. Furthermore, it was observed that the narrow force regime, in which the number of broken pillars scales with the applied F_N , has been difficult to find. In the majority of the experiments either all or none of the pillars were broken off depending on the applied force. It is assumed, that this had to do with problems regarding the reproducibility of the FIB manufacturing process. Although the same FIB adjustments were used, the pillars, which were produced in the morning, looked different compared to the ones produced in the afternoon. This behavior was especially recognizable in form of the pillar shape which ranged from conical, roundish, oval to flattened. Finally, after lots of experiments, it was possible to manufacture pillars with a uniform shape. The SFM measurements were performed with a normal force F_N of about 180 nN. Fig.6.4 shows an array containing 16 pillars of the sample with 0 L water at the interface. In this array all pillars except one was broken off after the first area scan. The graph shows the height image in which two yellow lines are drawn. The yellow lines indicate the position of the height profiles shown on the top and on the right. The interface positions and, especially for the vertical profile, the exact positions, where the pillars were broken off, are getting clearly visible this way. Furthermore, it shows that most pillars were broken off at about a third of their diameter. However, a fraction of pillars was also fractured at first contact. The samples with 1 L and 5 L of water at the interface showed some unexpected results: According to these measurements, it could be shown that small amounts of water do not decrease the adhesion as originally expected. Instead, the adhesion could even be increased. A fracture statistics histogram, which expresses this behavior, is shown in Fig.6.5.

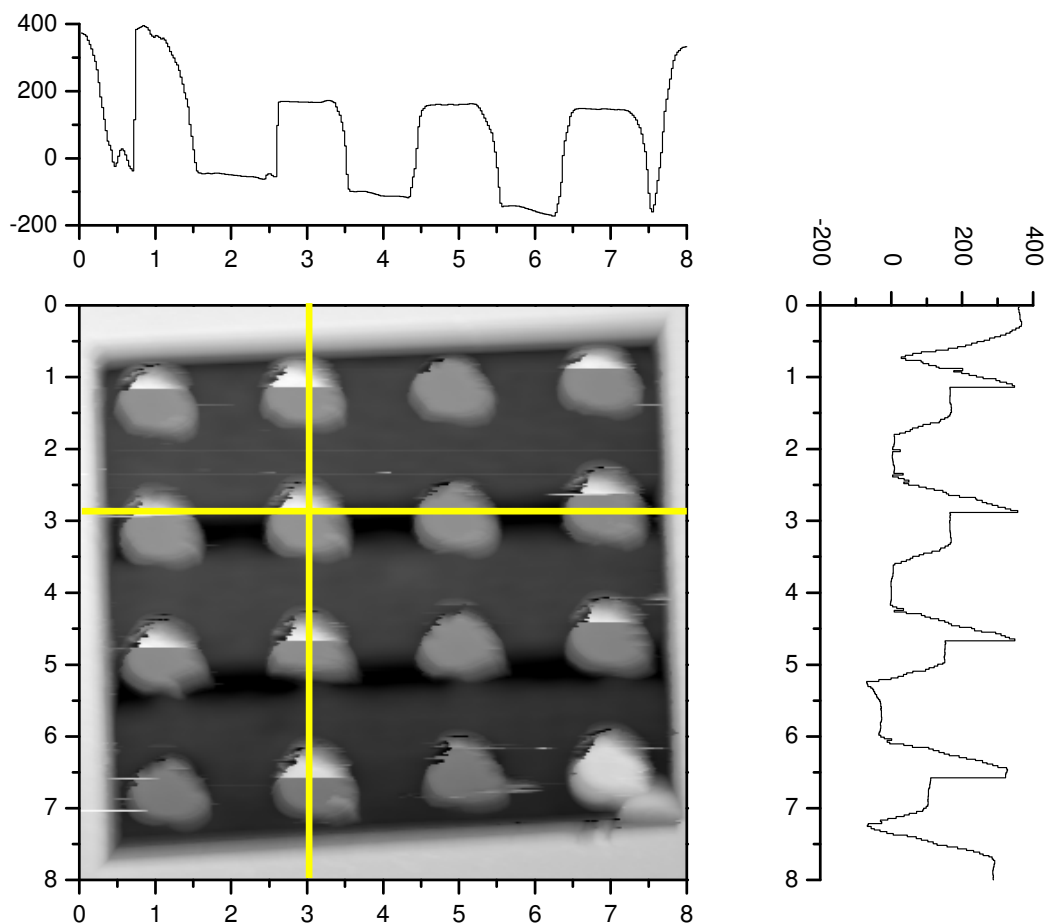


Fig.6.4: SFM micrograph section of a $10 \times 10 \mu\text{m}^2$ large scan field with 4×4 identical pillars produced with Ti/PI interfaces containing 0 L of water, as described in the main text. The data has been taken during the breaking experiment. Fracture incidents are recognized by pillars which are first imaged at their full height of $\sim 400\text{nm}$ and then, after the fracture incident, which occurs individually for each pillar, are imaged at the height of the remaining interface. The selected cross section above the figure represents the line scan at which the breaking event of pillar (2/3) occurred. Pillar (1/3) is still intact to be fractured in the next scan lines, pillar (3/3) was broken off at first contact and pillar (4/3) fractured earlier in the experiment. The cross-section in y-direction across the pillars in the second column combines data points from all scan lines and clearly shows that all pillars in this row are broken off, after some scan lines have initially imaged the pillars in this row at full height. The incidents are recognized by the abrupt change in measured height (saw-tooth).

There is a significant decrease of the percentage of fractured pillars with the samples that have been exposed to an increasing water dose. This trend is reflected by the fraction of the pillars which remained intact, as well as with those which have been observed to break off instantly, at first contact. Note that the Ti layer thickness varies from sample to sample ($H_{\text{Ti}}(0 \text{ L}) = 220 \text{ nm}$, $H_{\text{Ti}}(1 \text{ L}) = 160 \text{ nm}$, $H_{\text{Ti}}(5 \text{ L}) = 170 \text{ nm}$), which may under certain circumstances lead to an increased percentage of fracture observed for the pillars manufactured with zero water dose

(0 L). However, the significant difference in the fracture behavior observed for 1 L and 5 L exposure at the interface proves that it is not the height ($H_{Ti}(5 L) = 170 \text{ nm} > H_{Ti}(1 L) = 160 \text{ nm}$) of the Ti pillar above the interface, but the strengthening of the interface by the water which dominates the observed effects. Thereby, a significant strengthening of the interface by the water introduced into the fabrication process can be detected.

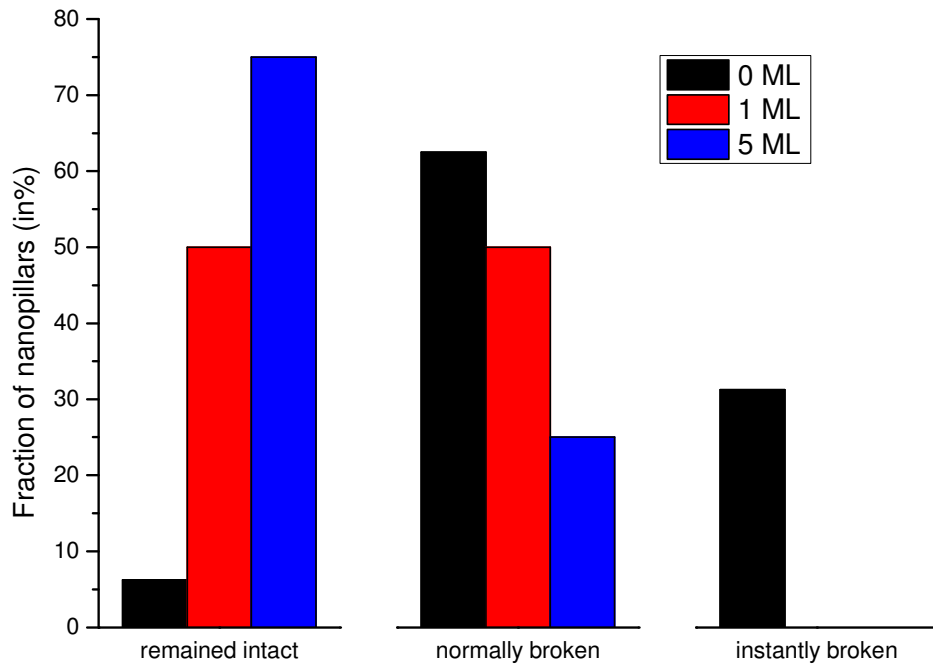


Fig.6.5: Fracture statistics histogram: Nanopillars prepared from Ti/PI interfaces after variable degrees of water exposure (0, 1, 5 L) have been scanned with a cantilever load of 180 nN perpendicular to the sample surface. The percentage of the pillars, which remain intact, significantly increases with the water dose. In full consistence the percentage of the pillars which are instantly broken off at first impact of the cantilever tip, decreases from a value of 31 % at 0 L exposure to zero at 1 L and 5 L exposure, respectively.

6.4.3. Determination of the friction and the lateral force

The lateral force determination is based on the Varenberg method (see chapter 3 for more information). For this purpose, a calibration factor α must first be determined. With this α , the lateral signal can be converted into a lateral force which, by a given normal force can further be converted into the friction coefficient μ . Tab.6.5 lists the values for the calibration test structure TGF11 (Si(100)). Interestingly, a decrease of the friction coefficient μ as a function of the normal force was observed. This decrease of the friction coefficient is

somewhat astonishing since Amontons second law states that the friction force is directly proportional to the normal force and therefore μ has to be constant.

Setpoint [V]	L [nN]	A [nN]	Calibration factor α [nN/V]	Friction coefficient μ
1	203	8	3317	0.30
2	402	8	2104	0.07
3	597	10	2008	0.07
4	777	11	1962	0.05
5	940	14	1596	0.05

Tab.6.5: Measured values for Si(100) for the given setpoint (defines the normal force): L is the normal force executed by the instrument, A is the adhesion force, α is the calibration factor that is deduced from the Varenberg method and μ is the friction coefficient on plain ground.

The reason for this has to do with the used cantilever tip. The tips consists of DLC (diamond like carbon) which, according to the literature [6.10], has in terms of a high acting contact pressure a lubricating effect similar to graphite. This has to do with the fact that DLC in its material properties lies somewhat between graphite (sp^2 hybridized) and diamond (sp^3 hybridized). A friction coefficient μ of 0.43 ± 0.08 can be calculated for titanium with a α -value of 3317 nN/V for 1V. Furthermore, for each W (the half value of the friction loop signal) a lateral force can be deduced. Unfortunately, during the pillar fracture process the photodetector signal always showed the maximum possible value of 10 V (saturation effect), regardless of the pillar diameter. Fig.6.6 shows the same image as Fig.6.4 but the shown values are representing the lateral force F_L instead of the height. The cropped signals are the reason why a serious analysis is impossible. Nevertheless, the unsaturated data from Fig.6.6 can be used to calculate the friction coefficient at specific positions.

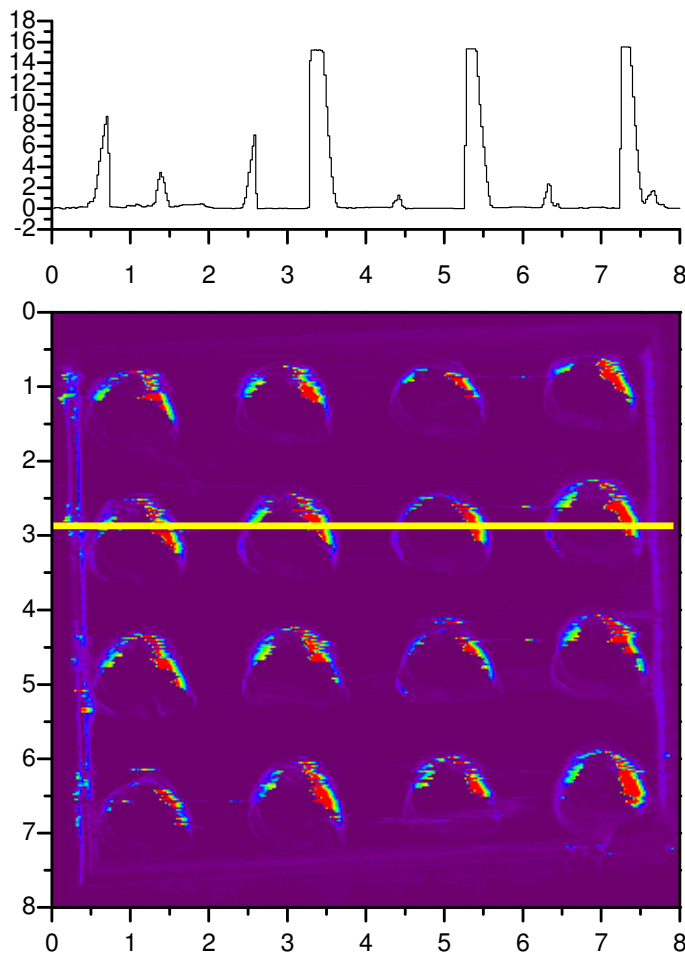


Fig.6.6: Here, the same nanopillars as shown in Fig.6.4 are displayed. However the z-signal represents the lateral force F_L instead of the height. The lateral force can be calculated according to the Varenberg method (see chapter 3). The yellow line indicates the position of the force profile, which is shown at the top of the image. Clearly visible are the cropped peaks, which should show the lateral force at the time of fracture. This saturation phenomenon is independent of the pillar diameter and could be explained by a (elastic) bending of the polymer socket. This would also explain why the saturation signal is still visible even after the pillar was broken.

Furthermore, the friction coefficient for the PI base level as well as for the fresh PI socket was calculated. Table 6.7 shows that the difference between the fresh PI (socket) and the old PI (base level) tends to zero with an increased amount of water at the interface. This can be interpreted as an indication that the physical properties of the 5 L PI socket are approximated to the base level PI.

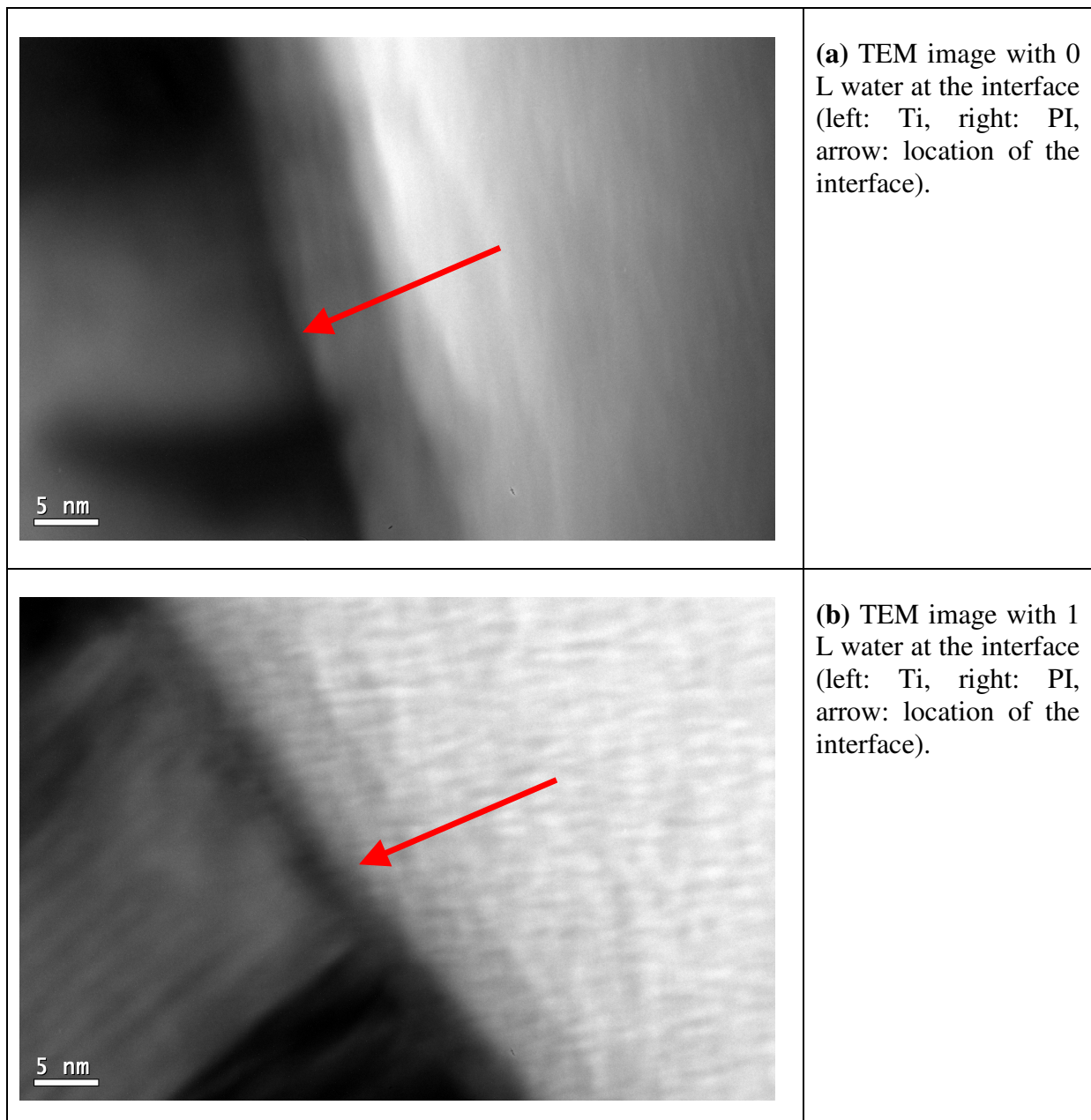
	0 L	1 L	5 L
$\mu(\text{PI})$	0.23	0.19	0.22
$\mu(\text{PI socket})$	0.32	0.26	0.18
$\Delta\mu$	0.09	0.07	0.04

Tab.6.7: Shown are the friction coefficients μ for PI on the base level as well as for the PI surface as it appears immediately after pillar fracture. The calculated differences show a

decrease whereas the water content at the interface increases. With this, it is further possible to demonstrate that minimal amounts of water at the interface will influence the interface properties.

6.4.4. TEM

TEM measurements were performed to gain further insights concerning interfaces and to show differences between the water content. Fig.6.7a, b, c shows TEM images with a magnification of 1:500'000. However, there are no significant differences detectable. The only difference is that the interfaces with an increased amount of water are less rich in contrast and more blurred.



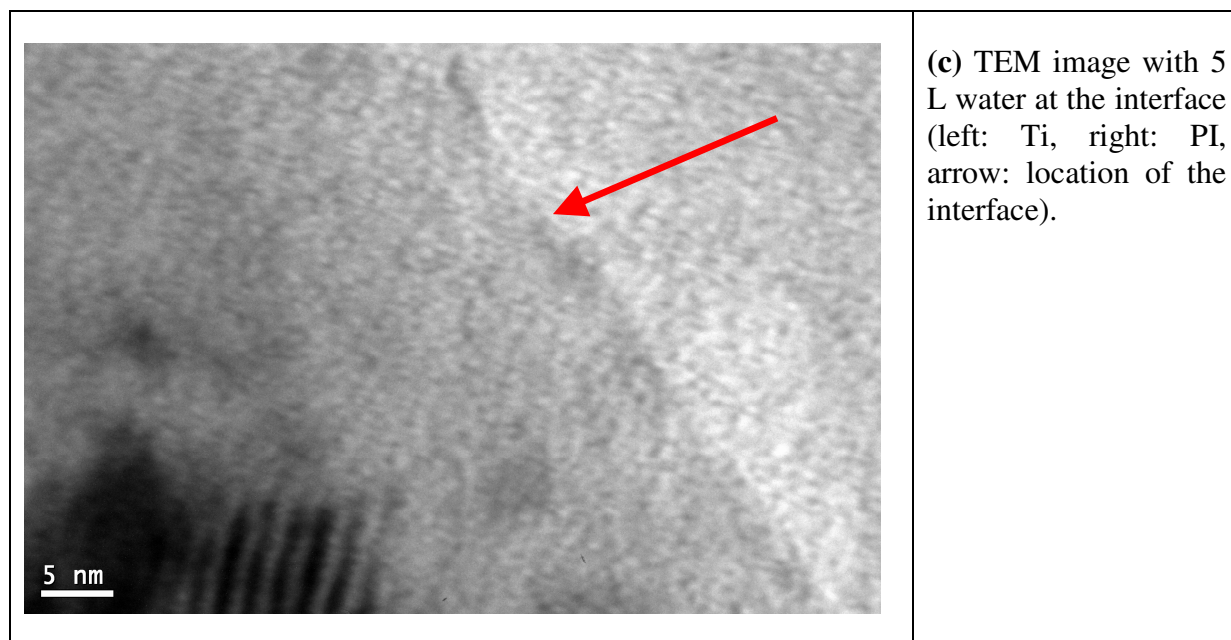


Fig.6.7a, b, c: TEM images of Ti/PI interfaces with a magnification of 1:500'000. The shown arrows indicate the position of the interface, whereby the Ti is on the left and the PI is on the right side of the image. A decreased contrast change between Ti and PI is visible while the interface water amount is increased from a) 0 L to b) 1 L to c) 5 L. This smearing, which suggests diffusion, can be a potential reason for the observed adhesion increase.

The less concise interface contour between Ti and PI can be a sign for the increased adhesion as measured by SFM. A blurred interface may be caused by a stronger diffusion of the two involved components into each other.

6.5. Summary and discussion

The Ti/PI fracture experiments were more difficult in their completion than the experiments with SiO₂/Si nanopillars. A statistical analysis was complicated due to the frequently insufficient reproducibility of the pillar production by means of the FIB. It could be shown that the FIB technique is not the best choice to fabricate reproducible structures in the nanometer range. But finally a statistical analysis was possible and very interesting results could be obtained. Contrary to the initially stated hypothesis that water should decrease the adhesion between Ti and PI, it could be shown that this is not the case. As could be demonstrated within the experiments, a few Langmuir of water can significantly increase the adhesion between these two materials. A possible explanation for this behavior could be that water induces an amid group hydrolysis of the cured polyimide. The consequence of this is an increased amount of carboxyl groups and secondary amines which leads to a better complexation of the Ti atoms. Another reason, which might explain the increased adhesion, is

given by the observations received from the TEM measurements which suggest that diffusive processes may be another cause that enhances the adhesion.

An alternative evaluation by the lateral forces was not possible since the detector at the time of fracture showed saturated signals. Indeed, it showed the potential feasibility of this approach. Another explanation for the sporadic observed poor adhesion between Ti and PI could be residual oxygen traces present in the vacuum chamber. It is a well known fact that Ti has an extremely high affinity to oxygen. If the titanium evaporation chamber always has to be vented before being filled with fresh samples, it is likely that the first evaporated titanium reacts with residual oxygen and thus the first deposited portion is some titanium oxide. Therefore, this inhomogeneous layer is possibly responsible for the sporadically observed insufficient adhesion.

6.6. References

- [6.1] Buchwalter, L.P., *Adhesion of polyimides to metal and ceramic surfaces: an overview*. Journal of Adhesion Science and Technology, 1990. **4**(9): p. 697-721.
- [6.2] Egitto, F.D. and L.J. Matienzo, *Plasma modification of polymer surfaces for adhesion improvement*. IBM Journal of Research and Development, 1994. **38**(4): p. 423-439.
- [6.3] Egitto, F.D., et al., *Oxygen plasma modification of polyimide webs: effect of ion bombardment on metal adhesion*. Journal of Adhesion Science and Technology, 1994. **8**(4): p. 411-433.
- [6.4] Nakamura, Y., Y. Suzuki, and Y. Watanabe, *Effect of oxygen plasma etching on adhesion between polyimide films and metal*. Thin Solid Films, 1996. **291**: p. 367-369.
- [6.5] Bodo, P. and J.E. Sundgren, *Adhesion of evaporated titanium to polyethylene: Effects of ion bombardment pretreatment*. Journal of Vacuum Science & Technology a-Vacuum Surfaces and Films, 1984. **2**(4): p. 1498-1502.
- [6.6] Mittal, K.L., *Polyimides and other high temperature polymers: synthesis, characterization and applications*, 2001, VSP: Utrecht.
- [6.7] Fach, A., et al., *Multilayer polyimide film substrates for interconnections in microsystems*. Microsystem Technologies, 1999. **5**(4): p. 166-168.
- [6.8] Kandasamy, K. and N.A. Surplice, *The interaction of titanium films with water vapour over a wide range of pressures and exposures*. Journal of Physics C-Solid State Physics, 1982. **15**(5): p. 1089-1097.
- [6.9] van Ooij, W.J., *Interfacial Interactions Between Polymers and Other Materials and Their Effects on Bond Durability*, in *Physicochemical aspects of polymer surfaces*, K.L. Mittal, Editor 1983, Plenum Press: New York. p. 1035-1091.
- [6.10] Radi, P.A., et al., *Friction and wear maps of titanium alloy against a-C:H20% (DLC) film*. Surface & Coatings Technology, 2008. **203**(5-7): p. 741-744.

7. SUMMARY AND CONCLUSIONS

With the here introduced method to mechanically probe nanopillars by SFM, mechanical tests are now applicable to probe pieces of a material, possibly containing an engineered interface, with external dimensions in the sub-micrometer range. For this purpose, nanopillars were fabricated by lithographic methods. In this thesis, nanopillars exhibiting dimensions ranging from 70 to 340 nm have been manufactured and probed mechanically. The fabricated pillars contain a very important characteristic trait: The material interface is implemented at a specific position within the height of the pillar. Nanopillars were engineered from SiO₂/silicon and titanium/polyimide polymer to establish the application of SFM nanomechanics to distinctively different materials and interfaces. In the case of both studied interfaces, it is the material interface which is the weakest part and which therefore acts as a predetermined breaking point. Nanopillars were fabricated with different characteristic dimensions, which allows for the determination of size effects and the like. Unlike in other nanoscale fracture assessments, e.g. in nanoindentation with subsequent SEM or TEM investigations, in the here presented experiments, a scanning force microscope (SFM) was used for both, for measuring the topography as well as for inducing well-defined forces to fracture in a controlled manner and to assess the fracture process and to analyze the residual 'stumps'.

The major number of experiments was performed while the scanning SFM tip was in close contact with the sample surface (contact mode). Most of the statistical experiments, where a certain area of a pillar array is scanned, were carried out in this mode. This way, the preset force acts on all pillars in the scan area in a comparable way, such that dozens of experiments, more exactly one hundred for a ten by ten array of towers, can be performed at once. It has been shown that, by using this statistical method, precise conclusions about the quality of the pillar production can be taken. Therefore, the presented method can be used for judging the fabrication quality and consequently guide towards the necessary steps for further optimization of the quality of the produced mechanical structures and interfaces. A unique advantage is that besides the topography one obtains information about the mechanical sample properties. In addition to the statistical experiments, modification experiments on single nanopillars were also performed. With the so-called tapping mode technique, it is possible to address and to fracture single nanopillars in a highly defined way. Hence, manifold possibilities for saving data this way are possible. Nanopillars made of SiO₂/Si are

chemically extremely resistant as even the Si surface is coated by the thin and naturally occurring SiO₂ layer which comprises an outstanding chemical resistance. Therefore, the SiO₂/Si pillars could be the choice for long-term storage applications or as a feature for identification purposes of e.g. identity cards or for stamps for e.g. expensive watches as an additional, hidden sign for proving the origin. Such pillars can be read out nearly unlimited times without altering.

Statistical fracture experiments were also performed in liquid media. The measurements proved to be highly interesting since the mechanical stress in combination with the interaction from the environmental fluid can either affect the surface or it can selectively interact with the nanopillars interface region. Both effects have been identified, side by side when SiO₂/Si nanopillars interact with brine (NaCl) solutions: A fast process with a weakening effect and a slow process with a stabilizing effect has been recognized. The adsorption of positively charged sodium ions and the consequent formation of an electrical double layer can be the cause of the fast and weakening process. The weakening can be explained by the stabilization of existing cracks at the surface. The slow, stabilizing effect is assigned to diffusive processes preferably occurring at the interface position. As adsorptive and diffusive processes occur on different time scales, a differentiation between these two is possible. A highly interesting discovery regarding these fracture experiments in liquids is the distinct dependency on the NaCl concentration. A novelty in the field of analytic chemistry would surely be the determination of very small NaCl concentrations (10⁻⁷ M and probably even lower) based onto the fracture mechanics properties. In our experiments the nanopillars, which were exposed to NaCl, returned to their original mechanical stability after the medium was exchanged to pure water as in the original state. Altogether, the processes involved here appear to be fully reversible.

In another series of experiments, it was examined how far the statistical method is applicable for real-world problems as they frequently occur in industry. Together with Hightec MC from Lenzburg, Switzerland, a company dedicated to microelectronics, experiments were designed to examine how water is influencing the adhesion between a polyimide polymer and a metallization layer (titanium). Hightec MC encountered that the adhesion between the polyimide and the metallization layer is below the required values in sporadically occurring badges of their manufactured flexible electronic circuitry. A minimal amount of water at the interface position was suspected to be the cause of this problem. For this reason, samples with 0, 1 and 5 Langmuir of water deposited at the interface position

were produced. With the aid of a FIB, nanopillars were then implemented into these so prepared samples. With these as produced pillars, it was shown that, contrary to the initial hypothesis, water seems to have a positive effect on adhesion instead of a negative one. This means that interface water decreases the amount of broken pillars instead of the anticipated increase. This would mean that the amount of broken pillars decreases from 94 % for 0 L of water down to a level of about 25 % for 5 L water at the interface. This is an astonishing result which may be used for improving the adhesion between polymers and metallization layers at a later stage. In order to analyze the situation before and after the fracturing, also friction forces were measured at the pillars base and on the socket surface exposed by a freshly broken nanopillar. In SFM, frictional forces can be measured by assessing the torsional deformation of the cantilever in the scanning process at a controlled perpendicular force setting and scanning speed. This local friction force assessment showed unequal values between the samples base polyimide surface compared to the polyimide surface from the nanopillar socket right after the Ti part was broken away. In conclusion of our detailed analysis of the interface strength of PI/Ti in this technological context, we attribute the rest gas contained in the process vacuum, to be responsible for the insufficient adhesion between the polymer and the metallization layer. It is known, that titanium has an extraordinary high affinity to oxygen, so this component of the residual gas may provide a strong candidate for a further assessment. For an industrial manufacturing setup our result implies that the vacuum chambers, which have to be vented in order to replace the already processed samples with new ones, contain residual oxygen which then will react with the first amounts of evaporated titanium, which in consequence form a weakly bound TiO_2 layer.

As shown in this work, it is possible to perform fracture experiments on a very small scale in various environments with the aid of the SFM techniques developed in this work: Friction, fracture and corrosion but also lubrication and erosion experiments are possible to be performed and provide a radically new approach to fracture mechanics and nanomechanics with probed structures on a true nanometer scale. The understanding of microscopic processes can be expanded this way, an important pre-requisite for the further development of nanomechanics in micro- and nanotechnological applications. As processes on the macroscopic scale are intimately connected to the corresponding processes on a small scale, these examinations might further contribute to understand the initiation of fracture of larger structures and in particular in the context of slowly acting mechanisms as corrosion and degradation by solubilization. Finally, this study comprises an example for the assessment of

the parameter dependent interface strength of so far two technologically and scientific important material systems: Ti on PI and SiO₂ on Si. Thereby, SFM-based nanofracture experiments now reach beyond the investigation of brittle systems which were first investigated by the group and are ready for the investigation of interface strength in dependence of chemical and/or physical parameters.

ACKNOWLEDGEMENT

Many people contributed to this PhD thesis. I am grateful to all of them!

First of all, I would like to thank Prof. Dr. Thomas Jung for giving me the opportunity to work under his supervision, coaching and to be my doctor father.

I owe Dr. Helmut Shift many thanks, for coaching this thesis too, being also one of my supervisors and for the scientific advice.

In numerous discussions Thomas and Helmut helped me with lots of ideas and were therefore a great source of inspiration. Without their help, this work would definitely not be possible.

Furthermore, I would like to thank Prof. Dr. Ernst Meyer from the University of Basel for being my second examiner. I would also like to thank Prof. Dr. Jens Gobrecht, the leader of the ‘Laboratory for Micro- and Nanotechnology’, for providing excellent working conditions. Prof. Dr. Wolfgang Meier from the University of Basel is heartily thanked for the straightforward help to accomplish my Master’s thesis which I had to do during my PhD study. I would also like to thank Prof. Dr. Martina Hirayama (ZHAW) for her continued guidance in my career.

The people from Hightec MC are many times thanked for their great support and for all the interesting things they showed me in their clean room. Especially Dr. Hans Burkard, Simon Gubser and Karl Kurz are thanked for the introduction into the secrets of printed circuit boards made of polyimide polymers.

I also need to thank the colleagues who got me through this: Rolf Schelldorfer for the SFM introduction, Dr. Kathrin Müller who has helped me with XPS, Eugenia Minikus who showed me the TEM and Julijana Krbanjevic who was responsible for the introduction to the FIB. All these people are thanked very much indeed.

A big ‘thank you’ goes to all my MOLNANO colleagues: Dr. Nirmalya Ballav, Dr. Claudio Vanoni, Dr. Andreas Scheybal, Rolf Bertschinger, Dorota Chylarecka, Jan Girovsky, Tatjana Hählen and Christian Wäckerlin. Special thanks and many wishes are given to Dariusz Jarzabek for the continuation of this research.

Special thanks go to Patrick Helfenstein and Sonja Neuhaus for proof reading and their invaluable input. Many thanks also to the famous ODRA/100 team: Dr. Christian Dais,

Dr. Patrick Farquet, Dr. Sankha Subhra Sarkar, Niklaus Baumann, Jan Rhensius, Thomas Siegfried and Jörg Ziegler. It was a great time to work with you!

Life at PSI wouldn't be the same without the people from the 11.45 lunch group: Dr. Martin Bednarzik, Dr. Celestino Padeste, Dr. Arne Schleunitz, Mirco Altana, Peter Friedli, Arnold Lücke, Edith Meisel, Stefan Neuenschwander, Simon Rutishauser, Christian Spreu, Lorena Strübin, Stefan Stutz, Konrad Vogelsang and Anja Weber.

Eugen Deckardt and Thomas Neiger are thanked for many discussions in the floors and around the Diorit building.

Finally, I am especially thankful that Dr. Lorenz Meier was helping me with some of the figures (all the great ones!) shown in this text.

And last of all, thank you Yvonne, for reading this thesis, again and again, for weathering my minor crises of confidence (and a couple of major ones), for never doubting. This thesis would not be without you. I love you!

LIST OF PUBLICATIONS

DIPLOMAS

Master's thesis in chemistry (University Basel, Switzerland) from
A.N. Kaufmann
Advisors: W. Meier (Unibas) and T.A. Jung (PSI, Unibas)
The titanium/polyimide interface as a function of its water content
28.6.2010

INVITED TALKS

A.N. Kaufmann
Nano fracture mechanics for studying adhesion and corrosion on interfaces and grain boundaries
EMPA Seminar talk, Thun, Switzerland, 4.11.2008

ORAL PRESENTATIONS

A.N. Kaufmann, S. Gubser, H. Burkard, H. Schiff, E. Meyer, and T.A. Jung
Quantitative assessments of interface strengths and fracture for nanotowers containing specific materials interfaces
3rd Vienna International Conference on Nanotechnology, Wien, Österreich, 18.-20.3.2009

A.N. Kaufmann, H. Schiff, E. Meyer, and T.A. Jung
Fracture and wear of 'nanotowers'
12th International Conference on Fracture, Ottawa, Canada, 12.-17.6.2009

A.N. Kaufmann, H. Schiff, Ernst Meyer, and Thomas A. Jung
Fracture and Wear of "Nanopillars" - Defined Fracture at Interfaces using Scanning Force Microscopy
Int. Colloquium Micro-Tribology, Milowka, Poland, Sept. 21-24, 2009

A.N. Kaufmann, H. Schiff, Ernst Meyer, and Thomas Jung
The Fracture Behavior of Nanostructures
2009 MRS Fall Meeting, Boston, USA, 30.11.-4.12.2009

A.N. Kaufmann, H. Schiff, E. Meyer, and T.A. Jung
Fracture mechanics for the study of interfaces on the nanoscale
1st European Nanomanipulation Workshop, Cascais, Portugal, 17.-19.5.2010

A.N. Kaufmann, H. Schiff, E. Meyer, and T.A. Jung
Interface strength and fracture behavior of nanostructure
Seeing at the Nanoscale VIII, Basel, Switzerland, 30.8.-1.9.2010

POSTERS

A.N. Kaufmann, S. Gubser, L. Heyderman, H. Schiff, H. Burkard, E. Meyer, and T.A. Jung
Interface strengths and fracture behavior of nanotowers
NanoEurope, St.Gallen, Switzerland, 16.-17.9.2008

A.N. Kaufmann, S. Gubser, H. Schiff, H. Burkard, E. Meyer, and T.A. Jung
Interface strengths and fracture behaviour of nanotowers – A new versatile way for testing adhesion and related phenomena
NanoTechDay, Aarau, 20.5.2009

A.N. Kaufmann, S. Gubser, H. Schiff, H. Burkard, E. Meyer, and T.A. Jung
Interface strengths and fracture behaviour of nanotowers – A new versatile way for testing adhesion and related phenomena
Interdisciplinary Symposium on 3D Microscopy 2009, Interlaken, Switzerland, 12.-16.7.2009

A.N. Kaufmann, H. Schiff, Ernst Meyer, and Thomas Jung
Measurement of mechanical strength of interfaces in nanopillars
Int. Conf. on Nanoimprint and Nanoprint Technology (NNT 2009), San Jose, California, USA, Nov. 11-13, 2009

A.N. Kaufmann, H. Schiff, H. Burkard, T. Debski, E. Meyer, and T.A. Jung
Measurement of mechanical properties of nanotowers
NanoTechDay, Basel, Switzerland, 11.5.2010

PAPERS, PROCEEDINGS

A.N. Kaufmann, H. Schiff, E. Meyer, and T.A. Jung
Fracture and wear of ‘nanotowers’
12th International Conference on Fracture, Ottawa, Canada, 12.-17.6.2009

A.N. Kaufmann, S. Gubser, H. Burkard, H. Schiff, E. Meyer, and T.A. Jung
Quantitative assessments of interface strengths and fracture for nanotowers containing specific materials interfaces
3rd Vienna International Conference on Nanotechnology, Wien, Österreich, 18.-20.3.2009

A.N. Kaufmann, H. Schiff, H. Burkard, E. Meyer, and T.A. Jung
Nano-fracture mechanics: Scanning force microscopy used to test adhesion strength at the titanium/polyimide interface
Submission intended to Nanotechnology

PUBLIC RELATIONS

A.N. Kaufmann, H. Schiff, H. Burkard, T. Debski, E. Meyer, and T.A. Jung
Presentation of the Nano-Argovia project “NanoBruch” in representation of T.A. Jung
NanoTechDay, Basel, Switzerland, 11.5.2010

AWARDS & OTHER HONORS

Nanopic Award 2008

A.N. Kaufmann
“I ‘LOVE’ U” written in a field of nanopillars by a SFM-based method for storing data
Swiss Nanoscience Institute (University Basel, Switzerland)

Chairman on Wednesday July 15, 15:30 – 16:50 in the session T29-S3: Nano-Or Micro-Scale

A.N. Kaufmann
Fracture and wear of ‘nanotowers’
12th International Conference on Fracture, Ottawa, Canada, 12.-17.6.2009

Oral presentation was mentioned on the conference webpage (day 4) with an own small article about the presentation/project

A.N. Kaufmann, Helmut Schift, Ernst Meyer and Thomas Jung

The Fracture Behavior of Nanostructures

2009 MRS Fall Meeting, Boston, USA, 30.11.-4.12.2009

CURRICULUM VITAE

Date/place of birth: 30.9.1978 in Zürich, Switzerland

Nationality: CH

Work experience:

01/2003 – 03/2007 Zürcher Hochschule Winterthur (ZHW), Switzerland
Research assistant in Industrial Chemistry

Education/Studies:

03/2007 – 03/2011 PhD student in Nanosciences at Paul Scherrer Institute (PSI) in
Würenlingen, Switzerland

02/2009 – 06/2010 Master's course in Chemistry at the University of Basel,
Switzerland.

Diploma as M.Sc. in Chemistry (University of Basel)

10/2004 – 03/2007 Master's course in Micro- and Nanotechnology of the Micro-
and Nanotechnology-Network of the Euregio Bodensee
(EMPA, FH Vorarlberg, NTB and ZHW under the scientific
lead of the ETH in Zürich).

Diploma as M.Sc. in Micro- and Nanotechnology (FH
Vorarlberg)

10/1998 – 12/2002 Study in chemistry at ZHW

Diploma as dipl. Chemist FH (ZHW)

08/1995 – 07/1998 Apprenticeship as a chemical lab assistant at EAWAG in
Dübendorf, Switzerland

During my studies I have heard lectures by the following people:

Lecturer of the University of Basel Master's course:

Werner Bonrath, Roland Buser, Edwin Constable, Karl Gademann, Peter Hauser, Thomas Jung, Christian Körner, Marcel Mayor, Andreas Pfaltz, Thomas Ward, Hermann Wegner, Helma Wennemers

Lecturer of the Euregio Bodensee Master's course:

André Bernard, Rudolf Buser, Walter Caseri, Alex Dommann, Roman Fasel, Thomas Graule, Pierangelo Gröning, Ursula Graf-Hausner, Martina Hirayama, Peter Hudek, Hans-Josef Hug, Peter Jacob, Johann Michler, Markus Michler, Jörg Patscheider, Beat Ruhstaller, Patrick Schwaller, Hansueli Schwarzenbach, Thomas Spielmann

Lecturer of the Zürcher Hochschule Winterthur (FH):

Peter Benz, Heinrich Bühler, Martin Conzett, Jürg Donatsch, Eduard Gamp, Urs Goldener, Walter Krebs, Roland Kunz, Peter Lienemann, Gaudenz Marx, Urs Michel, Gustav Peter, Ferenc Rakoczi, Thomas Spielmann, Jürgen Stohner, Samuel Wunderli